Summer 2010

Project RESUN, a Radio Evla Search for UHE neutrinos

Theodore Robert Jaeger
University of Iowa

PROJECT RESUN, A RADIO EVLA SEARCH FOR UHE NEUTRINOS

by

Theodore Robert Jaeger

An Abstract

Of a thesis submitted in partial fulfillment of the
requirements for the Doctor of Philosophy
degree in Physics in the
Graduate College of The
University of Iowa

July 2010

Thesis Supervisor: Professor Robert Mutel

ABSTRACT

In the past decade there have been several attempts to detect ultra high energy (UHE) neutrinos by searching for radio Ĉerenkov bursts in terrestrial ice or the lunar regolith. So far these searches have yielded no detections, but the inferred flux upper limits have started to constrain physical models for UHE neutrino generation. This thesis is a description of the Radio EVLA Search for UHE Neutrinos (RESUN) experiment, aimed at further limiting isotropic and point-source production models. RESUN uses the Expanded Very Large Array (EVLA) configured in multiple subarrays of four antennas observing at 1.4 GHz pointed along the lunar limb to detect neutrino-induced Ĉerenkov bursts. No pulses of lunar origin were detected during a observing campaign totaling 250 hours, implying an upper limit to the differential isotropic neutrino flux E dN/dE < 1 km^{-2} yr^{-1} sr^{-1} at 90% confidence level for sources with energy (E) exceeding $10^{21.2}$ eV and E dN/dE < 0.1 km^{-2} yr^{-1} sr^{-1} for E $> 10^{22.5}$ eV. The isotropic flux upper limit is the lowest published for lunar searches and is inconsistent with extra-galactic and halo Z-burst models for neutrino generation. Further, RESUN establishes 90% confidence differential flux limits for 41 AGN sources within 50 Mpc which were located along the lunar celestial path.

Abstract Approved: _____
Thesis Supervisor

_____
Title and Department

_____
Date

PROJECT RESUN, A RADIO EVLA SEARCH FOR UHE NEUTRINOS

by

Theodore Robert Jaeger

A thesis submitted in partial fulfillment of the
requirements for the Doctor of Philosophy
degree in Physics in the
Graduate College of The
University of Iowa

July 2010

Thesis Supervisor: Professor Robert Mutel

Graduate College
The University of Iowa
Iowa City, Iowa

CERTIFICATE OF APPROVAL

PH.D. THESIS

This is to certify that the Ph.D. thesis of

Theodore Robert Jaeger

has been approved by the Examining Committee for the thesis requirement for the Doctor of Philosophy degree in Physics at the July 2010 graduation.

Thesis Committee: _____
Robert Mutel, Thesis Supervisor

_____
Kenneth Gayley

_____
Cornelia Lang

_____
David Peate

_____
Mary Hall Reno

To my first physics instructor Dr. Theo Koupelis who told me graduate school was too difficult without the support of a partner, and to my wife Ferzan who was there for me when he was right.


I DID IT.
I DID IT.
SOMEHOW I IMAGINED THIS EXPERIENCE WOULD BE MORE REWARDING.

ACKNOWLEDGMENTS

I first and foremost thank my advisor Robert Mutel, for many good adventures and without whom the content of this thesis would not be possible. I am also grateful for the support I received from numerous individuals, most notably; Ken Gayley for his nearly overnight development of the lunar aperture model and apt insights; Hallsie Reno for her insights on neutrino interaction physics; Peter McMahon, Andrew Siemion, and Dan Wertheimer from the UCB CASPER lab; Dan Mertely, Barry Clark, and the staff of the NRAO for doing just about any crazy thing we asked; Mike Fountian and Ron Vogel for continual mechanical and electrical advice; and Cornelia Lang for her much appreciated guidance on issues both academic and otherwise.

TABLE OF CONTENTS

LIST OF TABLES

Table

LIST OF FIGURES

Figure

CHAPTER 1
INTRODUCTION

1.1 The Universe Above 10^{18} eV

Determining the source and characteristics of Ultra High Energy (UHE, energies exceeding 10^{18} eV or 1 EeV) particles is of fundamental importance in astrophysics. Currently, all observed UHE particles have been in the form of highly accelerated atomic nuclei known as cosmic rays. Presumably, these energetic nuclei are generated by nearby sources, as direct detection of UHE cosmic rays (UHECRs) from distant sources appears unlikely due to interaction with cosmic microwave background (CMB) photons. Above a limiting energy of $10^{19.5}$ eV, also known as the Greisen-Zatsepin-Kuzmin or GZK limit, cosmic rays are expected to interact with CMB photons within a few tens of Mpc (10^6 pc $\sim 3 \times 10^{22}$ m) from their source and be destroyed. Recent measurements of the cosmic ray spectrum at UHE energies (Yamamoto, 2008) show a clear drop at the GZK limit, consistent with the prediction. However, a predicted byproduct of the GZK interaction is a shower of high-energy pions (Greisen, 1966; Zatsepin and Kuz'min, 1966) which quickly decay and create ultra-high energy (UHE) neutrinos. Unlike cosmic rays, neutrinos can propagate unimpeded directly to the Earth, meaning cosmic ray generation processes thought to occur in distant active galactic nuclei (AGN) cores and hypernovae can be traced via the secondary production of cosmogenic UHE neutrinos. Other, more speculative, sources for UHE neutrinos include GRBs and top-down production from dark matter annihilation, super heavy particle decay (Sigl et al., 1999), the Z-burst mechanism (Fodor et al., 2002; Kalashev et al., 2002), and cosmic topological defects (Stanev, 2004). Although not yet detected, these UHE neutrinos will provide a fundamentally new window for studying the physics of AGN and exotic astrophysical particles.

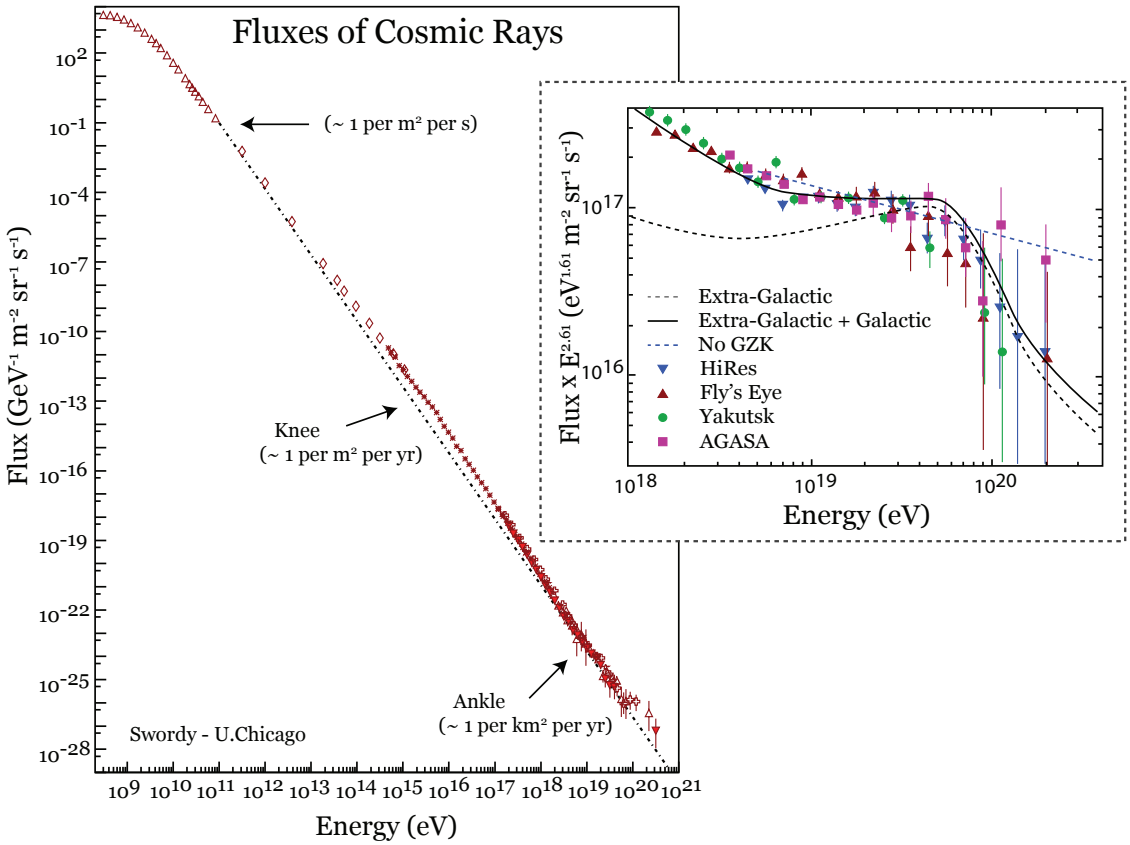

Figure 1.1: Observed Cosmic Ray spectrum across a wide range of energies (Cronin et al., 1997). Inset shows a detailed view of the "Ankle" region (adapted from Waxman 2009) located at the UHE end of the spectrum. Recent measurements at UHE energies have revealed a drastic attenuation of the CR spectrum at $10^{19.6}$ eV, consistent with the predicted GZK cutoff. Note that the ordinate of the inset has been scaled by a factor of $E^{2.61}$ to better illustrate the CR flux drop-off.

1.2 The Moon as a Neutrino Detector

Since the interaction cross-section of neutrinos with matter is notoriously small, large targets are required to detect UHE neutrinos for realistic observation times. A promising approach is the observation of radio bursts resulting from UHE neutrino interactions with the Moon. Using the moon as a neutrino detector was first suggested by Dagkesamanskii and Zheleznykh 1989 based on an earlier prediction by Askaryan (1962) that UHE neutrinos and cosmic rays could interact with

bulk materials such as ice, salts, or the lunar regolith and produce bursts of radio Ĉerenkov radiation (see Fig. 1.2). Incident neutrinos with a mean free path of $\sim$ 10-100 km (Reno, 2005) interact with lunar baryons to produce a shower of short-lived particles which decay into e+/e- pairs. However, processes of positron annihilation and electron entrainment change the overall neutral shower into one with a 20% net electron excess. As the electrons are moving at the free-space speed of the incident neutrino ($\sim$ c, larger than the phase speed of light in the medium), they produce a very short duration (hence wide bandwidth) burst of radio Ĉerenkov radiation concentrated in a thin cone with half-angle $\theta_c \sim 55^\circ$ (James and Protheroe, 2009).

The Ĉerenkov pulse is attenuated in a very short distance in the lunar regolith, with an electric field attenuation length of 10-100 m (Olhoeft and Strangway, 1975). However, if the interaction occurs at a shallow depth and the neutrino enters the moon at an angle that does not result in total internal reflection of the radiation cone (cf. Figure 1.2), the emission partially escapes and is visible on earth by cm-wavelength radio telescopes. Askar'yan's prediction and many details of the particle interaction have been directly verified with pulsed electron bunches and salt and ice targets at the Stanford Linear Accelerator (Saltzberg et al., 2001; Miocinovic et al., 2006; Gorham et al., 2007) . The pulse emission was shown to be broadband, linearly polarized, with nanosecond characteristic timescales, and corresponding bandwidth 1-10 GHz, depending on the observer's location in the radiation cone.

1.3 History of Lunar UHE Neutrino Searches

Searching for radio bursts with such small time scales is problematic. Although the peak flux density is predicted to be very intense, e.g. of order 10^5 Jy at 1 GHz (Alvarez-Muniz et al., 2000), interference and radiometer statistical power fluctuations can mimic the desired signals. Hence, well-designed detection schemes must strongly discriminate signals of lunar origin from accidental pulses.

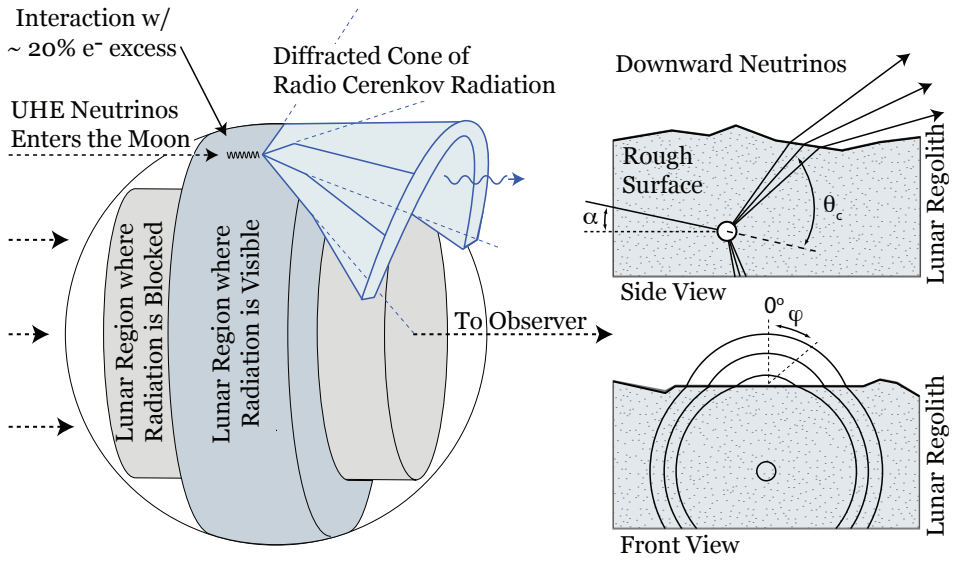

Figure 1.2: Illustration of a UHE neutrino interaction with lunar regolith matter. The neutrino-parton interaction results in a near light-speed hadronic shower with eventual 20% charge excess, creating a cone of radio Ĉerenkov emission. Cones that are both created near the surface and do not suffer from total internal reflection partially escapes the lunar surface, where an observer sees a nanosecond-duration radio pulse.

The first pioneering search was performed in 1995 when Hankins et al. (1996) observed the Moon in a band from 1200 -1700 MHz using the Parkes telescope in Australia. They searched for pulses dispersed by the Earths ionosphere, using the frequency dependent delay to discriminate against terrestrial RFI pulses. Not realizing that only on the lunar limb could Ĉerenkov emission escape in the direction of the observer, they spent a large fraction of their 12 hour experiment pointed at the lunar center and they detected no pulses of lunar origin.

The second lunar radio search, known as GLUE (Goldstone Lunar UHE Neutrino Experiment, Gorham et al. 2004) employed the Goldstone 70m and 34m telescopes with a large (22 km) separation to search for delayed pulse coincidence. They found no pulses of lunar origin in 120 total hours of observation, but the sampled

fraction of the lunar limb was limited by the small primary beams of the antennas compared with the angular size of the Moon ($\sim 8\%$). Additional lunar target searches using the 64-m diameter Kalyazin telescope (Beresnyak et al., 2005) and the Westerbork Synthesis Radio Telescope (Scholten et al., 2009) also reported no UHE neutrino detections. Several lunar radio searches using existing or planned radio telescopes have also been discussed by Scholten et al. (2006, LOFAR), Panda et al. (2007, GMRT), James and Protheroe (2009, SKA), and James et al. (2009, ATCA) and there are multiple terrestrial ice searches for Ĉerenkov radio bursts reported by Lehtinen et al. (2004, FORTE), Kravchenko (2006, RICE), Barwick (2006, ANITA-lite), and Gorham et al. (2009, ANITA). So far, no UHE neutrinos have been detected by any of these experiments.

1.4 Project RESUN

Project RESUN, short for Radio EVLA[1] Search for UHE Neutrinos is the focus of this thesis. RESUN is a lunar-target search for radio Ĉerenkov bursts aimed at further limiting isotropic and point-source neutrino production models. The experiment uses the Expanded Very Large Array (EVLA) configured in multiple subarrays of four antennas arranged along the lunar limb to obtain the maxim limb coverage and minimize the moon's contribution to the system temperature (a measure of the system sensitivity). RESUN observes at 1.4 GHz and uses high speed data acquisition devices to detect and store voltage pulses exceeding a set threshold on individual EVLA antennas. The geometrical delay between antenna pairs is used to determine the origin of detected pulses and discriminate against statistical and terrestrial interference. No pulses of lunar origin were observed during two observing campaigns totaling 250 hours. This implies an upper limit to the differential neutrino flux E dN/dE < 1 km^{-2} yr^{-1} sr^{-1} at 90% confidence level

[1]Expanded Very Large Array, operated by National Radio Astronomy Observatory under the auspices of AUI

for isotropic sources with neutrino energy (E) exceeding $10^{21.2}$ eV and E dN/dE < 0.1 km^{-2} yr^{-1} sr^{-1} for E $> 10^{22.5}$ eV. The isotropic flux upper limit is the lowest published for lunar searches and is inconsistent with extra-galactic and halo Z burst models for neutrino generation, in agreement with the ANITA Antarctic ice observations (Gorham et al., 2009) and WMAP neutrino mass limits(Crotty et al., 2004; Fogli et al., 2004). RESUN also uses the varying lunar position to establish 90% confidence differential flux limits for 41 AGN sources within 50 Mpc.

1.5 Detecting UHE Cosmic Rays

Like UHE neutrinos, UHE cosmic rays will also cause Ĉerenkov bursts upon impacting the lunar surface. Indeed, the probability of detection for UHECR is much larger, since they all interact with the lunar regolith very close to the surface where radiation can easily escape. Nevertheless, extragalactic UHECR with energies above the GZK cutoff ($E_{GZK} = 10^{19.5}\ eV$) should be scattered by CMB photons and lost unless the source is relatively close (within ~ 50 Mpc). Super-GZK UHECR are therefore not expected to exist, except possibly from a few discrete nearby sources. For this reason, only UHE neutrinos are considered in the RESUN experimental planning, although UHECR certainly would be detected as well, if they exist.

CHAPTER 2
UHE NEUTRINO-REGOLITH INTERACTIONS

The sections that follow describe the characteristics of UHE neutrino interactions with the moon, as first predicted by Askaryan (1962) and with many properties experimentally verified by particle accelerator tests on salt, ice, and sand targets (Saltzberg et al., 2001; Miocinovic et al., 2006; Gorham et al., 2007). For this reason, many of the expressions used to describe the neutrino-moon interaction are applicable to a wide range of target material by inserting the appropriate constants. A summary of the pertinent lunar constants can be found in Table 2.1 and a summary of the corresponding Ĉerenkov burst properties with respect to the RESUN experiment can be found in Table 2.2.

In this analysis, UHE neutrinos interact with baryons in the lunar regolith, unless otherwise indicated. The regolith refers to the upper-most layer of lunar rock which displays a fractal distribution of particle sizes (Shepard et al., 1995) and has average physical properties determined by multiple direct measurements (James and Protheroe, 2009, and refs.).

2.1 Creating the Ĉerenkov Burst Emission

Incident UHE neutrinos interact with baryons in the target media with an energy-dependent cross-section given by (Reno, 2005)

$$\sigma(E) = 1.57 \times 10^{-31} \left(\frac{E}{ZeV} \right)^{1/3} \text{ cm}^2, \tag{2.1}$$

where ZeV $= 10^{21}$ eV. The corresponding mean free path of the neutrino in the lunar regolith can be expressed as

$$\lambda_\nu(E) = \left[\frac{m_H}{\sigma(E)\rho_r} \right] = 35.7 \text{ km} \left(\frac{ZeV}{E} \right)^{1/3} \tag{2.2}$$

Table 2.1: Lunar Regolith Physical Constants.

n	ρ	X_r	V_o	ν_o	α_o
1.73	1.8	22.1	0.1	2.32	1.23

Units: ρ (gm/cm^3), X_r (gm/cm^2), V_o (μV m^{-1} MHz^{-1}), ν_o (GHz)

where E is the neutrino energy and $\rho_r = 1.8$ gm cm^{-3} is the mass density of baryons in the regolith (James and Protheroe, 2009). While large, it is in sharp contrast with the neutrino mean free path in the intergalactic medium which is characterized by a baryon mass density of $\rho_g \sim 10^{-24}$ gm cm^{-3} ($\rho_g \sim 10^6 \rho_{crit}$). At the energies in question, this density corresponds to a length exceeding 10^{25} km or a factor of 10 time the size of the known universe (cf. Wynn-Williams 1992).

The neutrino does not impact baryons *per se*, but instead with their interior, point-like constituent partons (quarks and/or gluons) and results in a hadronic shower with approximately 20% of the initial neutrino energy. This shower quickly evolves into a short-lived current source via processes of electron entrainment and positron annihilation (Alvarez-Muniz et al., 2008). The transient current creates a pulse of coherent Ĉerenkov radiation, since the electrons' speed ($\sim$ c) is greater than the local phase speed of light in the medium. An illustration of the UHE neutrino-baryon interaction is given in Figure 2.1.

The characteristic hadronic shower length L_s is given by (Scholten et al., 2006)

$$L_s(E) = \left[13.37 + 0.67 \log\left(\frac{E}{ZeV}\right)\right] \cdot L_r \tag{2.3}$$

where L_r is the radiation length equal to ratio of the nuclear interaction length (X in gm/cm^2) to the mass density (ρ in gm/cm^3). For the lunar regolith, $X_r = 22.1$ gm/cm^2 and the hadronic shower length is $\sim$1.5 m at 1 ZeV, corresponding to a broadband pulse with a characteristic timescale $\tau = L_s/c \sim 5$ ns.

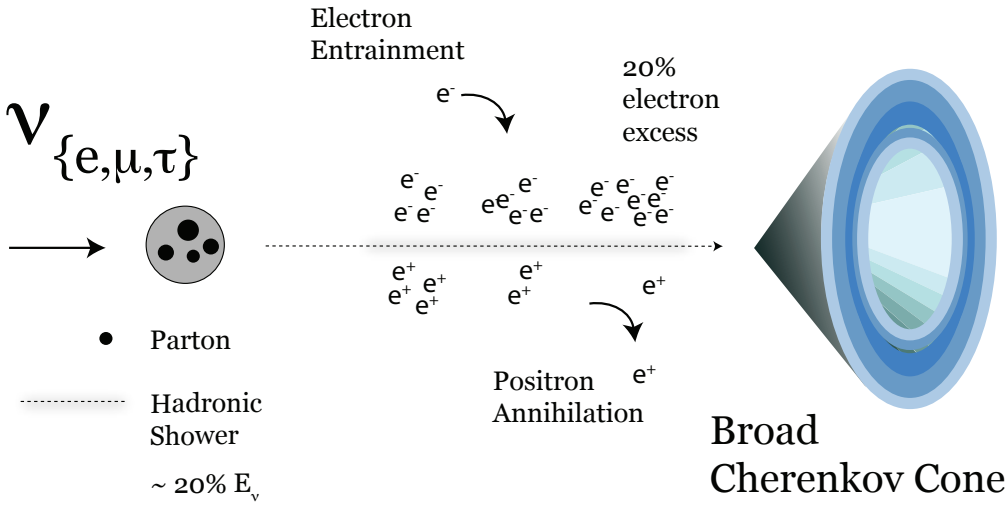

Figure 2.1: Sketch of the neutrino-parton interaction. The hadronic shower carries 20% of the neutrino energy and eventually decays to primarily e^+e^- pairs. Positrons are absorbed more quickly than the elections, resulting in a 20% net e^- charge excess. This charged current emits a short-duration Ĉerenkov pulse with a cone width given by Equation 2.5.

The remaining 80% of the neutrino energy goes into one of two different reactions. For neutral-current (NC, branching ratio $\sim 1/3$) interactions, the neutrino is scattered and retains the remaining energy. In the charge-current (CC, branching ratio $\sim 2/3$) case, a muon, electron, or tau lepton is produced with the remaining $\sim 80\%$ of the energy. While muons and tauons are absorbed by the surrounding medium, electrons will initiate a electromagnetic cascade which in turn creates a secondary Cerenkov cone. However, the EM cascade is considerably elongated by the Landau-Pomeranchuk-Migdal (LPM) effect (Alvarez-Muniz et al., 2000), forming a narrow emission cone which has a negligible contribution to the total emission at most observing angles.

Table 2.2: Ĉerenkov Burst Properties pertaining to the RESUN Experiment.

θ_c	$\Delta\theta_H$	L_r	λ_ν	$\lambda_\mathcal{E}$	$\mathcal{E}^c_{TX}$
54.7°	2°	1.64 m	35.7 km	12.4 m	0.024 μV m^{-1} MHz^{-1}

RESUN parameters: E = 1 ZeV, ν = 1.4 GHz

2.2 Properties of the Ĉerenkov Radiation Pulse

The UHE neutrino-induced hadronic shower generates a pulse of Ĉerenkov emission concentrated in a cone with medium dependent half-angle equal to

$$\theta_c = \text{acos}(\frac{1}{n_r}) \sim 55^\circ \tag{2.4}$$

where $n_r = 1.73$ is the refractive index of lunar regolith (James and Protheroe, 2009). This cone has a width that varies strongly with observation frequency and has a small energy dependance. The cone's full angular e^{-1} width in lunar regolith can be written (James and Protheroe, 2009)

$$\Delta\theta_H(E,\nu) = 2.9^\circ \left[\frac{\text{GHz}}{\nu}\right] \left[1.15 + 0.075 \log\left(\frac{E_s}{ZeV}\right)\right]^{-1} \tag{2.5}$$

where the expression from James and Protheroe (2009) has been multiplied by 1.2 to convert from half-wifth to e^{-1} width and $E_s = 0.2\ E$ is the shower enengy. At $E = 1$ ZeV, the resulting cone widths vary from 17.6° at 150 MHz to 0.5° at 5 GHz. Note that the Ĉerenkov cone angle is the exact complement of the total internal reflection critical angle $\theta_{crit} = \sin^{-1}(1/n_r) = 35^\circ$. This implies that, baring surface roughness effects (see Chapter 4 for discussion), only neutrinos with small range of "skimming" impact angles can produce emission escapes into free-space and be witnessed by an exterior observer. Positive impact angles (α) which are larger than the cone width create Ĉerenkov cones which suffer total internal reflection on a smooth lunar surface, and large negative impact angles produce cones too deep

below the lunar surface to escape.

The burst electric field strength $\mathcal{E}$ at a distance R can be parameterized as

$$\mathcal{E}^c(E,\nu,\theta) = \frac{V_0}{R} \cdot \frac{E}{ZeV} \Psi(\nu)\Theta(E,\nu,\theta) \tag{2.6}$$

where the constant $V_0 = 0.1\ \mu V\ \mathrm{m}^{-1}\ \mathrm{MHz}^{-1}$ and functions $\Psi(\nu)$, $\Theta(E,\nu,\theta)$ are scaling factors of order-unity for frequencies > 1 GHz and observations near the Ĉerenkov angle (cf. Figs. 2.2a,b).

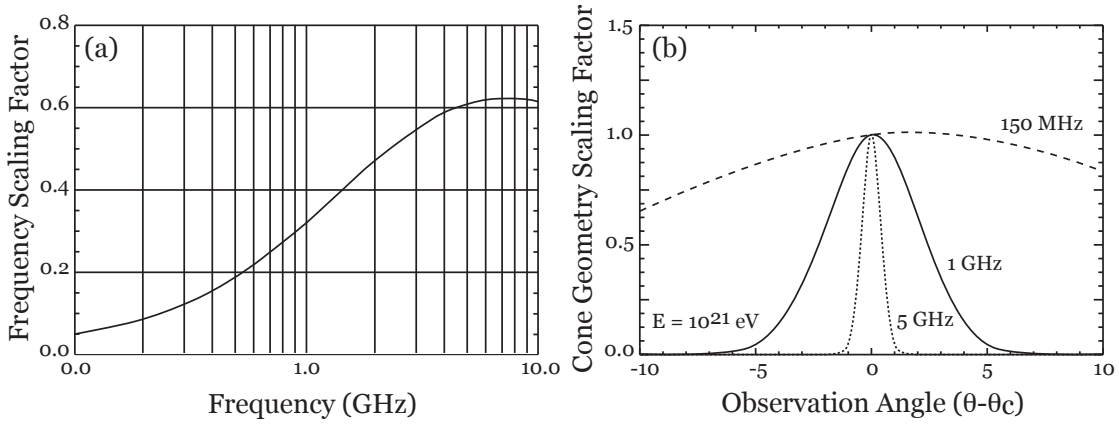

Figure 2.2: Frequency (a) and Cone Geometry (b) scaling factors from Eqn. 2.6.

The frequency scaling function $\Psi(\nu)$ is based on the Stanford Linear Accelerator (SLAC) electron beam experiment (Gorham et al., 2000; Saltzberg et al., 2001) and is expressed

$$\Psi(\nu) = \left[\frac{\nu}{\nu_o}\right]\left[1 + \left(\frac{\nu}{\nu_o}\right)^{\alpha}\right]^{-1} \tag{2.7}$$

with $\nu_o = 2.32$ GHz, $\alpha = 1.23$ for regolith material (James and Protheroe, 2009). The cone geometry function $\Theta(E,\nu,\theta)$ accounts for the decrease in signal strength for observations off the cone axis and is given by (Alvarez-Muñiz et al., 2006; James and Protheroe, 2009)

$$\Theta(E,\nu,\theta) = e^{(-\Delta\theta/\Delta\theta_H(E,\nu))^2} \cdot \frac{\sin(\Delta\theta + \theta_c)}{\sin(\theta_c)} \tag{2.8}$$

where $\Delta\theta$ is angle off the the cone axis.

2.3 Transmission into Free-Space

In the absence of regolith attenuation (interactions near the surface), the peak electric field strength ($\theta = \theta_c$) of the Ĉerenkov pulse at the telescope for the RESUN search (ν_0=1.4 GHz) is

$$\mathcal{E}^c_{max,int}(E) = 0.041 \left(\frac{E}{ZeV}\right) \ \mu V \ \mathrm{m}^{-1} \ \mathrm{MHz}^{-1} \tag{2.9}$$

and the e^{-1} width of the Ĉerenkov cone is $\Delta\theta_H \sim 2.1^\circ$ for all $E \geq E_{GZK}$. Of greater interest is the electric field strength after propagating through the regolith-vacuum interface (cf. Fig. 2.3). Transmission across the lunar interface is a complicated function of both incident angle and polarization (Williams, 2004; Gusev et al., 2006). If the electric field amplitudes $\mathcal{E}$ are Gaussian distributed over the escaping cone width $\Delta\theta$ (refer to Scholten et al. 2006; Gusev et al. 2006 for a discussion of perturbations from this criteria), the transmitted electric field at a fixed frequency is

$$\mathcal{E}^c_{TX} = \mathcal{E}^c_o \ t_\parallel(\beta) \ e^{-(\Delta\theta/\Delta\theta_H)^2} \ e^{-\tau_\gamma} \tag{2.10}$$

where $\mathcal{E}^c_o$ is the strength of the field at the shower along the Ĉerenkov angle, $\hat{t}_\parallel(\beta)$ is the field transmission coefficient for exiting rays that fill the desired solid angle, and τ_γ is the number of radiation mean free paths traversed by the field.

2.3.1 Transmission Coefficient

Assuming the polarization is in the plane of incidence, the field transmission coefficient for plane waves can be expressed (Williams, 2004)

$$t_\parallel \ = \ \sqrt{\frac{n_r \cos\beta}{\cos\beta_o} \ \left(1 \ - \ r^2_\parallel\right)} \tag{2.11}$$

where $r_\parallel$ is the field reflection coefficient for radiation with polarization in the incident plane, β is the angle of incidence inside the Moon relative to the surface

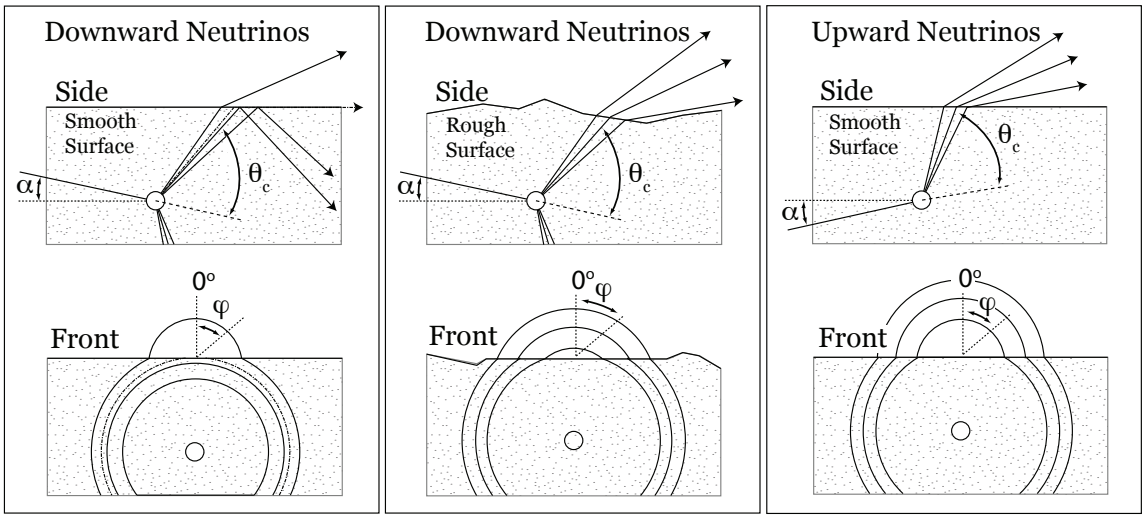

Figure 2.3: (Left panel) Side and face-on views of Ĉerenkov cone ray paths escaping the lunar surface for downward-directed neutrinos, assuming a smooth surface. (Middle) Same, but including surface roughness. Note that a larger fraction of the Ĉerenkov cone escapes. (Right) Same, but for upward-going neutrinos.

normal, and β_o is the angle outside the Moon relative to the surface normal. Using Snell's Law, β_o can also be written

$$\beta_o \;=\; \sin^{-1}(n_r \sin\beta)\;. \tag{2.12}$$

A numeric approximation to Equation 2.11 using a ray tracing technique can be found in in Williams (2004), along with the analytic approximation

$$\hat{t}_{\|} \;=\; \sqrt{\frac{\tan\beta}{\tan\beta_o}(1 \;-\; \frac{\tan\left(\beta-\beta_o\right)^2}{\tan\left(\beta+\beta_o\right)^2}}. \tag{2.13}$$

A slightly more pessimistic approximation can be found in Gusev et al. (2006) equaling

$$\hat{t}_{\|} \;=\; 2\;\frac{\tan\beta}{\tan\beta \;+\; \tan\beta_o}. \tag{2.14}$$

The above expressions predict a transmission coefficient of zero for angles that exceed the compliment of the Ĉerenkov angle ($\beta \geq \pi/2 - \theta_c$) and a value that rapidly becomes non-zero for lesser angles, saturating at a value near 0.7 (cf. Fig. 2.4). A computationally simpler transmission coefficient $\hat{t}_{\|} \approxeq 0.6$ can then chosen

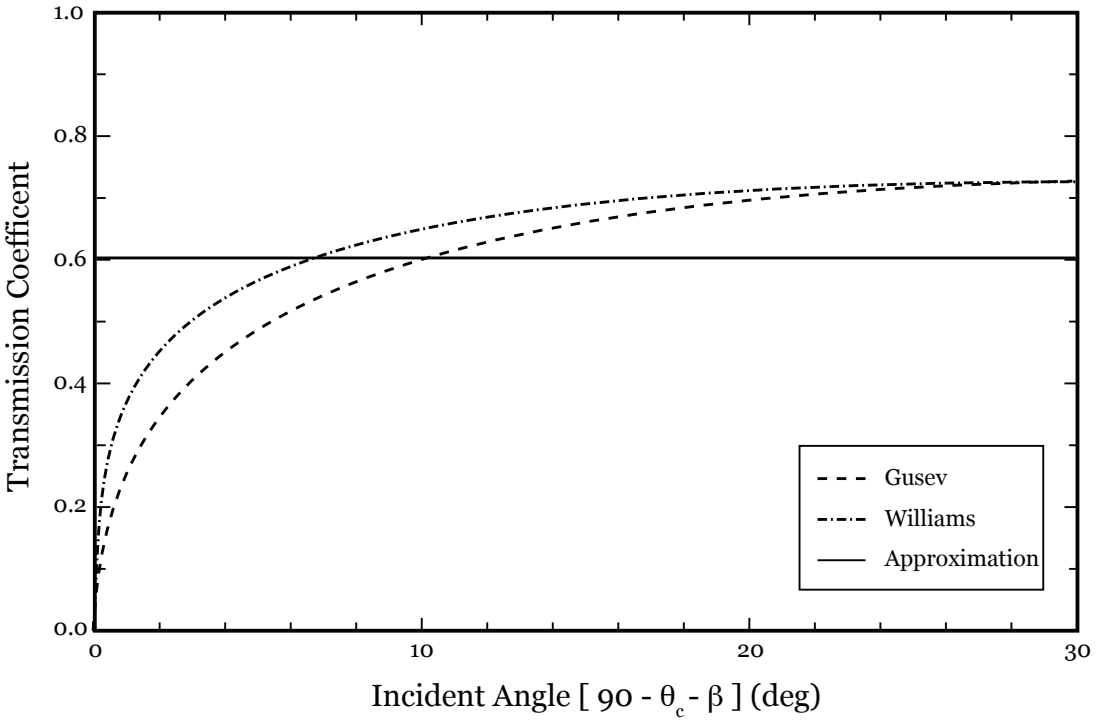

Figure 2.4: Electric field transmission coefficient versus relative incident angle ($\pi/2 - \theta_c - \beta$), where β is the angle to the surface normal. The dashed line is Equation 2.13 from the appendix of Williams (2004), and the dashed-dot line is a similar expression (Eqn. 2.14) from Gusev et al. (2006). The solid line is the constant approximation $t_{||} = 0.6$ used for the RESUN analysis.

without significant error.

2.3.2 Electric Field Attenuation in the Regolith

Along with transmission effects, the burst radiation will also be strongly attenuated by the local medium as it propagates to the surface. The expected decrease in electric field strength requires a nontrivial integration along each escaping ray path, but can be approximated by only considering emission generated very close to the surface. This "near-surface approximation" is valid for cases where the neutrino energy has not been strongly attenuated at a depth radiation can escape. This

requirement is

$$\lambda_{\mathcal{E}} \; << \; \frac{\lambda_{\nu}^{2}}{R_m} \; , \tag{2.15}$$

where R_m is the radius of the moon, λ_ν is the mean free path of the neutrino in the lunar regolith and the electric field attenuation length $\lambda_{\mathcal{E}}$ is (Olhoeft and Strangway, 1975)

$$\lambda_{\mathcal{E}} = 18 \text{ m } (GHz/\nu) \; . \tag{2.16}$$

Strictly, λ_ν is the mean free lunar rock which can be obtained by replacing $\rho_r = 1.8$ gm cm^{-3} with $\rho_r = 3$ gm cm^{-3} (James and Protheroe, 2009) in Equation 2.2. The result is a factor of 2 decrease in the neutrino mean free path, but the distinction has little effect on the above approximation when the limit is well satisfied. Substituting the functional forms of $\lambda_{\mathcal{E}}$ and λ_ν (Eqns. 2.2, 2.16) into Equation 2.15, the approximation requires

$$\nu \; << \; 10^{-3} \left[\frac{E}{ZeV} \right]^{2/3} \text{ GHz} \; . \tag{2.17}$$

The criteria above is safely satisfied over the range of neutrino energies and radio frequencies in the RESUN experiment. As consequence, the regolith electric field attenuation can be ignored for all down-going neutrinos and the Ĉerenkov pulses due to up-going neutrinos are only significantly effected if they exceed a cut-off angle which applies uniformly at all depths. The value of τ_γ in Equation 2.10 is then replaced by

$$\tau_\gamma = 0 \text{ for downward-going neutrinos} \tag{2.18}$$

and

$$\tau_\gamma = \frac{R_m \; \sin\alpha}{\psi \; \lambda_\nu} \text{ for upward-going neutrinos} \tag{2.19}$$

where the angle α is approximated

$$\alpha \; \cong \frac{\psi \; \lambda_\nu}{2 \; R_m} \; , \tag{2.20}$$

and ψ is an order-unity parameter equal 1.4 (for a neutrino spectrum $\sim E^{-2}$, see

the Appendix of Gayley et al. 2009) which accounts for higher energy neutrinos which have previously produced hadronic showers and are now at a lower energy. The maximum free-space electric field strength for upward-going neutrinos is then expressed

$$\mathcal{E}^c_{max,TX}(E,\nu) = 0.6\ \mathcal{E}^c_{max,int}(E,\nu,\theta=\theta_c)\ . \tag{2.21}$$

CHAPTER 3
EXPERIMENT DESIGN

Incident UHE Neutrinos interact with baryons in the lunar regolith and generate transient pulses of coherent radio Ĉerenkov radiation originating from the lunar limb. To detect this emission, the transmitted burst electric field must exceed some factor of the minimum receiver sensitivity for each detector element (single antenna). Note that this is different from interferometer arrays, in which signals are co-added coherently. In general, one can not reliably measure signals with arbitrarily low signal to noise (n_σ), as with lower n_σ an observe detects a rapidly increasing amount of spurious events that mimic the expected Ĉerenkov burst. Detection is further complicated by the presence of terrestrial radio frequency interference (RFI). An experiment must then be designed which addresses these observational constraints to ensure the accidental detection rate is much less than 1 for the total observing period.

3.1 Arrays and Receiver Configuration

The RESUN search used the National Radio Astronomy Observatory's Expanded Very Large Array (EVLA) to search for UHE neutrino induced Ĉerenkov radio bursts originating from the Moon. The EVLA consists of 27 25-m diameter parabolic reflectors with Cassegrain optics in an array whose maximum baseline varies from 1 km to 30 km depending on configuration. RESUN utilized 12 EVLA antennas which were divided into three equal subarrays with baselines of 0.5-5.3 km. These sub-arrays were pointed toward different locations along the lunar limb to obtain maximum limb coverage (see Fig. 3.1). A complete summary of the RESUN observation parameters can be found in Table 3.1.

Observations were made in two 50 MHz bands centered on 1385 MHz and

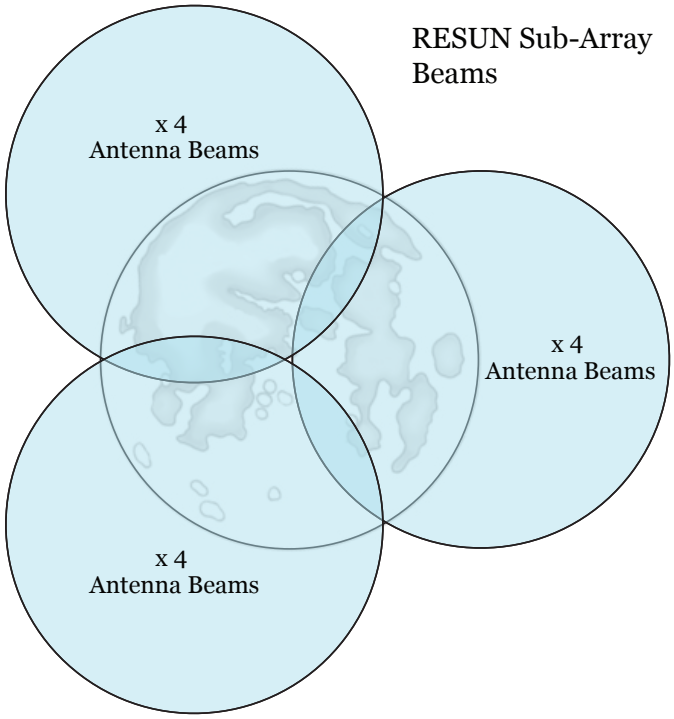

Figure 3.1: Subarray beam geometry for the RESUN experiments.

1465 MHz. The frequency range provided a good compromise between maximum aperture and low energy sensitivity (for discussion, refer to Sec. 4.2). Right and left polarization measurements in each frequency band were combined, resulting in an effective bandwidth of 200 MHz. The EVLA antenna FWHM primary beam in this frequency range is ~ 30 arcmin. Therefore, approximately one third of the lunar limb is illuminated by a single sub-array. Considering only the frequency range pertaining to the RESUN experiment and revisiting Equations 2.5, 2.6, the Ĉerenkov burst emission is characterized by a full angular width of $\sim 1.7^{\circ}$ and a peak ($\theta = \theta_c$) free-space electric field of

$$\mathcal{E}^c_{max}(E) = 0.024 \left(\frac{E}{ZeV}\right) \ \mu V \ \mathrm{m}^{-1} \ \mathrm{MHz}^{-1}. \tag{3.1}$$

Table 3.1: System parameters for the 200-hr (Phase-B) RESUN observation.

ν	$\Delta\nu$	N_a	N_s	$\mathcal{E}_{min}$	E_{min}
1360-1400, 1440-1490	200	4	8	0.017	0.69

Units: ν (MHz), $\Delta\nu$ (MHz), $\mathcal{E}_{min}$ (μV m^{-1} MHz^{-1}), E_{min} (ZeV)

3.1.1 Minimum Detectable Electric Field

The RMS electric field fluctuations of a radio receiver with system temperature T_{sys} and bandwidth $\Delta\nu$ can be calculated by equating the shot noise power of the receiver to the power associated with a radiation field $\mathcal{E}$ illuminating the telescope area A_e,

$$\frac{\eta\ k_b T_{sys}}{\Delta\nu} = \frac{\mathcal{E}^2}{Z_0} A_e$$

so that the RMS field due to detector noise fluctuations is given by

$$\mathcal{E}^d_{RMS} = \left(\eta\ \frac{k_b T_{sys} Z_0}{A_e\ \Delta\nu} \right)^{\frac{1}{2}} \tag{3.2}$$

where η is a dimensionless constant of order unity which depends on the polarization properties of the telescope feed and radiation, k_b is Boltzmann's constant, and $Z_0 = 377\ \Omega$ is the impedance of free space. The minimum detectable electric field is then the RMS field times a multiple n_σ which is determined by the detection threshold described in section 3.1.2. For the RESUN search ($\eta = 2$ for linearly polarized radiation and circularly polarized feeds, $T_{sys} \sim 120$ K pointing on the lunar limb, $\Delta\nu = 200$ MHz, $A_e = 343$ m^2) this evaluates to

$$\mathcal{E}^t_{min} = \ n_\sigma \cdot \mathcal{E}^d = 0.004\ n_\sigma\ \mu V\ \text{m}^{-1}\ \text{MHz}^{-1}. \tag{3.3}$$

By equating Equations 3.1 and 3.3, the minimum detectable incident neutrino energy for RESUN can be expressed as

$$E_{min}\ =\ 0.69\ \text{ZeV}. \tag{3.4}$$

3.1.2 Detection Threshold

At each detector, a threshold level must be set to discriminate against false pulse detection arising from statistical noise fluctuations. Assuming the receiver noise voltage obeys Gaussian statistics and that the receiver maintains a linear response within the voltage range of the fluctuations (see the calibration section in Chapter 5 for a test of this criteria), the probability of a sample signal x exceeding a specified threshold n_σ is given by

$$p_o(x > n_\sigma) = \frac{1}{\sqrt{2\pi}} \int_{n_\sigma}^{\infty} exp\left(-\frac{x^2}{2}\right) dx = \text{erfc}\left(\frac{n_\sigma}{\sqrt{2}}\right) \tag{3.5}$$

where $erfc$ is the complementary error function. For fast sample times, the false signal rate can be quite high, even for very high threshold values. For example, with a 100 MHz sample rate (10 ns samples) and a 6 σ threshold, one expects an accidental trigger approximately once every 5 seconds.

The primary beam of a radio telescope will illuminate an area on the lunar surface with a range of geometrical delays corresponding to a window of n_s time samples (cf. Fig. 3.2). Assuming $p_0 << 1/n_s$, The probability p_w of a pulse exceeding the threshold level in the window of n_s samples is simply

$$p_w(\sigma_t, n_s) = 1 - [1 - p_o(\sigma_t)]^{n_s} \sim n_s \cdot p_o(\sigma_t). \tag{3.6}$$

For an array of n_a telescopes whose primary beams are coincident on the Moon, the joint probability p_j that a statistical fluctuation will exceed the threshold level at all telescopes is the product of the individual antenna detection probabilities, where each antenna may have a different signal to noise ratio and corresponding threshold level. Thus, the joint probability of an accidental trigger in time window

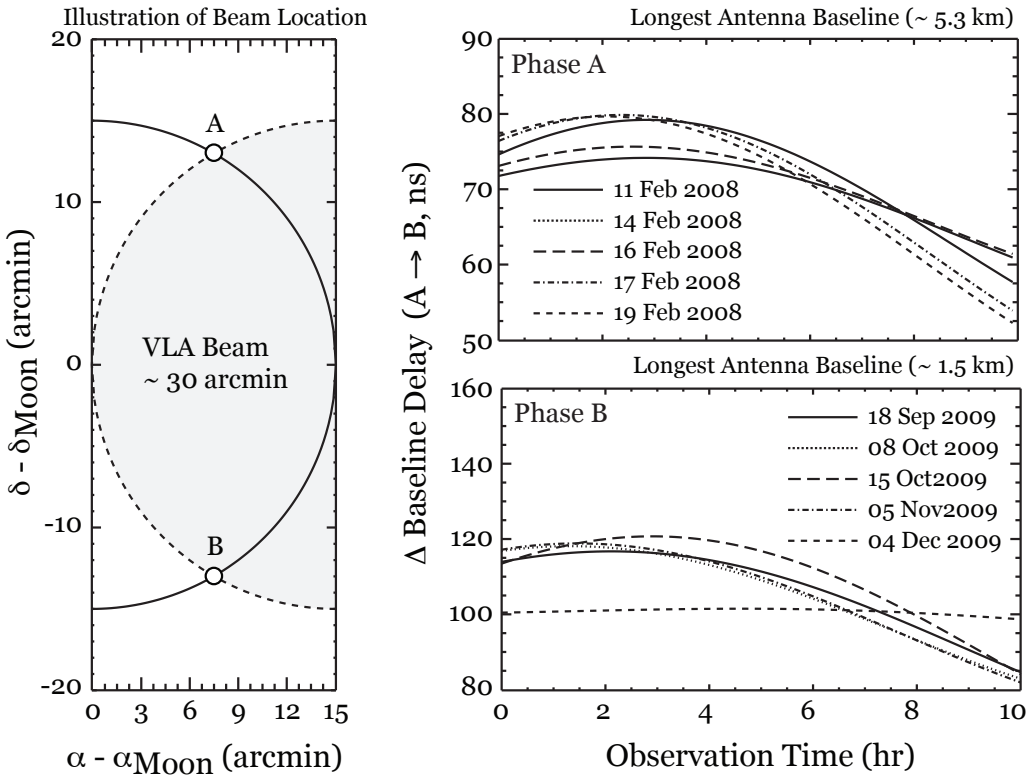

Figure 3.2: The expected change in the differential delay (the observed geometrical delay between detector elements) for lunar limb sources at points A and B for the longest RESUN sub-array baselines on 5 sample observing epochs. While each point has a different corresponding differential delay, both points are located within a single antenna primary beam and are indistinguishable.

of n_s samples (after correction for geometrical delays) for n_a antennas is

$$p_j(\sigma_t, n_s, n_a) = n_s^{(n_a-1)} \prod_{i=1}^{n_a} p_0(\sigma_{ti}) \tag{3.7}$$

which accounts for the possibility of different threshold levels σ_{ti} for each antenna.

Figure 3.3 illustrates the effect that large numbers of antennas n_a has on the detection threshold. As the number of elements increases, the detection threshold n_σ (and therefore the minimum sensitivity) initially decreases rapidly for a fixed number of accidental events. However, the gain to the minimum sensitivity becomes less pronounced after approximately four antennas. For this reason, RESUN

uses sub-arrays of four antennas, as the increase in equipment cost associated with sampling additional antennas is not adequately offset by the increase in neutrino energy sensitivity.

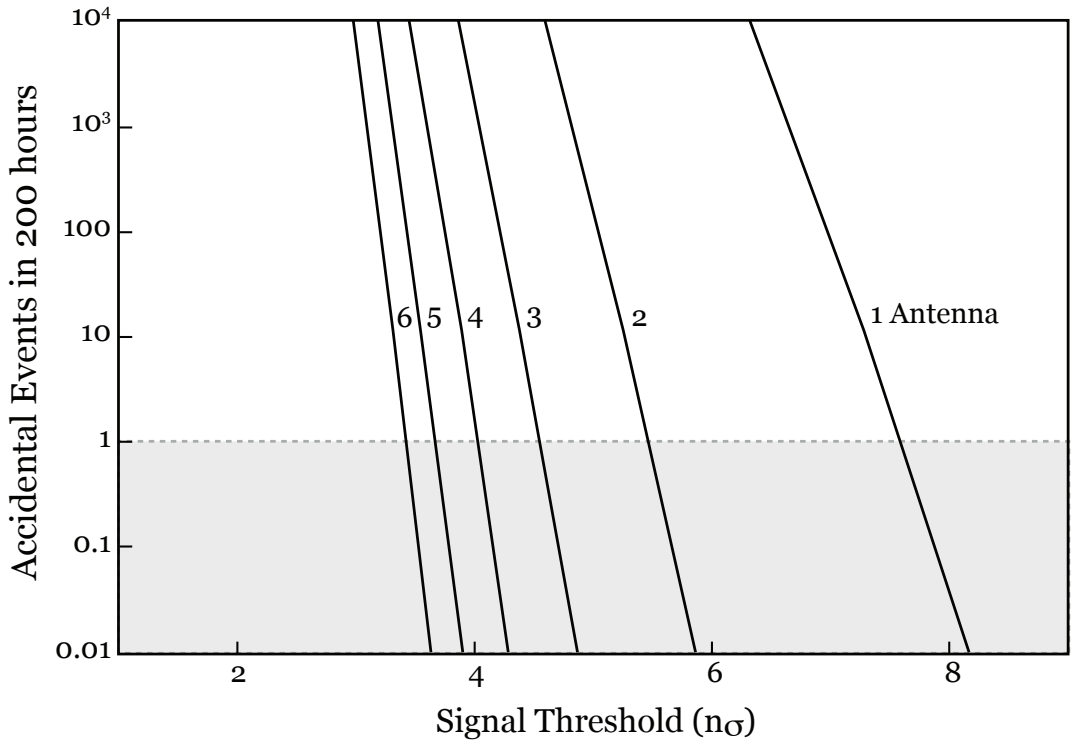

Figure 3.3: Expected number of accidental delay coincident events in 200 hr vs. signal threshold level using a 100 ns uncertainty window and one through six antennas. The shaded horizontal region indicates antenna number - threshold combinations that result in an accidental detection rate of less than 1 per observing period.

3.2 Multi-Antenna Pulse Detection Scheme

RESUN utilized high speed data acquisition devices to record antenna pulses exceeding a set threshold and save these candidate events to disk. The stored events were then compared offline with pulses observed by other sub-array elements, checking for 4-antenna pulse coincidences. A wave front originating from the Moon will illuminate all four antennas with differential time delays dictated by instrumental

and time-dependent geometrical delays. Hence, UHE neutrinos of sufficient energy produce four threshold events (suitably displaced in time) per lunar interaction.

The down-converted waveform at each antenna were sampled using FPGA-based digital signal processors developed by the CASPER laboratory at U. C. Berkeley (Parsons et al., 2008). Each subsystem module (one per sub-array) consisted of two dual-channel 8-bit analog to digital converters (ADCs) attached to a Internet Break-Out Board (iBOB), which provided Internet Protocol (IP) based configuration and high speed ($\sim$ 5 Mb/s) data transfer to a host computer (see Fig. 3.4). The raw input data stream consisted of four channels (one from each telescope) that were simultaneously sampled every 10 nanoseconds using a common sampling clock. In order to avoiding recording all bits, a logic-trigger was developed which only transfers the channel values and corresponding time stamps when the signal level in any one channel exceeds a predefined threshold. This resulted in a significant decrease in the storage of uninteresting pulses while still retaining all candidate events (cf. Sec. 3.1.2). A block diagram of the data acquisition system in shown in

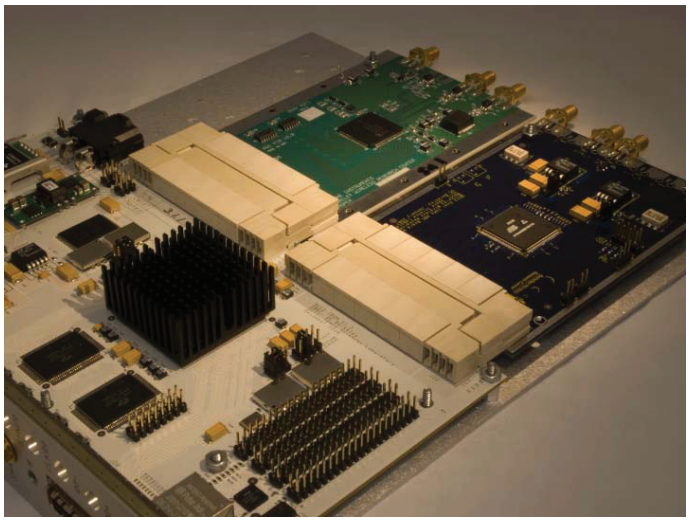

Figure 3.4: Data acquisition hardware showing two, 2-port ADCs connected to an internet breakout board (iBOB) hosting a FPGA.

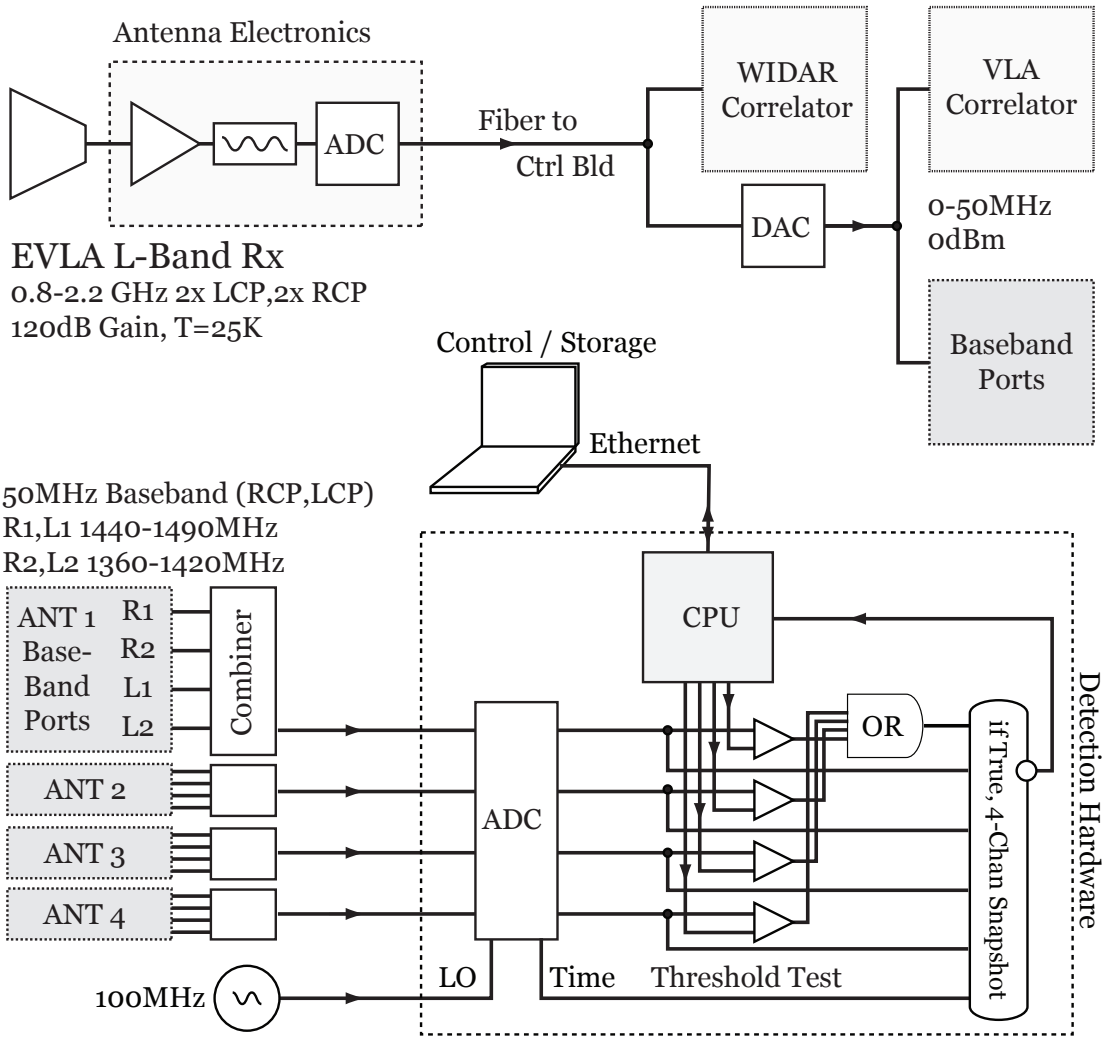

Figure 3.5: Block diagram of RESUN pulse detection scheme for a 4-antenna sub-array. RESUN bypasses the EVLA-WIDAR and VLA correlators and down-converted antenna signals are accessed instead via the VLA baseband ports.

Fig. 3.5. Further details about the trigger logic and FPGA design can be found in Appendix A.

Candidate events were compared with pulse detections from 3 other sub-array antennas by calculating the expected sum of the instrumental and geometrical delays, then searching for 4-channel coincident events in delay uncertainty windows centered at the expected pulse arrival times. The geometric delay for sources

along the illuminated chord of the lunar limb was calculated using the Chapront ELP2000/82 algorithm (Meeus, 1998) which has < 10 arcsecond positional uncertainty and < 1 km uncertainty in lunar distance. EVLA optical fiber transmission times were used for the instrumental delays. The consequent instrumental and geometrical delays have an uncertainty of ~ 5 ns, a value smaller than the 10 ns sample time. Instead, the delay window size was dominated by the delay range expected for sources distributed over the part of the lunar limb illuminated by the primary beam of the antennas (Fig. 3.2). The range of delay window widths varied with projected antenna separation, but was generally in the range of 50 ns to 80 ns. For more detail on the candidate event post-processing, see Appendix C.

3.3 Disadvantages of Single Element Designs

While the RESUN experiment utilizes a multi-element delay-coincidence detection scheme, lunar neutrino searches using single element detectors like Parkes (Hankins et al., 1996) and Kalyazin (Beresnyak et al., 2005) must rely on ionospheric dispersion to distinguish Ĉerenkov events from RFI. Radio signals traveling through the Earth's ionosphere experience a frequency-dependent delay given by

$$t(\nu) = 13 \text{ ns } (\frac{n_e}{10^{17} m^{-2}})(\frac{\nu}{GHz})^{-2} \tag{3.8}$$

where n_e is the column density of ionospheric electrons (typically $n_e \sim 10^{17} m^{-2}$ at night, $10^{18} m^{-2}$ during daytime) and ν is the frequency. At an observing frequency of 1.5 GHz, this results in a broadening of the pulse by approximately 5 ns depending on time of day. Since changes in the electric field strength scale like the square root of changes to the pulse power, ionospheric broadening at high frequencies only has a small effect on the pulse field amplitude. However, the dispersion effect is much stronger at lower frequencies, where observations at 150 MHz result in a factor of 100 increase in the ionosphere induced pulse broadening corresponding to a factor

of 10 decrease in received electric field strength. The effect is also highly variable, as the electron column density can change by orders of magnitude in short ($<$ hr) timescales. It is for these reasons that a multi-element detector scheme is preferred and the focus of project RESUN.

CHAPTER 4
DETECTION APERTURE FOR ĈERENKOV RADIO EMISSION

The rate at which Ĉerenkov bursts of lunar origin are observed by a detector can be conceptualized as the product of the incident neutrino flux (neutrinos per area per solid angle) multiplied by an aperture which has units of area times solid angle (Williams, 2004). The magnitude of the aperture will depend on both lunar cross-sectional area and the physical parameters of the detector (such as observing frequency, bandwidth, detector sensitivity and collection time). Several groups have addressed this problem for specific experiments by developing Monte Carlo simulations, following ray paths for an variety of neutrino flux models (Gorham et al., 2000; Williams, 2004; Gusev et al., 2006; James et al., 2007; James and Protheroe, 2009).

Project RESUN instead uses an analytic expression for the lunar detection aperture which is in good agreement with recent Monte Carlo simulations and in transparent to the underlying physics. The scaling approximations made in the aperture model also inform tradeoffs in the design of detection experiments. Note that the aperture formulation described in this chapter assumes an isotropic incident neutrino flux. However, this approach can also be generalized to a direction-dependent case (e.g., James et al., 2007).

4.1 Lunar Aperture to Incident UHE Neutrinos

The effective aperture A_e can be written as the product of the cross-sectional area of the Moon, the total solid angle of incident neutrinos (4π for isotropic neutrino flux), and a detection probability P which takes into consideration the interaction specifics,

$$A_e(E, \nu, \mathcal{E}^d_{min}) = A_0 \cdot P(E, \nu, \mathcal{E}^d_{min}) \ , \tag{4.1}$$

where E is the neutrino energy, ν is the observing frequency, $\mathcal{E}^d_{min}$ is the minimum detectable electric field strength of the detector (see Chapter 3), and A_0 is the geometric lunar aperture (Gayley et al., 2009; Williams, 2004),

$$A_0 = 4\pi \cdot (\pi R_m^2) \ ,$$

where R_m is the radius of the Moon. Note that the aperture has units of physical area times solid angle. The probability P is the fraction of neutrinos entering the Moon at energy E whose radio pulse will be detectable with a telescope (detector) having minimum electric field sensitivity $\mathcal{E}^d_{min}$ at frequency ν.

An approximate expression for P can be written

$$P = P_o \left(\Psi_{dr} + \Psi_{ds} + \Psi_u\right) \tag{4.2}$$

where

$$P_o = \left[\frac{n_r^2 - 1}{8n_r}\right] \frac{\lambda_\mathcal{E}}{\lambda_\nu} f_0^3 \Delta\theta_H$$

and the three bracketed terms Ψ_{dr}, Ψ_{ds}, Ψ_u represent the contributions from downward incident neutrinos on a smooth surface, downward neutrinos on a rough surface, and upward traveling neutrinos respectively. The contribution of each term to the total detection aperture is shown in Figure 4.2.

For a smooth lunar surface, the role downward incident neutrino in the lunar detection aperture is expressed as

$$\Psi_{dr} \ = \ f_o \ \Delta\theta_H \tag{4.3}$$

where the dimensionless scaling parameter f_o is the ratio of the thickness of the Ĉerenkov cone e^{-1} full thickness to the cone thickness at the minimum detectable electric field $\mathcal{E}^d_{min}$ (cf. Fig. 4.1),

$$f_0(E,\nu) = \sqrt{\ln\left[\frac{\mathcal{E}^c_t(E,\nu)}{\mathcal{E}^d_{min}(\nu)}\right]} \ . \tag{4.4}$$

However, the moon is not smooth. It is instead almost entirely comprised of

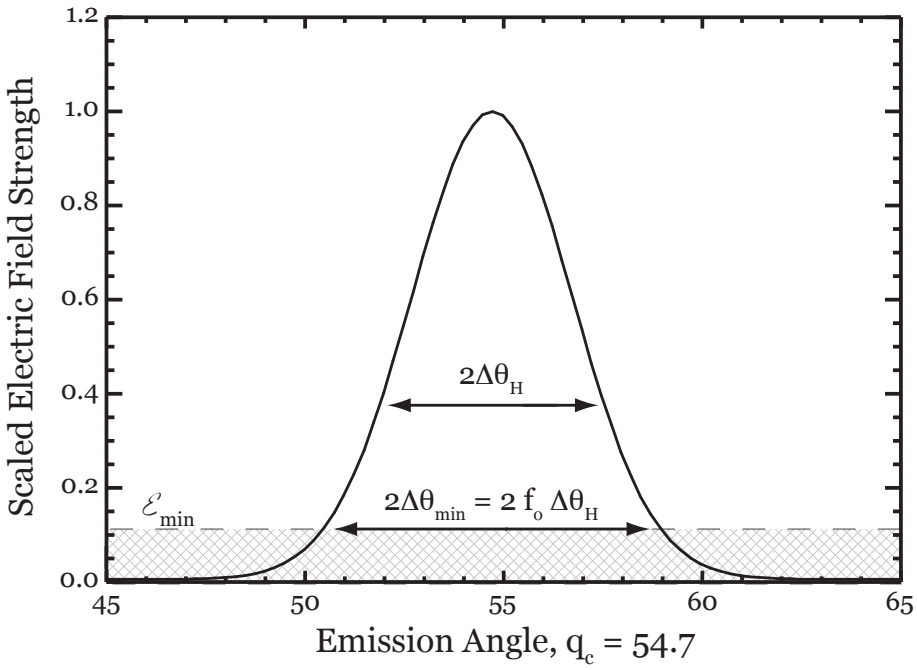

Figure 4.1: Cerenkov cone angular profile at $E = 10^{21}$ eV and $\nu = 1$ GHz. The dimensionless factor f_o is the ratio of the cone thickness at threshold $\mathcal{E}_{min}$ to the $1/e$ width.

random surface variations which can alter the Ĉerenkov cone ray path. Shepard et al. (1995) analyzed radar measurements of the lunar surface and determined that the surface irregularities have an observation frequency dependent fractal (self-similar) distribution, with a root-mean-square roughness angle of

$$\sigma_o(\nu) = \sqrt{2}\ \tan^{-1}\left(0.29\ \lambda^{-0.22}\right) = \sqrt{2}\ \tan^{-1}(0.14\ \nu^{0.22}) \tag{4.5}$$

where λ is the spatial scale in cm, ν in GHz, and σ_o is in radians. For the RESUN search ($\nu = 1.40$ GHz), we obtain $\sigma_s = 12.1^{\circ}$. The effect surface roughness has on the lunar aperture for downward incident neutrinos is

$$\Psi_{dr} \ = \ \frac{16}{3\pi^{1.5}}\ \sigma_o\ . \tag{4.6}$$

While roughness may cause the lunar surface to be slanted at any angle for any given ray-path, favorable surface tilts increase the number of escaping rays more

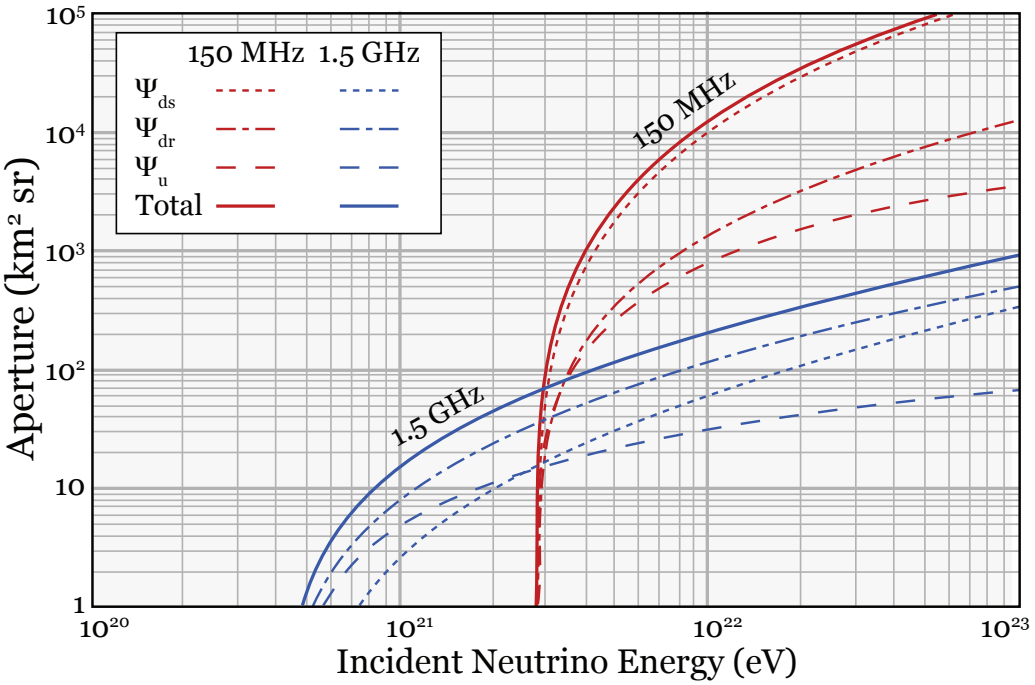

Figure 4.2: Total aperture versus neutrino energy at threshold field $\mathcal{E}_{min} = 0.01$ μV m^{-1}MHz^{-1} and two observing frequencies: 150 MHz (solid red line) and 1.5 GHz (solid blue line). The contribution from each of the three terms in equation (4.2) is also shown. At both frequencies, downward-directed terms have the largest contribution except near the lower cutoff energy. For energies well above the cutoff energy, surface roughness has the largest contribution, except at low frequencies, where the smooth surface term already dominates without assistance from roughness.

than unfavorable tilts increase internal reflection. This is because unfavorable tilts act disproportionally on ray-paths that were already near the critical angle and have little to no signal prior to the alteration. The enhancement to the number of exiting rays becomes especially important at high observing frequencies ($\nu \gtrsim 300$), for it is at these frequencies that the root-mean-square surface roughness angle exceeds the Ĉerenkov width.

The lunar detection aperture for Ĉerenkov bursts due to upward incident UHE neutrinos depends only on the maximum acceptance angle α_o discussed in Section 2.3.2 of Chapter 2. Again applying a "near-surface" approximation, the functional

contribution to the detection aperture for upward incident neutrinos is

$$\Psi_u \;=\; \frac{16}{3}\,\alpha_o\;. \tag{4.7}$$

Figure 4.3 displays the lunar detection aperture as a function of antenna sensitivity $\mathcal{E}^d_{min}$ and observing frequency ν for UHE neutrino energies exceeding $E > 10^{21}$ eV (a) and $E > 10^{22}$ eV (b). Figure 4.4 is a second plot of the lunar aperture for a family of antenna sensitivities at fixed frequencies of 1.5 GHz (a) and 150 MHz (b).

4.2 Optimal Observing Frequency

The analytic solution to the lunar detection aperture detailed in the previous section provides valuable insight into trade-offs between sensitivity, target neutrino energy, and observation frequency. The minimum sensitivity of the RESUN experiment is essentially a fixed value, set by the single antenna sensitivity and the maximum capture rate of the data acquisition system. Given this sensitivity lower

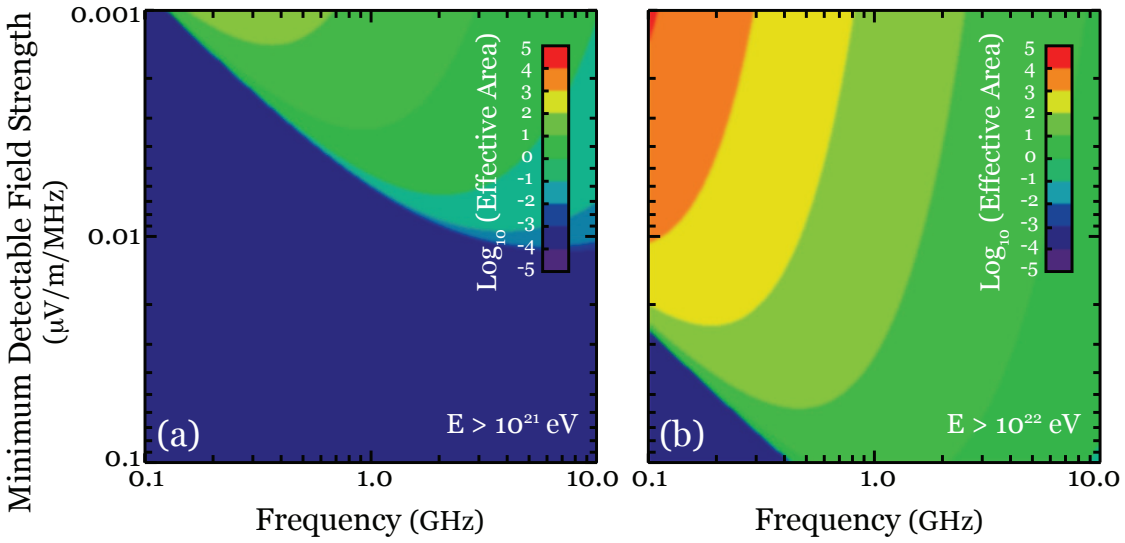

Figure 4.3: (*a*) Aperture vs. minimum detectable electric field and observing frequency for neutrinos with energies $E > 10^{21}$ eV. (*b*) Same as panel (*a*), but for neutrino energies $E > 10^{22}$ eV.

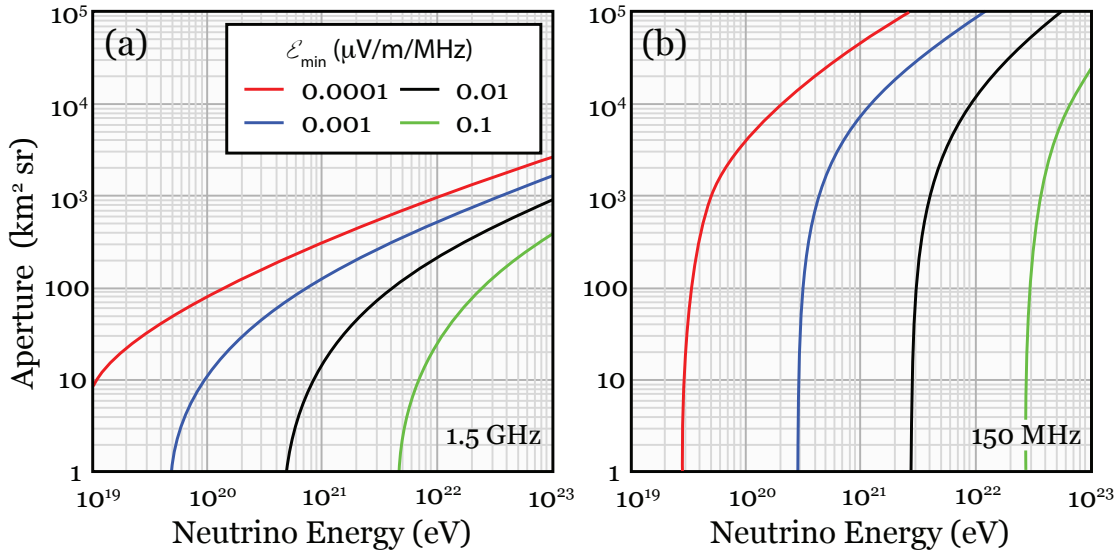

Figure 4.4: (a) Aperture vs. neutrino energy at observing frequency $\nu = 1.5$ GHz using telescopes with minimum detectable electric field $\mathcal{E}_{min}$= 0.0001, 0.001, 0.01, and 0.1 μV m^{-1}MHz^{-1} . (b) Same as panel (a), but at observing frequency $\nu =$ 150 MHz. Note the trade-off between collecting area and minimum detectable neutrino energy as frequency is changed.

limit ($\mathcal{E} \sim 0.02\mu V$ m^{-1} MHz^{-1} for RESUN), and that neutrino energies exceeding a few ZeV seem unlikely from cosmogenic (GZK) models, the aperture model predicts that frequencies near 1 GHz provide the best compromise between low-energy cutoff and maximum aperture. This is illustrated in Figure 4.5 where the effective aperture is plotted as a function of neutrino energy for fixed detector sensitivity and a range of observing frequencies from 0.1 GHz to 10 GHz. Note that the sharp low-frequency cut-off is a result of $f_0 \rightarrow 0$,which for fixed telescope sensitivity occurs at higher neutrino energy as the observing frequency is lowered..

4.3 Predicted Count Rate

The expected number of detections n in exposure time t is the product of the neutrino flux $I(E)$ times the effective target area $A_e(E)$ integrated over the solid

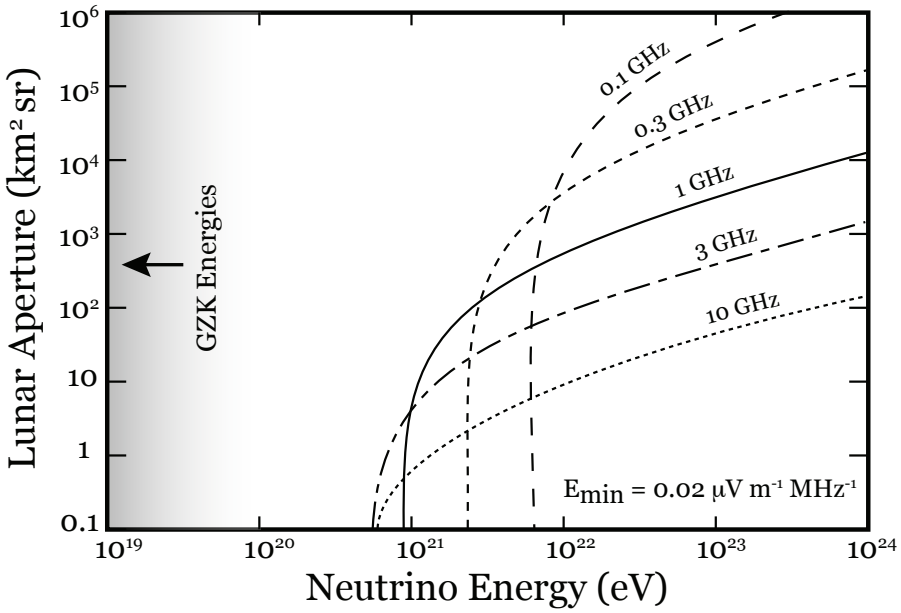

Figure 4.5: The effective lunar aperture from Equation 4.2 as a function of neutrino energy and observing frequencies between 0.1 GHz and 10 GHz given a fixed detector sensitivity E_{min}= 0.02 μV m^{-1} MHz^{-1}.

angle and all detectable energies.

4.3.1 Isotropically Distributed Sources

For the case of an isotropic distributed of neutrino sources, the expected count in time t is

$$n_{iso} = t \int_{E_{min}}^{\infty} dE\ I(E)\ A_e(E)\ . \tag{4.8}$$

Using several isotropic neutrino generation models $I(E)$ and Eqn. 4.8, the predicted number of detections expected for the RESUN observations is plotted in Figure 4.6. The 1-count accidental rate and the minimum electric field sensitivity for each experiment are also given. The intersection between the accidental rate and the horizontal one count line is a fiducial point: A search that could detect neutrinos from a given model must have its fiducial point below the model. The cross-hatched

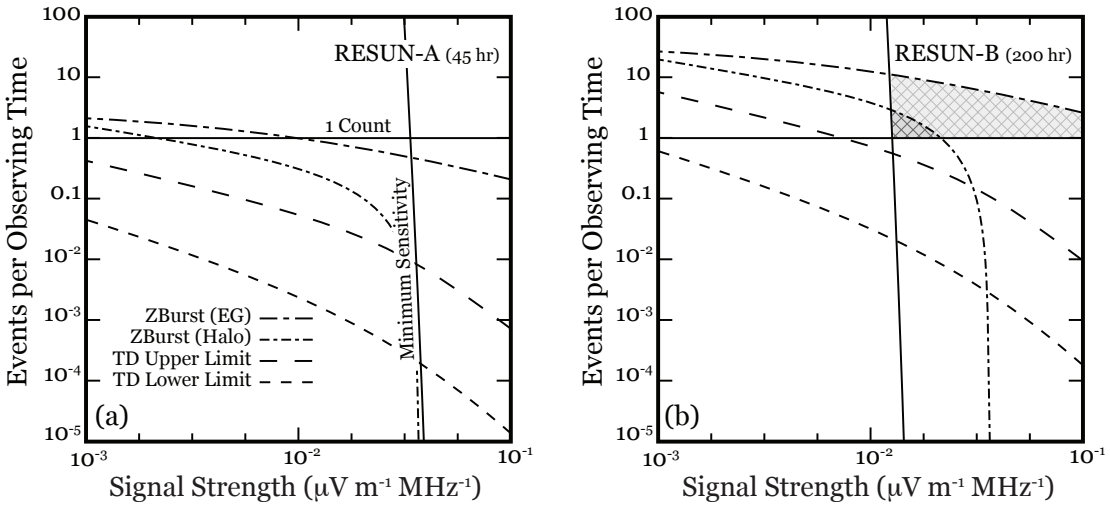

Figure 4.6: Expected number of events versus burst electric field strength for the RESUN-A (45hr) and RESUN-B (200 hr) experiments. In each case, the solid vertical line represents the minimum sensitivity of the observation given by equations 3.3 and 3.7, while the labeled dotted and dashed lines are the expected rates for neutrino-production models (see legend). The shaded areas are regions where model counts exceed the accidental counts. In order to detect neutrinos from a given source model, the intersection between the accidental rate (nearly vertical line) and the unity count horizontal line must lie below the model's curve.

area is the region for which model counts exceed accidental counts. While RESUN-A does not have any cross-hatch areas (i.e, does not test any proposed isotropic models), RESUN-B probes both halo (dash-dot) and extragalactic (bold dash-dot) Z-burst models(Fodor et al., 2002; Kalashev et al., 2002), with ∼1-10 expected counts. Note that recent radio observations by ANITA (Gorham et al., 2009) and FORTE (Lehtinen et al., 2004) along with neutrino mass limits set by WMAP (Crotty et al., 2004; Fogli et al., 2004) disfavor the Z-burst mechanism for UHE Neutrino generation. The RESUN non-detection is a confirmation of these results.

4.3.2 Point Sources

For a UHE neutrino point source, the effective lunar aperture to isotropic sources from Equation 4.1 must be modified by the lunar solid angle on the sky to estimate the expected count rate. The analytic results of Gayley et al. (2009) (summarized in Sec. 4.1) can be used to approximate the lunar solid angle (Ω_A) by noting that at high frequencies ($\nu \gtrapprox 1$ GHz) the downward neutrino acceptance angular spread is dominated by the surface roughness angle σ_0. The expected count rate for a point source is then approximated as

$$n_p \approx \frac{t_p}{\Omega_A} \int_{E_{min}}^{\infty} dE\ I(E)\ A_e(E)\ , \tag{4.9}$$

where

$$\Omega_A \approx\ {\sigma_0}^2$$

and t_p is the total time that the source is within the aperture solid angle.

For lunar search experiments, the beam tracks the Moon's motion on the celestial sphere. The maximum point-source observation time for a single epoch can then be written

$$t_p = 2 \times \frac{29.5^h}{2\pi} \times \theta_{eff} \sim 200^h \times \theta_{eff}$$

where θ_{eff} (radians) is the effective angular extent of the aperture solid angle as it transects the point source. Again, since the aperture is dominated by the lunar roughness term in equation 4.2, we can write

$$\theta_{eff} \approx\ \sqrt{\Omega_A} \approx\ \sigma_0\ .$$

4.3.3 Flux Limits for Non-Detection

For experiments with a null detection, at 90% confidence level the neutrino flux upper limit is 2.3 times the differential flux upper limit, assuming Poisson counting statistics. Using to the commonly plotted quantity $F(E) = E\ dI(E)/dE$, the

upper limit for a non-detection in a given observing time t is

$$F_{iso}(E,t) < \frac{2.3}{t \cdot A_e(E)} \tag{4.10}$$

while a single point source of neutrinos, the corresponding upper limit is

$$F_p(E) < \frac{2.3\ \Omega_A}{t_p \cdot A_e(E)} \tag{4.11}$$

where t_p is the total time that the source is within the aperture solid angle.

CHAPTER 5
RESUN OBSERVATIONS AND RESULTS

Project RESUN is comprised two phases: RESUN-A, a 45-hour proof-of-concept search completed in February 2008, and RESUN-B (the main focus of the RESUN project), a 200-hour search in the fall of 2009 with significantly enhanced limb coverage, wider total bandwidth, and lower pulse detection threshold. This section describes the results from each search, along with pertinent instrument response and calibration information.

5.1 Instrument Calibration

The RESUN observations were made in coincidence with receiver and correlator upgrades as the classic VLA system transitioned to the current EVLA (For a review of the VLA to EVLA transition, see Butler et al. 2006). During this period, both VLA and EVLA antennas were available which have different characteristics. In order accurately record and report the presence of nanosecond-scale radio bursts, it was important that the behavior of each antenna and corresponding receiver electronics was understood. Of greatest importance was a detailed understanding of the radio receiver dynamic range, receiver noise characteristics, system response to nanosecond-scale incident pulses, and the instrumental delay between the antenna and the baseband access ports.

5.1.1 Receiver Dynamic Range

The anticipated peak electric field strength for neutrino-induced Ĉerenkov bursts (Eqn. 3.1) can be many times larger than the RMS receiver sensitivity (Eqn. 3.3). In general, radio receivers are not designed to operate many orders of magnitude higher than the RMS noise level. This is mainly due to functional

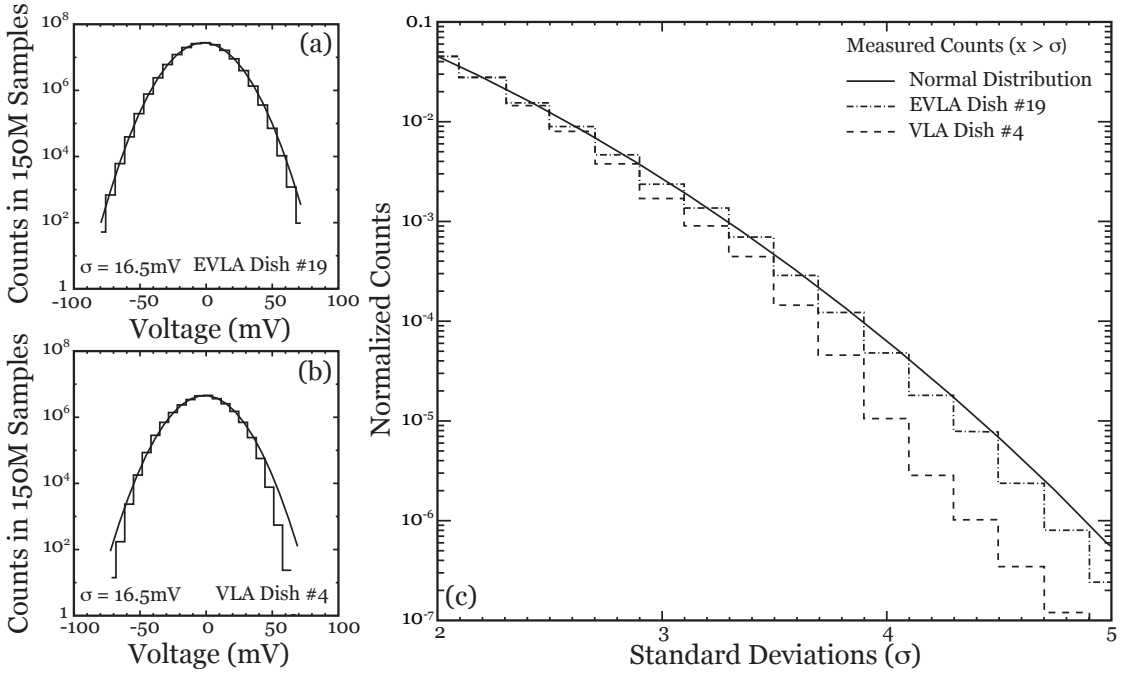

Figure 5.1: Comparison of measured count rates for sample VLA (antenna 4, dashed line), EVLA (antenna 19, dashed-dot line) receivers, and Gaussian statistical model (solid line) versus threshold level for sampled voltage output of square-law detector (proportional to input power). Note that while the VLA receiver shows significant saturation above 3σ, there is very little saturation for the ELVA system for signals $\lesssim 5\sigma$, well above the RESUN threshold.

limitations in the receiver amplifiers. However, a large voltage dynamic range is critical to Ĉerenkov pulse detection experiments.

In order to determine the most appropriate antennas for RESUN, the receiver output voltage dynamic range was measured for both VLA and EVLA antennas by comparing histograms of sampled receiver output voltage to a Gaussian statical model (Fig. 5.1). While each receiver is designed to have nearly identical RMS voltage fluctuations, histograms plotted to high sigma revealed that the classic VLA receivers were unusable for the RESUN search since they saturated well below the target RESUN threshold of $n_\sigma = 4$. However, the new EVLA receiver systems were in excellent agreement with Gaussian statistics until voltage excursions approached

5 σ. It was then determined that the RESUN search could only use sub-arrays comprised entirely of EVLA antennas.

5.1.2 Receiver Response to Nanosecond Pulses

Unlike the fully analog VLA signal path, the transitional EVLA signal path transitions changed from initially analog, to digital, then back to analog in order to maintain compatibility with the classic VLA correlator. With each transition existed the possibility of signal dispersion which would weaken or completely mask short duration signals. Two tests were performed to observe the receiver response to nanosecond-scale pulses. In the first test, a pulse-modulated monochromatic sine wave (1465 MHz, down-converted by the receiver to 25 MHz) was transmitted from the VLA operation center (cf. Fig. 5.2, Bld. 14) toward an antenna positioned nearby at location "DW7". The modulation width was slowly varied from 400 ns to 25 ns and the receiver response was both recorded graphically using an oscilloscope and with the RESUN data acquisition (DAQ) system. Figure 5.3 shows the measured response for 250 ns and 25 ns wide pulse modulations. RESUN DAQ results can be found in Appendix A.

As a second test, pulse-modulated broadband (0.5-2 GHz) noise pulses were injected directly into the receiver system[1] using a portable pulse generator which was later used to verify the instrumental delays (see Sec. 5.1.3). The pulse modulation width was again varied from 400 ns to 25 ns with the receiver output recorded graphically. In both test, the observed pulse response was consistent with the input signal for all modulation widths.

[1]Pulses were injected into the system after the first low-noise amplifier which is cryogenically cooled and inaccessible

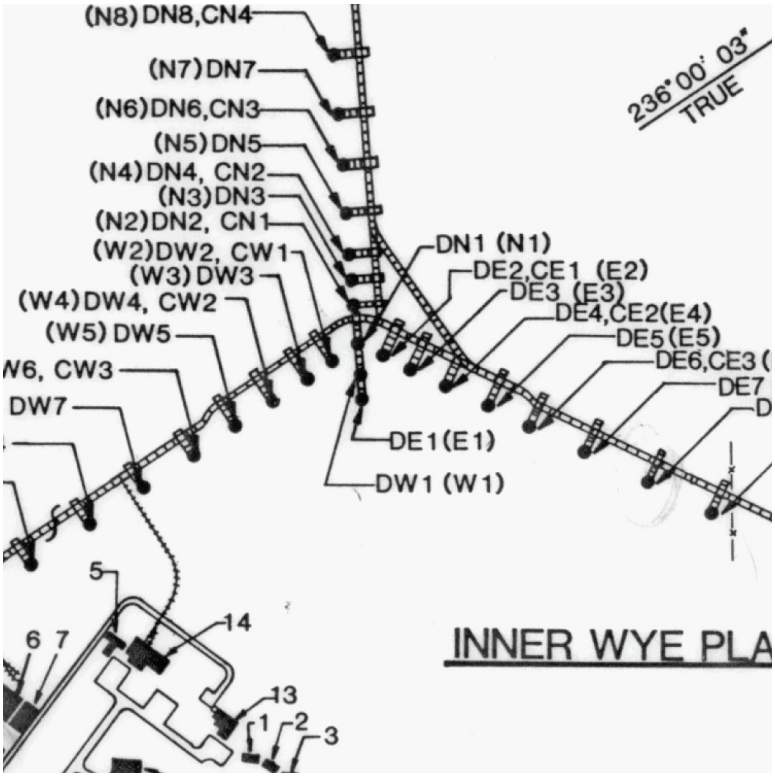

Figure 5.2: Illustration of VLA/EVLA antenna locations from the VLA Greenbook (http://www.vla.nrao.edu/astro/guides/greenbook/) showing the array center (position N1) and the EVLA control building (14). A full version of this image can be found in Appendix A.

5.1.3 Verifying the Instrumental Delays

The delay-coincidence method used in Project RESUN requires very accurate measurements of the propagation delay from the EVLA antennas to the analog baseband ports where signals are sampled. Briefly considered was using an astronomical source for pulse calibration, viz. the giant pulses from the Crab nebula (Bhat et al., 2008) but the rise times are too long ($\sim 0.5\mu s$) and the pulses are too dispersed at 1.4 GHz. Being no natural sources of nanosecond pulses in the sky to verify the pulse detection scheme, we built a broad-band portable pulse generator and flew it 40 m above the center of the VLA using a helium-filled balloon (Fig. 5.4). The portable unit generated 25 ns wide pulses which were amplified and radiated

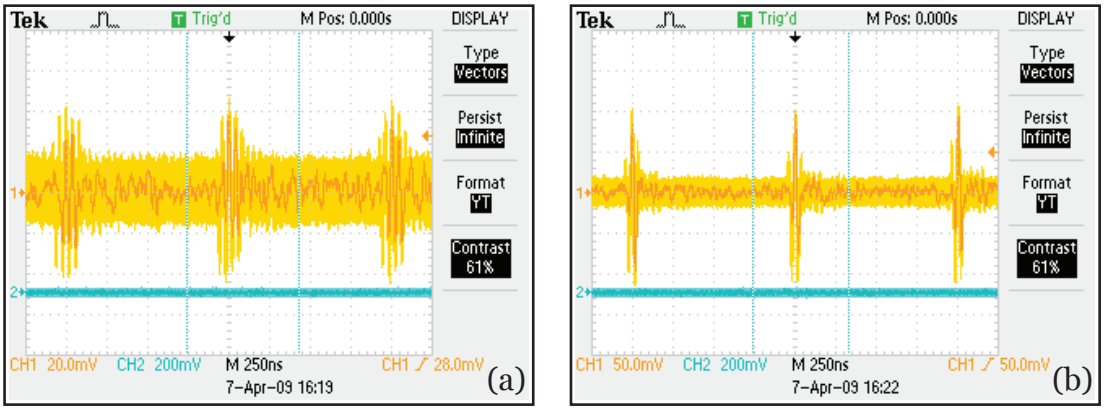

Figure 5.3: Measured EVLA receiver response to a transmitted pulse-modulated sine wave with widths of (a) 250 ns and (b) 25 ns.

from an omni-directional antenna (cf. Appx. B). We pointed three of the subarray antennas at the pulse generator and examined the delays between pulses using both

Figure 5.4: EVLA instrumental delay measurements using a broad-band balloon-borne pulse generator. Image courtesy of Bob Brolio (NRAO).

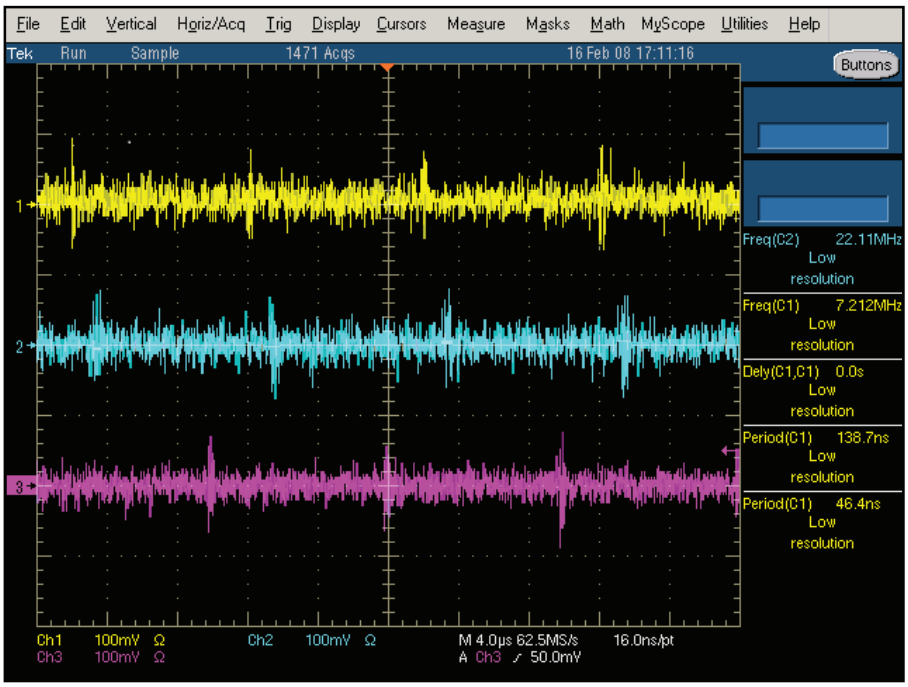

Figure 5.5: Measured pulse arrival times for two EVLA receivers (Channels 1, 2) and one VLA antenna (Channel 3).

realtime oscilloscope traces (Fig. 5.5) and the RESUN DAQ (The fourth antenna could not be tested since the balloon payload was below the minimum antenna elevation of 8°). After calculating the geometric delay to the arial pulse generator and measuring the arival delay, the instrumental delays provided by the EVLA were verified to a precision of ±10 ns.

5.1.4 Verifying the Accidental Detection Rate

To check the pulse detection statistics, the antenna signals were sampled at a threshold value which, based on a Gaussian statistics model of the receiver noise, would result in many spurious coincident-detections. The off-line analysis of candidate events was also performed using a delay window which was a factor of 2 larger than the delay uncertainty. With these parameters (n_σ=3.9, Δt =2 x 100 ns for

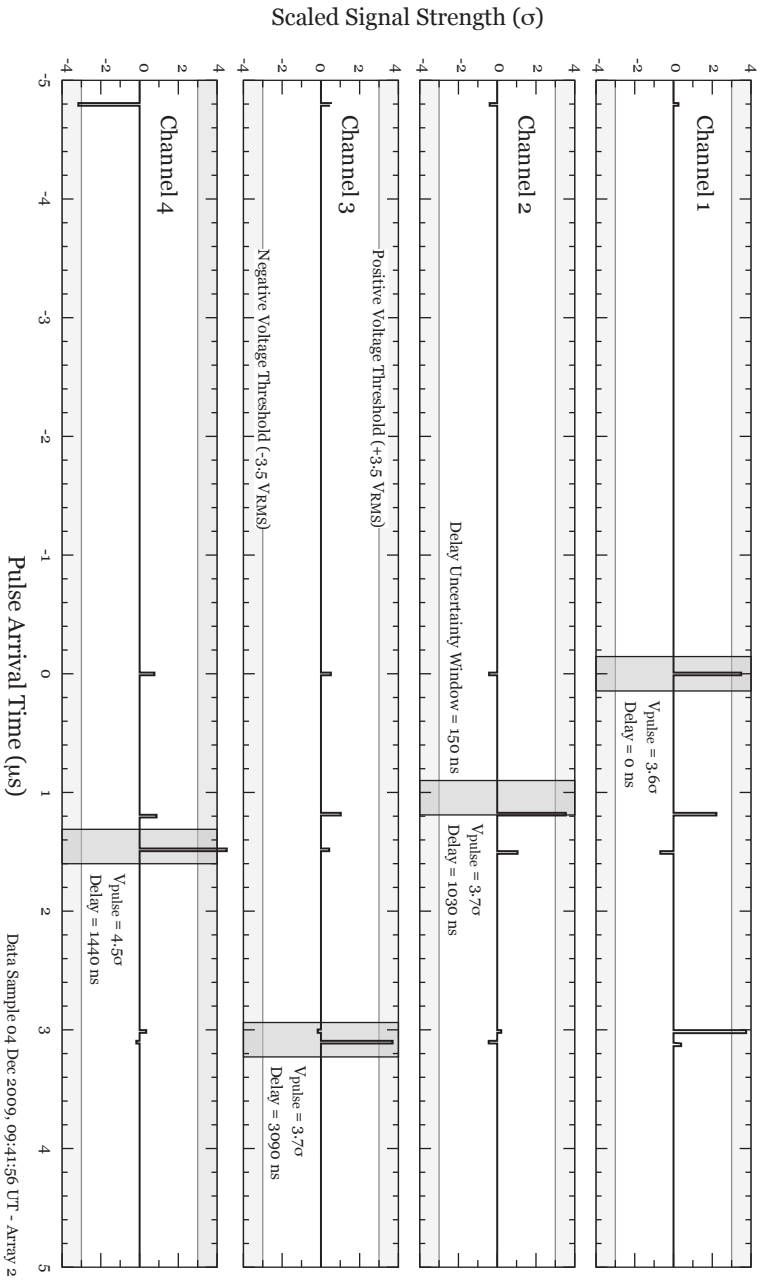

Figure 5.6: Example of four channel accidental trigger with a wide acceptance window. The $> 3.6\sigma$ trigger signal was initiated in channel 0, while the triggers in channels 1-3 were within a $\pm$150 ns tolerance window centered on the corresponding differential (geometric plus instrumental) delays to the Moon.

Phase-A, n_σ=3.5, Δt =2 x 75 ns for Phase-B), a 4-channel accidental coincidence

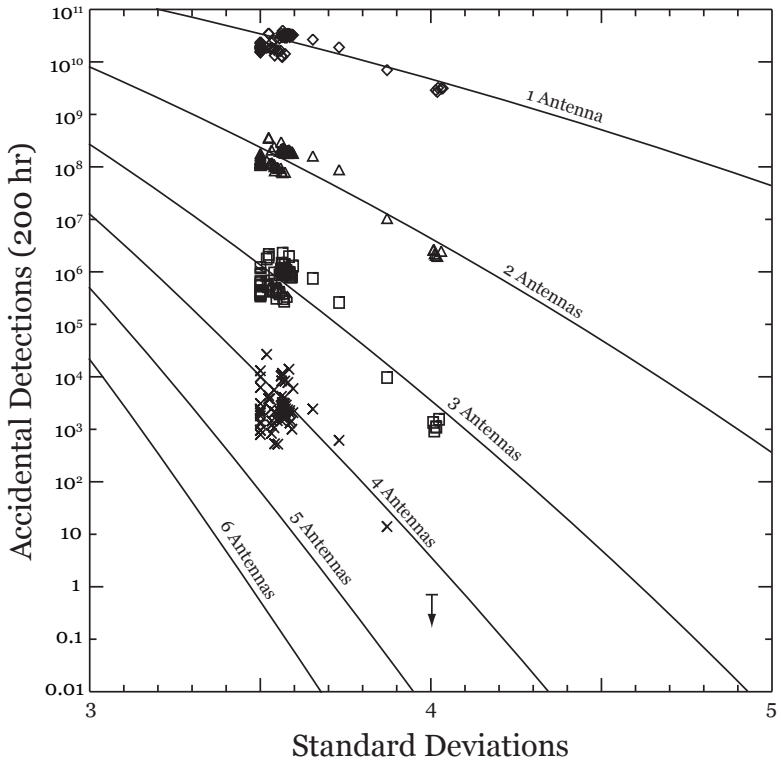

Figure 5.7: Expected number of accidental detections in 200 hours vs. threshold level calculated using equation 3.7. Solid lines represent accidental detection rates for arrays of one to six telescopes using identical threshold levels, 10 ns sampling time, and a 150 ns delay tolerance window. The measured number of accidental detections for each RESUN observation session (scaled to 200 hours) for one (diamonds), two (triangles), three (squares), and four telescope (x's) detection schemes are shown and are in excellent agreement with the noise model.

was observed approximately every minute, with 3-channel and 2-channel coincidence successively more frequency. Figure 5.6 shows an example of an accidental 4-antenna coincidence. The average accidental coincidence occurrence rate for each observing session was then tabulated and compared to the anticipated rate. The measured rates were in good agreement with the Gaussian model rates across the entire range of signal thresholds (Fig. 5.7).

5.2 45 hr RESUN-A Observation

The RESUN-A observation utilized two 4-antenna sub-arrays pointed at the east and west limbs of the moon, recording candidate pulses for a total of 50 hours in five 10 hour sessions between 11 - 20 Feb. 2008. Observations were made in a single 50 MHz band (RCP) centered on 1465 MHz. Unfortunately, two antennas in the eastern sub-array displayed anomalously high suppression of signals greater than 3σ deeming this sub-array unusable. In addition, approximately 5 observation hours were lost as result of bad weather, operator errors, and equipment malfunctions.

No 4-station coincident events greater that a 3.98σ threshold were recoded during a total observation period of 44.95 hours. The corresponding upper limit to the isotropic differential neutrino flux E dN/dE is < 10 km^{-2} yr^{-1} sr^{-1} at 90% confidence level for sources with neutrino energy (E) exceeding $10^{21.6}$ eV and E dN/dE < 1 km^{-2} yr^{-1} sr^{-1} for E $> 10^{23}$ eV. This is (marginally) lower than the published upper limits for lunar detection experiments in this energy range and confirms the GLUE upper limit reported by Gorham et al. (2004).

5.3 200 hr RESUN-B Observation

For the RESUN-B observations, the lunar limb was tracked using three sub-arrays of four antennas (cf. Fig. 3.1) for a total of 25 sessions from August 2009 to December 2009. RCP and LCP signals in two 50 MHz bands centered at 1385 MHz and 1465 MHz were combined prior to digitization. No 4-station coincident events greater than a 3.9σ threshold level during an total observation period of 200 hours. This corresponds to a differential neutrino flux upper limit of E dN/dE < 1 km^{-2} yr^{-1} sr^{-1} at 90% confidence level for isotropic sources with neutrino energy (E) exceeding $10^{21.2}$ eV and E dN/dE < 0.1 km^{-2} yr^{-1} sr^{-1} for E $> 10^{22.5}$ eV. The isotropic flux limit is more than an order of magnitude lower than previously published upper limits for lunar searches, and is incompatible with predicted fluxes

from Z-burst models of neutrino generation (Fodor et al., 2002; Kalashev et al., 2002) consistent with the ANITA lunar ice observation (Gorham et al., 2009) and WMAP neutrino mass limits (Crotty et al., 2004; Fogli et al., 2004).

Figure 5.8a shows the UHE neutrino flux upper limits established by both RESUN Phase-A (dotted line), and RESUN Phase-B (bold dotted line) along with previously reported upper limits from Parkes (Hankins et al., 1996; James et al., 2007), GLUE (Gorham et al., 2004), Kalyazin (Beresnyak et al., 2005), nuMoon (Scholten et al., 2009). Note that all upper limits have been computed using the analytic aperture calculation of Gayley et al. (2009) and do not necessarily agree with Monte Carlo simulations. Results from ice-target searches are shown in Figure 5.8b, highlighting the RICE (Kravchenko, 2006), HiRES (Abbasi et al., 2008), FORTE (Lehtinen et al., 2004), and ANITA (Gorham et al., 2009) experiments. Both figures show isotropic neutrino flux predictions from Z-bursts in the galactic halo and extragalactic background (crosses, Fodor et al. 2002; Kalashev et al. 2002), collapse of the cosmic string loops (green dot-dashed lines, Yoshida et al. 1997), GZK interactions with protons and with heavy ions (blue shaded band, Engel et al. 2001), topological defects (TD, green shaded band, James and Protheroe 2009 and refs.), and Waxman-Bahcall upper limits for no redshift evolution and with redshift evolution (WB, black short dashes, Waxman and Bahcall 1999).

RESUN-B also establishes 90% confidence differential flux limits for 41 AGN sources within 50 Mpc. 17 of these sources are are located more than 10 deg from the celestial equator where Antarctic ice experiments have limited spacial coverage. The point source upper limits are expressed in Tables 5.2 ($> 10\,\mathrm{deg}$), 5.3 ($< 10\,\mathrm{deg}$).

5.4 Isotropic Flux Upper Limits

Table 5.1 lists the isotropic differential neutrino flux upper limits from the RESUN experiment along with past lunar-target observations. Note that all upper

Table 5.1: Observation Results from Lunar-Target UHE Neutrino Searches.

Instrument	ν	t	E_{min}	E×I(1 ZeV)	E×I(10 ZeV)	E×I(100 ZeV)
RESUN-B	1.40	200	0.69	13	0.36	7.0×10^{-2}
RESUN-A	1.47	45	1.37	NA	7.7	1.2
nuMoon	0.15	20	12.9	NA	NA	2.0×10^{-2}
GLUE	2.30	113	0.97	3.8×10^{4}	23	4.1
Kalyazin	1.40	31	0.47	5.3×10^{2}	34	7.4
Parkes	1.50	10	0.98	1.7×10^{5}	94	17

Units: ν (GHz), t (hr), E_{min} (ZeV), E×I(E) (km^{-2} yr^{-1} sr^{-1})

limits have been calculated using the analytic effective aperture calculation described in Chap. 4. These may differ from upper limits reported using Monte Carlo calculations, i.e. the GLUE search (Gorham et al., 2004) and nuMoon (Scholten et al., 2009), where the authors report upper limits nearly 10 times lower. This discrepancy is discussed further in Gayley et al. (2009) and James and Protheroe (2009), but the cause of the discrepancy is not fully understood.

Figure 5.8 illustrates the estimated flux upper limits from lunar-target (a) and ice-target (b) observations in relation to expected neutrino fluxes from a variety of proposed isotropic neutrino source models. It is clear that the existing lunar searches have not yet reached sensitivity levels which could detect neutrinos from these models, with only RESUN testing the most optimistic Z-burst mechanisms. While ice-target observations generally have less electric field sensitivity and smaller detection aperture when compared to lunar-target experiments, their proximity to the Ĉerenkov burst is of great advantage and results in much lower flux estimates in similar observing times. Comparable lunar-based limits will be possible using

next-generation radio instruments such as the SKA (Beck, 2005) or lunar orbiters. These instruments have to potential to probe GZK model predictions depending on total observing time and observation frequency (See Chap. 6 for discussion).

5.5 Point Source Flux Upper Limits

Although RESUN did not have adequate sensitivity to test isotropic neutrino source models such as topological defects or the GZK mechanism, the non-detection result can be used to determine upper limits for UHE neutrino point source (e.g. active galaxies) fluxes along the lunar path. Fig.5.9a shows the sky coverage of RESUN over the entire 250 hour experiment along with sky positions of known active galaxies (Veron-Cetty and Veron, 2006). The 90% confidence level upper limits for AGN along the lunar path are expressed in Table 5.2. Also listed is source distance d in Mpc, closest angular separation from the lunar center α in degrees, and total time that the source is within the aperture solid angle t_p in hours. The sky coverage of the ANITA experiment (adapted from Gorham et al. 2009) is shown in Fig. 5.9b. Note that ice target searches only sample UHE neutrino point sources which are located within $\sim$10 degrees of the celestial equator.

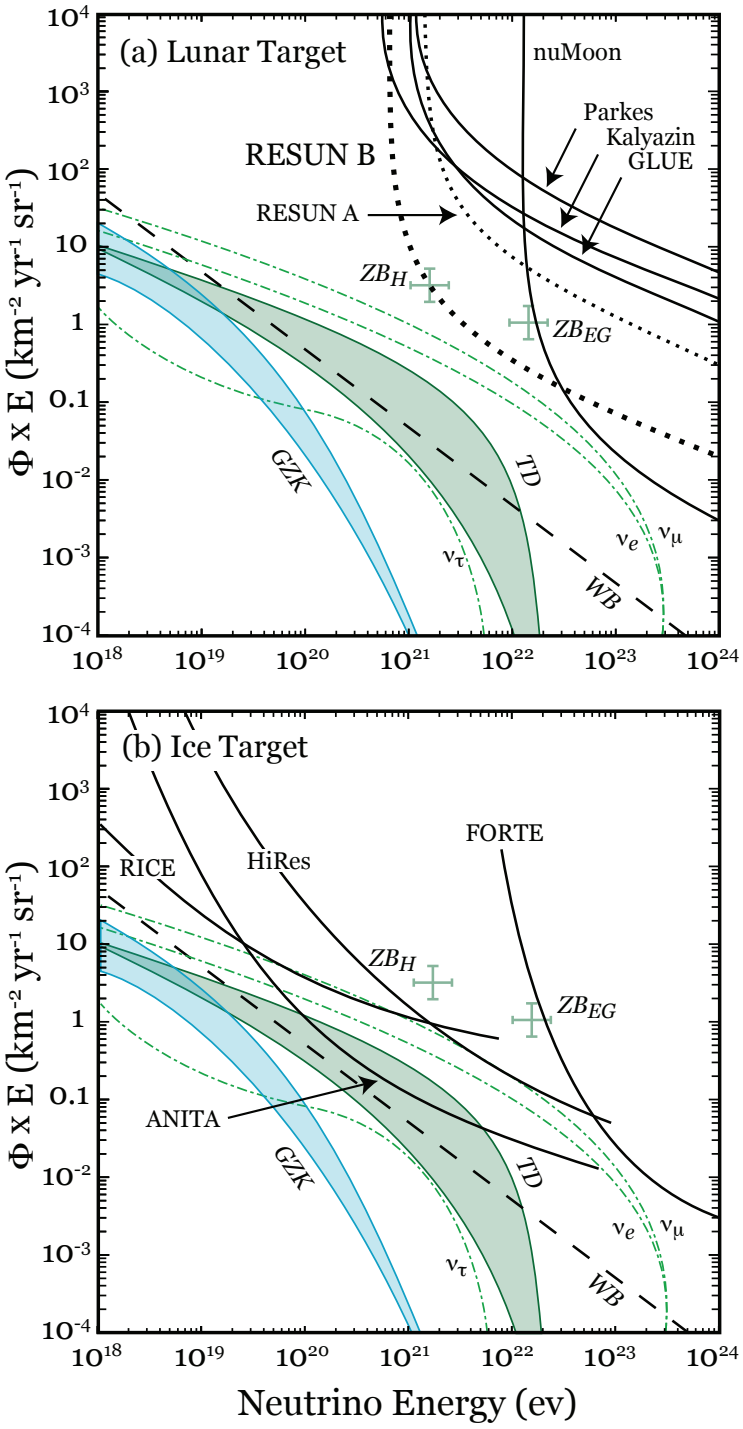

Figure 5.8: UHE Neutrino isotropic flux upper limits determined by lunar neutrino searches.

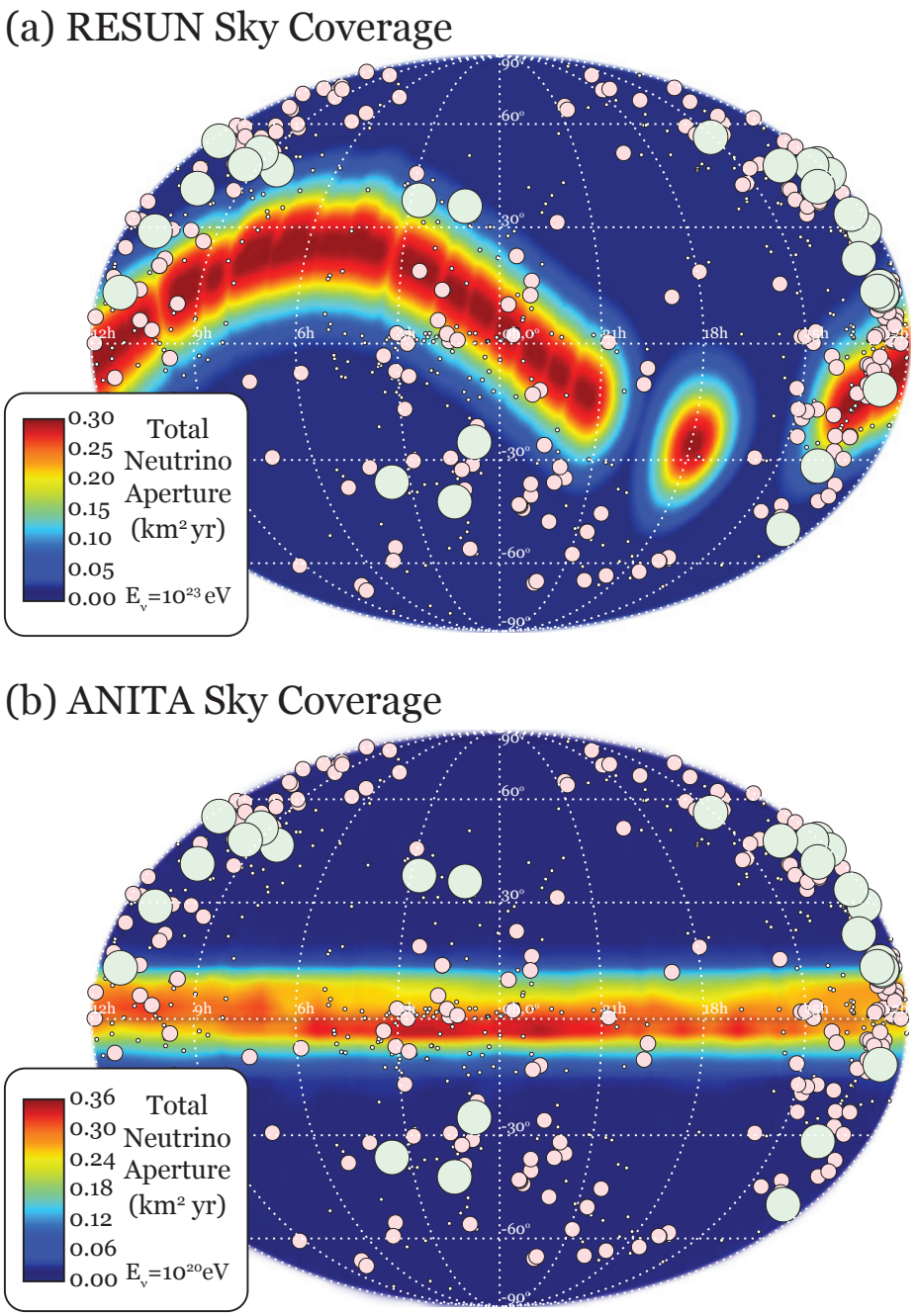

Figure 5.9: Sky Coverage in celestial coordinates of the RESUN (a) and ANITA (b) neutrino detection experiments. Positions of known AGN are shown as filled circles with diameter inversely proportional to distance (large green < 10 Mpc, medium pink 10 Mpc to 25 Mpc, and small black 25 Mpc to 50 Mpc).

Table 5.2: UHE neutrino differential flux upper limits (E dN/dE) established by the 200 hr RESUN observation for sources located more than 10° from the celestial equator (i.e. sources most suitable for lunar-target observations).

Source	d	α	t	E×I(10^{21} eV)	E×I(10^{22} eV)
ESO 508-05	42	10.5	9.8	12	0.32
ESO 509-64	37.9	8.2	9.8	12	0.32
NGC 660	12.7	7.6	8.3	14	0.38
NGC 918	21.1	1.1	16.2	7	0.19
NGC 2911	42	1.9	9.5	12	0.33
NGC 3367	42	8.8	5.9	20	0.53
NGC 3627	8.4	11.9	2.8	42	1.11
NGC 4594	8.4	1.8	24.3	5	0.13
NGC 4700	16.9	2.2	24.8	5	0.13
NGC 4897	33.7	3.7	19.5	6	0.16
NGC 4939	42	4.3	20.1	6	0.15
NGC 4968	37.9	10.2	9.8	12	0.32
NGC 5077	33.7	1.1	14.4	8	0.22
NGC 5597	33.7	11.7	1	118	3.11
NGC 7378	37.9	7.8	14.9	8	0.21
NGC 7450	42	9.8	13.2	9	0.24
NPM1G-10.0425	25.3	2.8	20.5	6	0.15

Units: d (Mpc), α (deg), t (hours), E×I(E) (km^{-2} yr^{-1} sr^{-1})

Table 5.3: UHE neutrino differential flux upper limits (E dN/dE) established by the 200 hr RESUN observation for sources located less than 10° from the celestial equator (i.e. sources most suitable for ice-target observations).

Source	d	α	t	E×I(10^{21} eV)	E×I(10^{22} eV)
MARK 1308	16.9	4	29.8	4	0.1
MARK 1313	33.7	5.9	28.7	4	0.11
NGC 3169	12.7	5.3	5.9	20	0.53
NGC 3660	46.2	7.3	24.1	5	0.13
NGC 3976	33.7	10.1	15.6	8	0.2
NGC 4261	29.5	11.8	6.6	18	0.47
NGC 4303	21.1	10.9	13.6	9	0.23
NGC 4355	29.5	8.2	23.9	5	0.13
NGC 4378	37.9	11.7	9.9	12	0.31
NGC 4385	29.5	7.8	24.7	5	0.13
NGC 4412	33.7	10.9	13.2	9	0.24
NGC 4593	37.9	3.9	19.8	6	0.16
NGC 4628	42	2.7	22.6	5	0.14
NGC 4636	12.7	11.5	12.3	10	0.25
NGC 4691	16.9	6.6	18.4	6	0.17
NGC 4772	12.7	12.1	4.3	27	0.72
NGC 4813	21.1	4.7	22.3	5	0.14
NGC 4845	16.9	12.1	5.2	23	0.6
NGC 4941	12.7	6.9	19.3	6	0.16
NGC 4990	42	8.1	19.1	6	0.16
NGC 5427	37.9	11.6	3.4	35	0.92
NGC 7714	37.9	1.7	16.1	7	0.19
NGC 7743	29.5	6.2	7.4	16	0.42

CHAPTER 6
BEYOND RESUN: ANTICIPATED FUTURE NEUTRINO DETECTION EXPERIMENTS

The aperture model described in Chapter 4 was instrumental in determining the optimal observing parameters for the RESUN detection experiment. This chapter discusses how the aperture scaling laws can be applied to the planning of future lunar-target Ĉerenkov burst detection experiments and is used to make isotropic neutrino flux upper limit predictions for example experiments using the EVLA, SKA, and low altitude lunar orbiters.

6.1 Testing UHE Neutrino Production

The expected number of UHE neutrino detections from isotropic sources in exposure time t is the integral of the neutrino flux $I(E)$ times the effective aperture $A_e(E)$ over the all detectable energies (cf. Sec. 4.3). The anticipated observation time required to detect one event is then

$$t \;=\; 1 \;/\; \int_{E_{min}}^{\infty} dE\; I(E)\; A_e(E).$$

Integrated over energy, the aperture varies with observation frequency, minimum detector sensitivity, and (while not made explicit in the RESUN specific expressions) the distance to the source. Decreasing the distance to the Ĉerenkov cone **increases** the detection probability (cf. Eqn. 4.2) by increasing the the ratio of the cone thickness at threshold $\mathcal{E}_{min}$ to the $1/e$ width (f_o).

Using isotropic models for cosmogenic neutrino production (Engel et al., 2001) and neutrinos created by topological defects (James and Protheroe, 2009, and refs.), the required one-count observation time versus minimum detector sensitivity $\mathcal{E}_{min}$ is plotted in Figure 6.1 for earth-based and lunar-based experiments. In general, close proximity to the source ($\sim$ 100 km) accounts for a factor of a thousand decrease in the required detector sensitivity needed to observe the same number of counts at

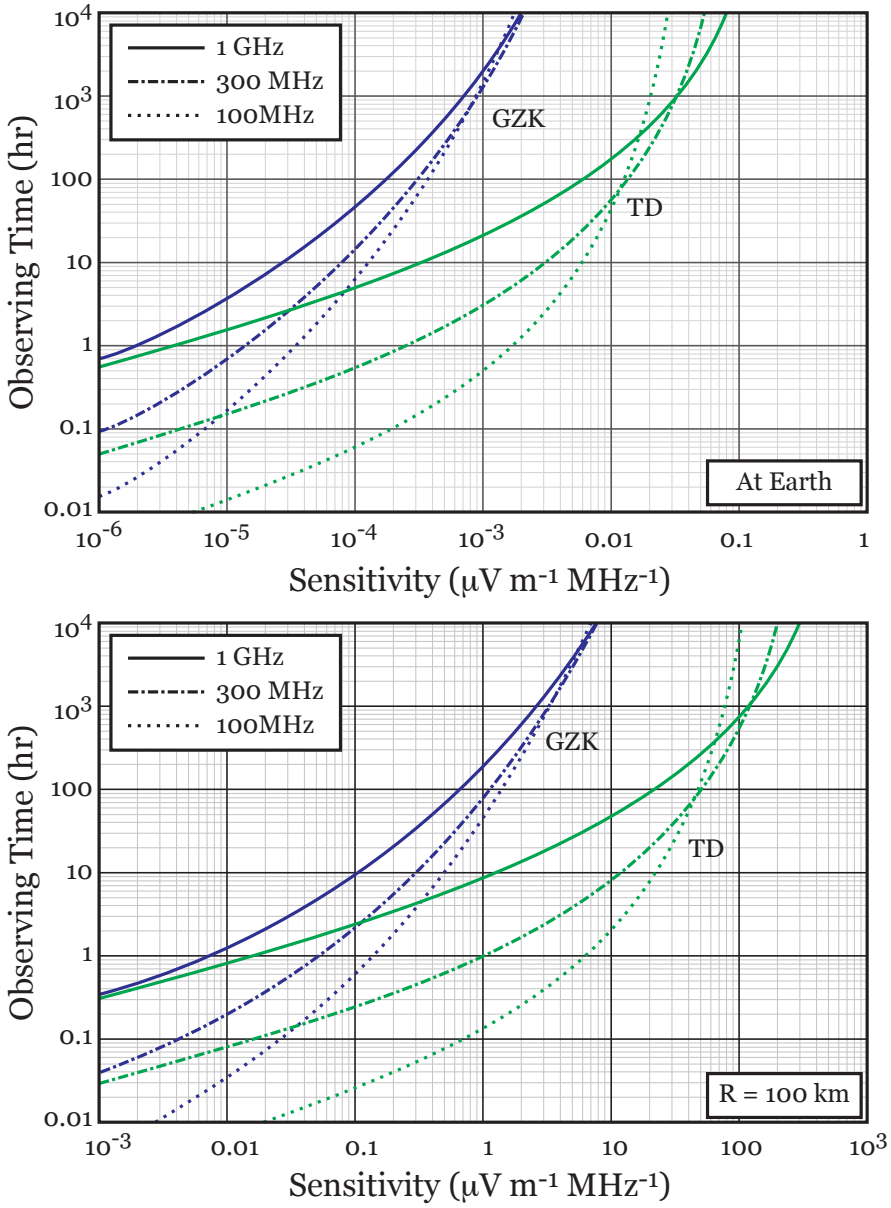

Figure 6.1: Anticipated observation time need to detect UHE neutrinos from GZK (Engel et al., 2001) and topological defect (TD, James and Protheroe 2009 and refs.) production models when observing from the Earth (top) and from a 100 km above the lunar surface (bottom). Observation time estimates are plotted for observing frequencies of 1 GHz (solid lines), 300 MHz (dot-dashed lines), and 100 MHz (dotted lines).

earth-moon distance. It is for this reason that terrestrial ice-target searches such as ANITA have established the most restrictive flux upper limits, despite probing

smaller areas and utilizing less sensitive radio receivers than comparable lunar-target experiments.

6.2 Future Lunar-Target Observations

With in the increased sensitivity of the EVLA and the anticipated sensitivity of the SKA, these instruments may be positioned to make the first detections of UHE neutrinos. In addition, proposed lunar orbiters such as LADEE (Hine, 2009) or GRAIL (Zuber et al., 2008) may also be well suited to detect neutrino-induced Ĉerenkov burst emission from the moon. The analytic aperture formulation developed for the RESUN experiment is a valuable tool for highlighting trade-offs between choices in observation frequency, target energy, and detection threshold. It is applied below to highlight these trade-offs and estimate the detection probability for a variety of experiments utilizing the EVLA, SKA, and low-orbit lunar orbiters.

For reference, the expected instrument parameters can be found in Table 6.1 and the anticipated results can be found in Table 6.2.

6.2.1 EVLA

While the RESUN experiment used EVLA antennas, the data acquisition system utilized the VLA analog back-ends to sample antenna voltages. In January 2010, these analog back-ends were disconnected and the EVLA receiver system now utilizes a completely digital signal path. The all digital system provides advantages for pulse detection experiments, namely significantly wider frequency bandwidths ($\sim$ 800 MHz for $\nu > 1$ GHz) and simultaneous access to data from all 27 antennas. The result is a factor of four improved electric field sensitivity (see Eqn. 3.2) when compared with the RESUN setup at 1.4 GHz. In addition to the current improvements, the deployment of two low frequency (350 MHz, 74 MHz) receivers is planned in early 2012 (Ott, 2010)) which could provide an EVLA based experiment

Table 6.1: Observing Parameters for Future Lunar-Target Ĉerenkov Pulse Detection Experiments.

Instrument	ν	$\Delta\nu$	$\mathcal{E}_{RMS}$	n_σ
EVLA	1500	800	0.002	3.1
EVLA	350	50	0.013	2.4
SKA	1500	500	2.8×10^{-4}	3.8
SKA	100	50	0.002	3.3
Orbiter	1400	200	0.580	8.4
Orbiter	1400	200	0.580	3.3
Orbiter	100	25	0.220	8.4
Orbiter	100	25	0.220	3.3

Units: ν (MHz), $\Delta\nu$ (MHz), $\mathcal{E}_{RMS}$ (μV m^{-1} MHz^{-1})

much larger lunar detection apertures.

The anticipated UHE neutrino flux limit obtained from a wide-band 1.5 GHz, and a narrow-band 350 MHz Ĉerenkov pulse detection experiment are calculated and the results are displayed in Table 6.2. Each experiment assumed 10 ns sampling and delay windows appropriate for the size of the primary antenna beam (10 samples at 1.5 GHz and 20 samples at 350 MHz). The decrease in detection threshold n_σ is obtained by using three sub-arrays of 8 antennas and a single array of 27 coincident antennas for the respective experiments. As EVLA time is typically in high demand, a "practical" observation time of 200 hr was chosen.

Low-frequency estimates were made at 350 MHz as opposed to 75 MHz because of the contribution to the system temperature (a proxy for $\mathcal{E}_{RMS}$) made by Galactic radio emission. At low frequencies, the brightness temperature associated with

diffuse Galactic ratio emission is (Lawson et al., 1987)

$$T_{Gal} \;=\; 50\ K\ \left[\frac{150\ MHz}{\nu}\right]^{2.75} \tag{6.1}$$

where ν is the observing frequency. At 350 MHz, the Galactic contribution to the system temperature is negligible. However, at 75 MHz the radio brightness is nearly 1.5 times that of the moon with $T_{Gal} \sim 350$ K.

Despite the EVLA sensitivity enhancements, the minimum detectable neutrino energy is too high to observer cosmogenic neutrinos (see Fig. 6.1). However, a 200 hr search at 1.5 GHz does establish a new isotropic flux upper limit for neutrino energies greater than $10^{22.3}$ eV.

6.2.2 SKA

The SKA is a proposed interferometric array with 1 million square meters of collecting area, 3000 km maximum baselines, and observing frequencies between 65 MHz and 35 GHz. Conventional large diameter antennas like those used at the EVLA will be replaced by $>$ 100 small and inexpensive antennas which observe in phase to synthesizing antennas with collecting areas comparable to 200 m telescopes. The complete SKA will contain 30 of theses large aperture stations plus an additional 150 stations each with collecting collecting area equivalent to a 90 m telescope.

The anticipated neutrino flux upper limit obtained from a wide-band 1.5 GHz, and a narrow-band 100 MHz pulse detection experiment was calculated using the Gayley aperture model and the results are displayed in Table 6.2. Each experiment assumed 200 m synthesized antennas, 10 ns sampling, and delay windows appropriate for the both the size of the primary antenna beam and the large station separation (150 samples at 1.5 GHz and 300 samples at 100 MHz). The detection threshold for each observation was predicted assuming 10 coincident stations per

Table 6.2: Anticipated Flux Upper Limits from Future Lunar-Target UHE Neutrino Searches.

Instrument	ν	t	E_{min}	E×I(0.1 ZeV)	E×I(1 ZeV)	E×I(10 ZeV)
EVLA	1500	200	0.26	NA	1.4	0.20
EVLA	350	200	3.70	NA	NA	8.7×10^{-4}
SKA	1500	200	0.05	NA	1.0	0.15
SKA	100	200	2.10	NA	NA	1.0×10^{-2}
Orbiter	1400	1 yr	0.19	0.05	1.1×10^{-2}	2.6×10^{-3}
Orbiter	1400	1 yr	0.02	2.7×10^{-2}	5.6×10^{-3}	1.7×10^{-3}
Orbiter	100	1 yr	0.18	NA	5.6×10^{-2}	6.0×10^{-6}
Orbiter	100	1 yr	0.04	2.5×10^{-4}	1.6×10^{-5}	3.1×10^{-6}

Units: ν (GHz), t (hr), E_{min} (ZeV), E×I(E) (km^{-2} yr^{-1} sr^{-1})

sub-array for the 1.5 GHz observations and 30 coincident antennas for the 100 MHz observation. While the 1.5 GHz observation would require $\sim$ 2000 observing hours to probe GZK models (ref. Fig. 6.1), the results given are for 200 observing hours to account for high instrument demand and provide comparison with the EVLA analysis.

The minimum electric field sensitivity given by Equation 3.2 predicts that element measurements improve linearly with increased antenna diameter. For this reason, it is only expected that the SKA will of order 200 m / 25 m = 8 times more sensitive than comparable EVLA experiments at the same frequency. The increase in electric field sensitivity and corresponding increase in neutrino low energy sensitivity for the 1.5 GHz experiment is still not enough to detect cosmogenic neutrinos (see Fig. 6.1) for observations shorter than 200 hours, but the SKA is

poised to make the first probes of GZK models if $\sim$ 2000 hours are possible. The sensitivity enhancement and the large detection aperture at 100 MHz is however sufficient to probe topological defect neutrino production models in as little as 1 hour and establish a new isotropic flux upper limit for neutrino energies greater than $10^{21.5}$ eV.

6.2.3 Lunar Orbiters

Lunar orbiters present an excellent opportunity to make the first detection of UHE neutrinos. The close proximity to the pulse source means a significant increase to both the detection aperture (by increasing f_o, see Eqn 4.2) and the minimum neutrino energy sensitivity. Orbiters also have potential for observations times on order the satellite flight time, as pulse detection experiments are not CPU intensive and can be designed to run as background processes.

The expected isotropic flux upper limit for one calendar year pulse detection experiments operating at 1.4 GHz and 100 MHz is predicted, with results displayed in Table 6.2. Each experiment assumes the use of full-wavelength whip antennas (21 cm at 1.4 GHz and 3 m at 100 MHz), altitude of 100 km, and a sample time of 10 ns. Flux limits are also estimated for both single antenna detectors and detectors employing eight individual antennas. The pulse threshold for a single element detector with 10 ns sampling must be set to $n_\sigma > 8$ for accidental events to be unlikely in one calendar year, while the threshold level can be halved for the same 1 yr observation if 8-elements are used.

Analysis of the lunar orbiter experiments described above shows that, while the minimum electric field sensitivity $\mathcal{E}_{min} = n_\sigma \times \mathcal{E}_{RMS}$ significantly exceeds that of the EVLA or SKA, the decreased distance to the Ĉerenkov source allows orbiters to probe topological defect models in under 24 hours and cosmogenic production in under 4 months. A multi-element lunar orbiter observing at 100 MHz (experiment

with smallest $\mathcal{E}_{min}$) will probe the Engel et al. (2001) GZK neutrinos production models in just 20 hours.

6.3 Predicted Isotropic Flux Limits

Estimated isotropic neutrino flux upper limits for proposed EVLA, SKA, and lunar orbiter experiments are shown in Figure 6.2. Shaded regions indicate the current isotropic flux upper limit (brown), anticipated isotropic neutrino flux from topological defects (green, James and Protheroe 2009 and refs.), and the anticipated isotropic neutrino flux due to GZK cosmic ray scatter (blue, (Engel et al., 2001)). Note that only the proposed lunar orbiter observations are able to probe cosmogenic neutrino models.

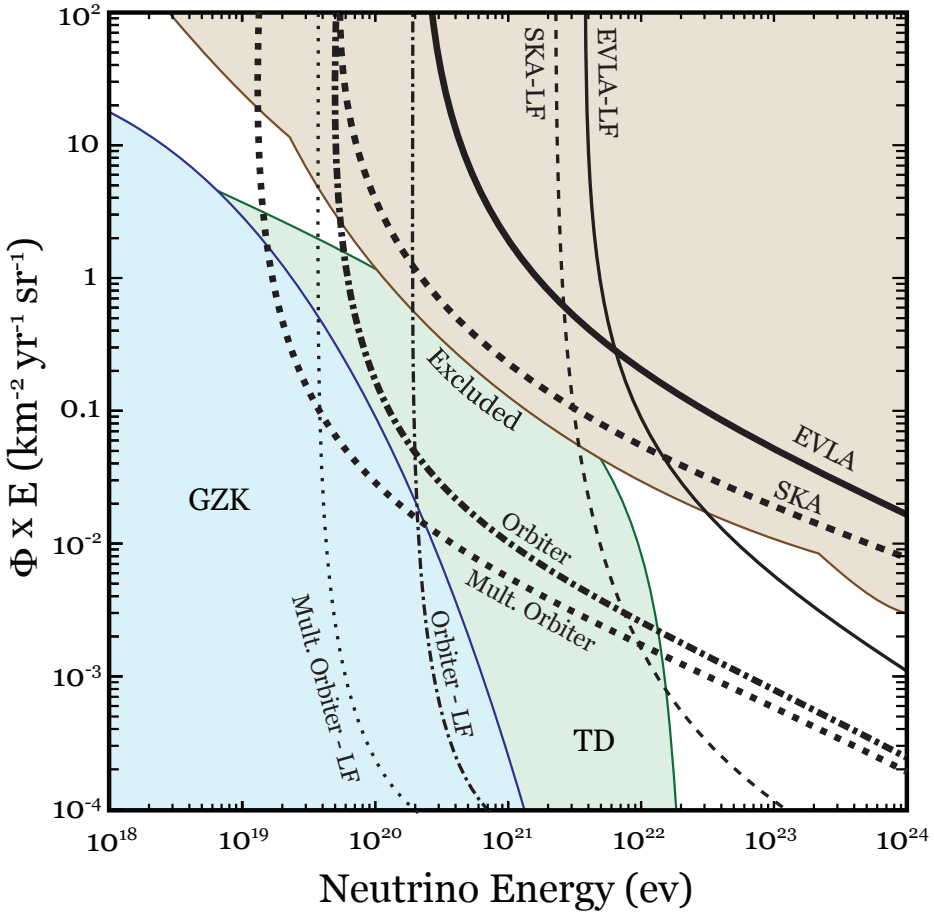

Figure 6.2: UHE neutrino flux upper limits obtainable by future lunar-target observations. Shown are limits obtained by using the EVLA (solid lines), SKA (dashed lines), a single antenna orbiter (dot-dashed line) and a multiple antenna orbiter (dotted lines). In all cases, thick lines indicate observations made above 1 GHz, while thin lines mark those made below 1 GHz.

APPENDIX A

TRIGGER LOGIC AND FPGA DESIGN

A.1 FPGA Design

At the core of the RESUN data acquisition system (RDAQ) is a Field Programmable Gate Array (FPGA) device which contains the logic-trigger design. Analog to digital converters (ADCs) and onboard memory are accessed by the FPGA using design blocks developed at the UC-Berkeley CASPER Lab. This tool-flow can be downloaded from http://casper.berkeley.edu/wiki/Toolflow. The FPGA functions are implemented using Simulink, an embedded systems design plug-in for Matlab. Figures A.1 through A.4 display the FPGA Simulink desing employed for the RESUN search. The signal thresholding is performed in Block-C and the simple trigger is performed in Block-D. Unless otherwise indicated, FPGA programming block which interface with CASPER hardware are colored yellow, RESUN logic-trigger blocks are colored green, and Xilinx FPGA core command are blue.

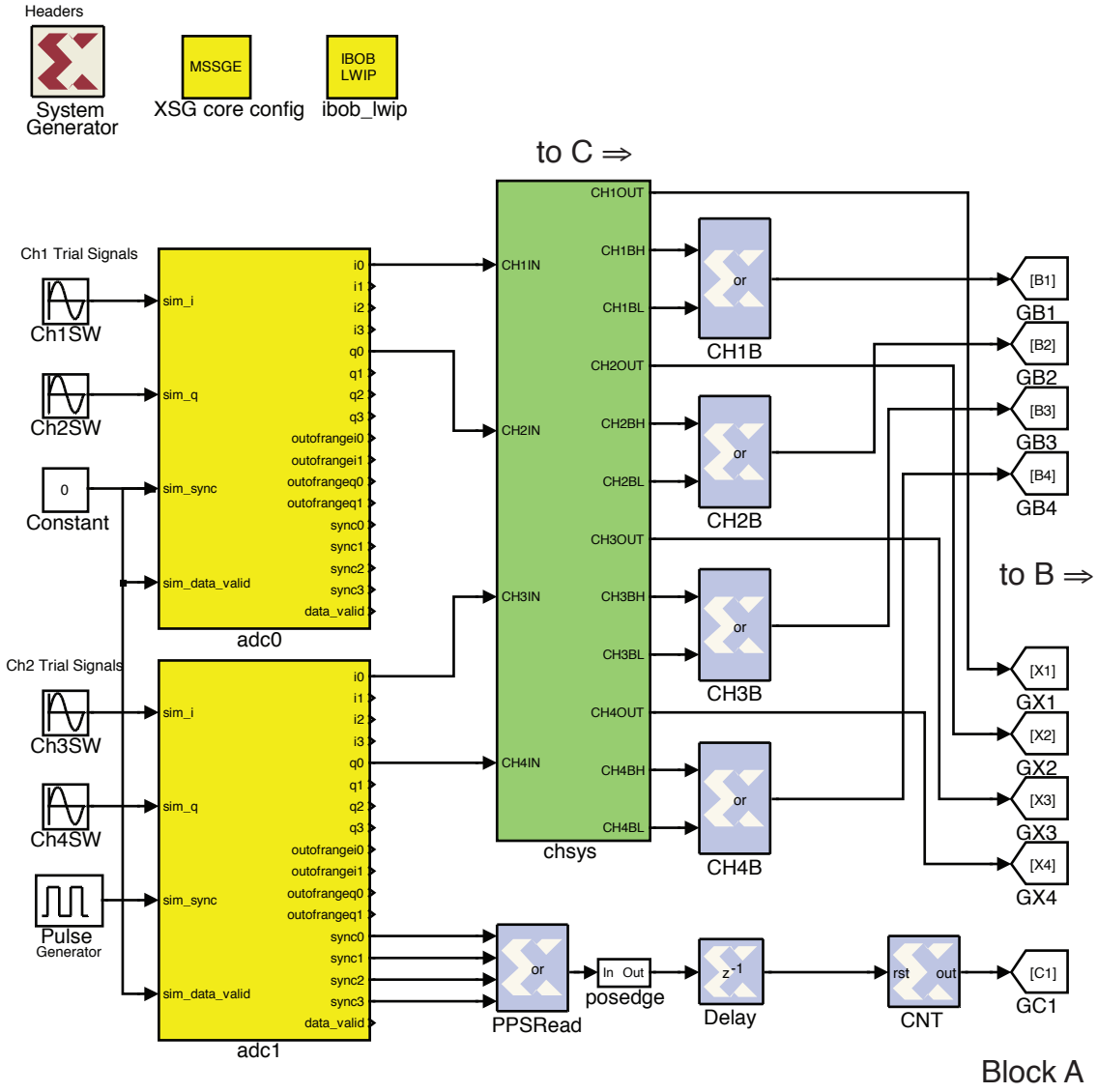

Figure A.1: RESUN FPGA design - Block A. Antenna signals are sampled using the two high speed ADCs (yellow blocks) and their output is feed into the "chsys" block (see Fig. A.3 which is responsible for thresholding the data streams. Positive and negative voltage pulses are assumed equally likely. The absolute position of each trigger is marked with a sample number generated by a ADC clock counter (CNT). Sample numbers are reset each second by a PPS generator attached to the second ADC (adc1).

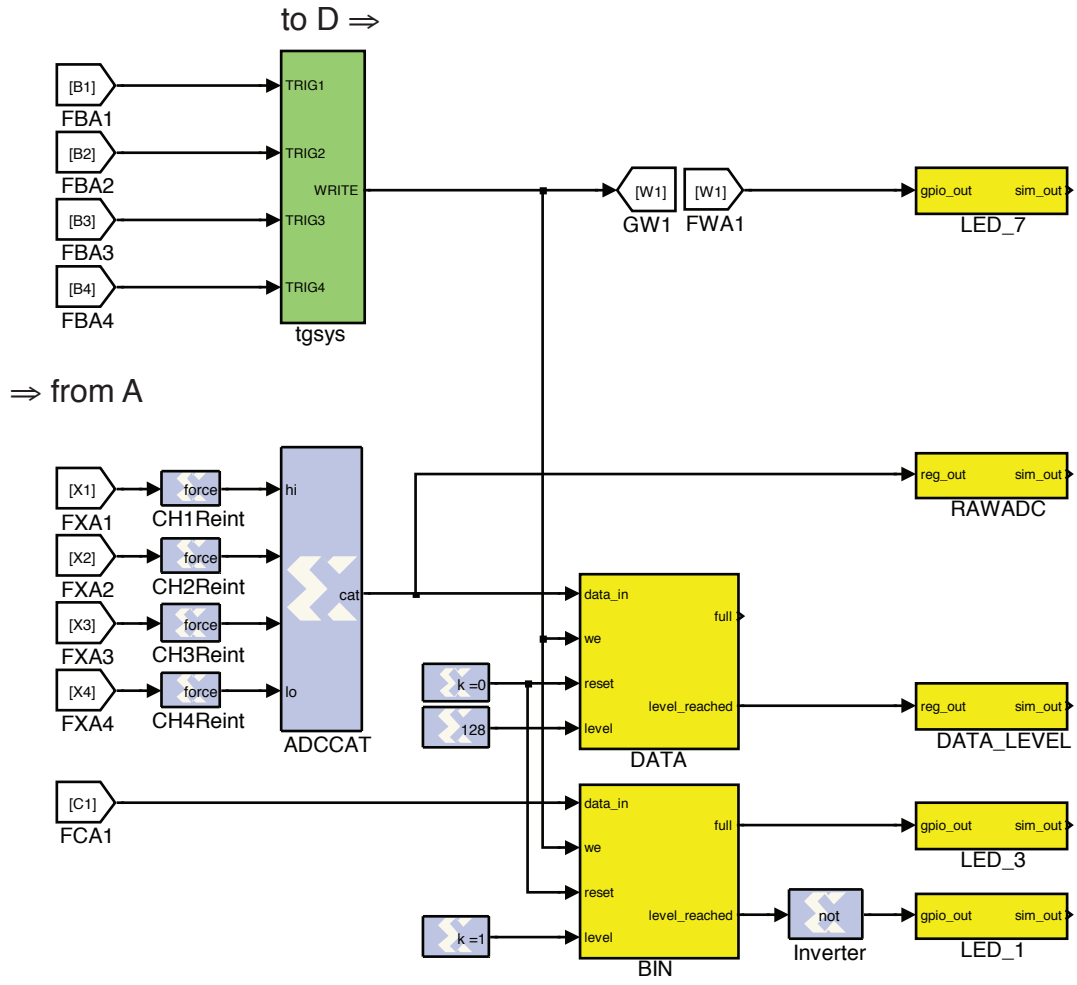

Figure A.2: RESUN FPGA design - Block B. If a voltage sample exceeds the set positive or negative threshold on any channel (determined in the green "tgsys" block, see Fig. A.4), the sample from each antenna is packaged (along with the corresponding sample counter) and placed in an onboard memory FIFO (first-in, first-out). When sufficiently full, the FIFO contents are transmitted by the iBOB using the commands given in Sec. A.2.

A.2 iBOB Processor Code

The FPGA design is compiled with custom iBOB CPU commands designed to read the onboard FIFO and transmit data packages via UDP packets over ethernet

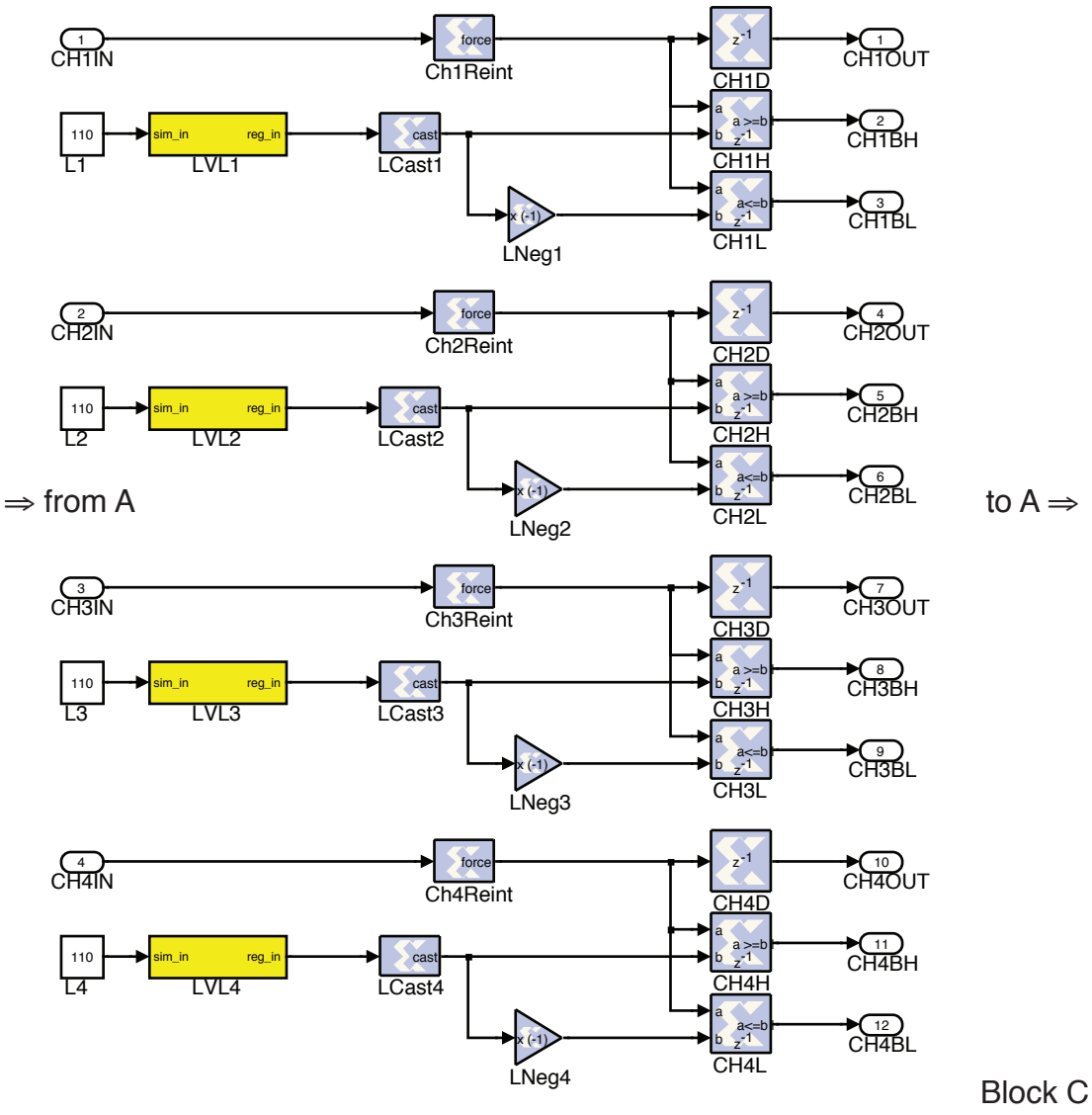

Figure A.3: RESUN FPGA design - Sub-Block C. Threshold levels are set via yellow CASPER blocks. Positive and negative voltage spikes are considered equally probable, so the threshold level is applied to the absolute value of the input signal.

cable. Excerpts from this code are given below. To implement the changes, (1) Change directory to model_directory/XPS_iBOB_base, (2) At the command prompt, type $xps -nw system.xmp, and (3) type $run init_bram.

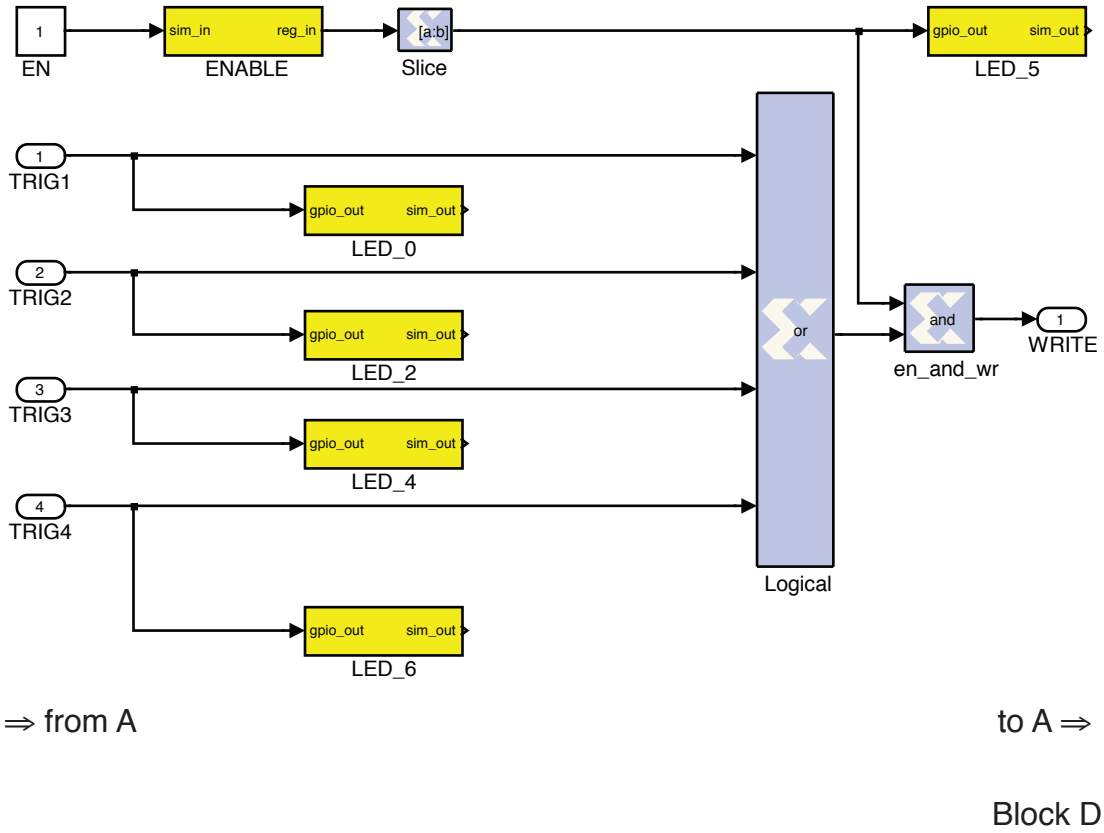

Figure A.4: RESUN FPGA design - Sub-Block D. A simple logic-trigger is applied which monitors the data stream for threshold event in any channel. Any future RESUN experiments will implement a more sophisticated algorithm which searches for common threshold events inside a sample window. Trigger occurrence is visually indicated on the RDAQ using various LEDs.

A.2.1 Script: main.c

The following lines are added to the default main.c script.

```
// Prototypes
static void startudp_cmd(int, char**);
static void endudp_cmd(int, char**);
```

```
void send_packet_if_ready(void);

// Commands
/*
static tinysh_cmd_t cmd_19 =
{0,"startudp","Starts the UDP Server","",startudp_cmd,0,0,0};
static tinysh_cmd_t cmd_20 =
{0,"endudp","Ends the UDP Server","",endudp_cmd,0,0,0};
*/

static tinysh_cmd_t cmd_19 =
{0,"startudp","","",startudp_cmd,0,0,0};
static tinysh_cmd_t cmd_20 =
{0,"endudp","","",endudp_cmd,0,0,0};

// UDP Server Setup
struct udp_pcb *udppcb;
struct ip_addr addr;
struct pbuf *somebuf;
//int i=0, j=0, k=0;
//int numpackets;
//int waittime;
int packetstatus;
Xuint32 dirxvalue, accnum, loadindicator
Xuinit32 bin_value, data_value, fail;
char bootpacket[1500];
int udpswitch = 0;
Xuint32 dumpbram;

// Functions
static void startudp_cmd(int argc, char **argv)
{
  // Usage: startudp 169 254 128 10 6969

  // The UDP server will transmit a 1kb (1024 bit)
  //payload + a 21 bit packet header
  // 21 byte UDP data packet headers look like this:
  // 8 bytes (double) time
  // 1 byte x engine number
  // 4 bytes (unsigned int) vector number within
  // an integration (ie if you want to send 10MB
  // every integration and you break it up into 1MB packets,
  // this number will range from 0 to 9)
  // 4 bytes (unsigned int) flags
  // 4 bytes (unsigned int) data length (in bytes)

  int udpport=0;
```

```
  //Error Test
  if(argc!=6) {
    xil_printf("Wrong number of arguments\n\r");
    return;
  }

  // Start the server
  udpport = tinysh_atoxi(argv[5]);
  xil_printf("Instantiating UDP Server...\r\n");
  xil_printf("Will transmit to IP Address:
    %d.%d.%d.%d on port: %d\r\n", tinysh_atoxi(argv[1]),
    tinysh_atoxi(argv[2]),tinysh_atoxi(argv[3]),
    tinysh_atoxi(argv[4]), udpport);
  IP4_ADDR(&addr, tinysh_atoxi(argv[1]),
  tinysh_atoxi(argv[2]),tinysh_atoxi(argv[3]),
    tinysh_atoxi(argv[4]));
  udppcb = udp_new();
  somebuf = pbuf_alloc(PBUF_TRANSPORT,
    1045, PBUF_ROM);
  //udppcb->flags &= ~(UDP_FLAGS_UDPLITE);
  udp_connect(udppcb, &addr, udpport);
  xil_printf("UDP pcb instantiated\n\r");

  //prepare the header
  bootpacket[0] = 0x0;
  bootpacket[1] = 0x0;
  bootpacket[2] = 0x0;
  bootpacket[3] = 0x0;
  bootpacket[9] = 0x0;
  bootpacket[10] = 0x0;
  bootpacket[11] = 0x0;
  bootpacket[13] = 0x0;
  bootpacket[14] = 0x0;
  bootpacket[15] = 0x0;
  bootpacket[16] = 0x0;
  bootpacket[17] = 0x0;
  bootpacket[18] = 0x0;
  bootpacket[19] = 0x0;
  bootpacket[20] = 0x0;

  (*somebuf).payload = bootpacket;
  loadindicator = 9999;
  // indicate that the UDP Server has started
  udpswitch = 1;
}

static void endudp_cmd(int argc, char **argv)
{
```

```
  //xil_printf("Removing UDP pcb...");
  udp_remove(udppcb);
  pbuf_free(somebuf);
  //xil_printf("Done\n\r");
  udpswitch = 0;
}

void send_packet_if_ready(void)
{
  int i;
  accnum = 0;
  loadindicator++;
  //test if the data is ready based on a register value
  accnum = sif_reg_read(
    XPAR_RESUN_V1_3_DATA_LEVEL_BASEADDR);
  if (accnum == 1) {
    //add info to packet header
    bootpacket[4] = (accnum >> 0);
    bootpacket[5] = (accnum >> 8);
    bootpacket[6] = (accnum >> 16);
    bootpacket[7] = (accnum >> 24);
    bootpacket[12] = (Xuint8) 0;

    dirxvalue = XIo_In32(dumpbram + 32764);
    memcpy(bootpacket + 21, &dirxvalue, 4);

    for(i=0;i<128;i++){
      //read the FIFO values
      bin_value = sif_fifo_read_nonblock(
        XPAR_RESUN_V1_3_BIN_BASEADDR, &fail);
      data_value = sif_fifo_read_nonblock(
        XPAR_RESUN_V1_3_DATA_BASEADDR, &fail);
      //copy the values to the bootpacket
      memcpy(bootpacket+(i*8)+21, &bin_value, 4);
      memcpy(bootpacket+(i*8)+21+4, &data_value, 4);
    }

    memcpy(bootpacket + 13, &loadindicator, 4);
    somebuf->len = (u16_t) 1045;
    somebuf->tot_len = (u16_t) 1045;
    udp_send(udppcb, somebuf);
    loadindicator = 0; //reset load cntr
  }

  //return accnum;
}

// Main Thread
```

```
int main(void)
{

. . .

/* loop waiting for input */
while(1) {
#ifndef LINUX_ENABLE
    process_inputs(1);
    if(udpswitch == 1){
      send_packet_if_ready();
    }
#else // LINUX_ENABLED is defined
    tinysh_char_in(inbyte());
#endif // LINUX_ENABLE
  }

}
```

A.3 RDAQ Interface Scripts

The RESUN data acquisition system (RDAQ) is configured using a series of scripts written in python. These scripts are responsible for configuring the RDAQ with the threshold parameters, enabling/disabling RDAQ sampling, and enabling/disabling data capture on the host computer. Each script is accessed by calling a master library file named **iBOB.py** which is given below. After setup, candidate events sampled by the RDAQ are formatted by the onboard processor and automatically transmitted as internet protocol (UDP) packets. To capture the data packets, the host computer uses a "packet sniffer" called **tcpdump** which monitors the activity on a designated internet port and saves any incoming packets to a file.

An outline of the capture process is as follows:

1. Start Python and import the **iBOB.py** library

2. Configure the RDAQ with the command **iBOB.Startup()**

3. Take a data snapshot using **iBOB.snapshot()**

4. Set the threshold levels based on the data sample by calling **iBOB.SetLVLs()**

5. Configure the data transfer port and enable sampling using **iBOB.StartUDP()**, **iBOB.Enable()**

6. Start the capture process on the host computer with **iBOB.Capture()**

A.3.1 Script: start_capture

```
import time
import os
import sys
import iBOB
import numpy

# read the capture time from the argument
if len(sys.argv) == 1 :
    sys.argv.append(480)

captime = 60 * long(sys.argv[1])

# Globals
savroot = "/media/DataEXT/Data/PhaseB/"
b1 = "169.254.128.1"
b2 = "169.254.128.2"
b3 = "169.254.128.3"

# Configure the iBOB (if not manually setup)
#iBOB.Logout(iBOB.Startup(b1, lvl=[40,40,40,40]))
#iBOB.Logout(iBOB.Startup(b2, lvl=[40,40,40,40]))
#iBOB.Logout(iBOB.Startup(b3, lvl=[40,40,40,40]))

# Load the current time
tnow = time.localtime()
print "The current time is: " +
    time.strftime("%H:%M:%S UT on %d/%b/%Y",tnow)

# Build the storage dir based on the time
daystr = time.strftime("%d%b%Y",time.localtime())
savdir = savroot + daystr + "/"
if not os.path.exists(savdir):
    os.mkdir(savdir)
```

```
os.chdir(savdir)

# e-mail status update
os.system("echo '" + str(captime/60) +
    " min Capture Started' | mail -s 'RESUN STATUS UPDATE " +
    daystr + " 'ted.jaeger@gmail.com")

# Take a quick look at the data
print "Taking a Snapshot to determine levels"
sname = iBOB.Snapshot([b1,b2,b3])

# Calculate the 4sigma Levels
lvl = iBOB.Stats(sname)

# Set the levels based on the data (optional)
#print "Setting iBOB Levels to:"
#iBOB.SetLVLs([iBOB.Login(b1),iBOB.Login(b2),iBOB.Login(b3)],lvl)
#print lvl

# Start Recording
iBOB.Capture([b1,b2,b3],lvl,captime)
```

A.3.2 Script: iBOB.py

```
# iBOB.py
# Python functions to interface with the iBOB boards
# Created 09/11/09 by Ted Jaeger

def FindSigma(x):
    from numpy import abs, array, std
    x = array(x)
    #print x
    y = []
    for i in range(len(x)):
        if abs(x[i]) > 2 and abs(x[i]) < 25:
            y.append(x[i])
    return std(y)

def Twos(x):
    return (2**8-1)*(x>=2**7)-x

def ReadPCAP(infile):
    from struct import unpack

    f = open(infile, 'rb')
    print "Reading data from " + infile
```

```
# unpack the file and search for UDP packets

# 24 byte PCAP header (one per file)
pcap_head = f.read(24)
# parse the pcap_header (TODO)
# the file header consists of, in order:
# 4 byte "magic number";
# 2 byte major version number;
# 2 byte minor version number;
# 4 byte "time zone offset" (not used)
# 4 byte "time stamp accuracy" (not used)
# 4 byte "snapshot length" field;
# 4 byte "link layer type" field.

# loop through the packets, saving data in lists
tme = []
src = []
mrk = []
ch1 = []
ch2 = []
ch3 = []
ch4 = []

# 16 byte PPC tag header
ppc_head = f.read(16)

while ppc_head != '' :

    # parse the ppc header
    time_sec = unpack('i',ppc_head[0:4])[0]
    time_msec = unpack('i',ppc_head[4:8])[0]
    jd1970 = 2440587.5
    time = jd1970 + (time_sec + time_msec/1E6)/8.64E4

    # intended_packet_size = unpack('i',ppc_head[8:12])
    packet_size = unpack('i',ppc_head[12:16])[0]
    #print packet_size
    # if packet_size = 1087, the packet is from the iBOB

    udp_packet_count = 0L
    if packet_size == 1087 :
        # save the time
        tme.append(time)

        # read the UDP packet
        udp_packet_count = udp_packet_count + 1L

        # 42 byte UDP header
```

```
            # byte order reversed
            udp_head = f.read(42)
            # parse the udp header
            # eth_head = udp_head[0:14]
            ip_head = udp_head[14:34]
            # ip_junk = ip_head[0:12]
            ip_src = unpack('BBBB',ip_head[12:16])
            src.append(ip_src[3])
            # print src
            ip_des = unpack('BBBB',ip_head[16:20])
            # tx_head = udp_head[34:42]
            # tx_src = unpack('H',tx_head[1]+tx_head[0])[0]
            # tx_des = unpack('H',tx_head[3]+tx_head[2])[0]
            # tx_len = unpack('H',tx_head[5]+tx_head[4])[0]
            # tx_chk = unpack('H',tx_head[7]+tx_head[6])[0]

            # 1045 byte data packet
            data = f.read(1045)
            # data_head = data[0:21]
            data_pack = data[21:1045]
            for i in range(128) :
                cnt = unpack('L',data_pack[8*i+3]+
                             data_pack[8*i+2]+
                             data_pack[8*i+1]+data_pack[8*i])[0]
                adc_i0 = Twos(unpack('B',data_pack[8*i+4])[0])
                adc_q0 = Twos(unpack('B',data_pack[8*i+5])[0])
                adc_i1 = Twos(unpack('B',data_pack[8*i+6])[0])
                adc_q1 = Twos(unpack('B',data_pack[8*i+7])[0])
                # print cnt,adc_i0,adc_q0,adc_i1,adc_q1
                mrk.append(cnt)
                ch1.append(adc_i0)
                ch2.append(adc_q0)
                ch3.append(adc_i1)
                ch4.append(adc_q1)

        else :
            # read the non-UDP packet and move on
            non_upd_packet = f.read(packet_size)

        # read the next packet
        ppc_head = f.read(16)

    print "DONE!"
    return (tme, src, mrk, ch1, ch2, ch3, ch4)

def SetLVL(sock,ch=1,lvl=100):
    sock.send("regwrite chsys/LVL"+str(ch)+" "+
    str(int(lvl))+"\n")
```

```
def SetLVLs(sock,lvl=[100,100,100,100]):
    #from time import sleep
    for i in range(4):
        SetLVL(sock,i+1,lvl[i])
        #sleep(1)

def Enable(sock):
    print "Enabling iBOB"
    sock.send("regwrite tgsys/ENABLE 1\n")

def Disable(sock):
    sock.send("regwrite tgsys/ENABLE 0\n")

def StartUDP(sock, destination = "169 254 128 101 6969"):
    print "Starting UDP Server"
    sock.send("startudp 169 254 128 101 6969\n")

def EndUDP(sock):
    #from time import sleep
    Disable(sock)
    #sleep(1)
    sock.send("endudp\n")

def ResetAll(sock):
    from time import sleep
    Disable(sock)
    EndUDP(sock)
    sock.send("adcreset adc0\n")
    sock.send("adcreset adc1\n")
    sock.send("fiforeset DATA\n")
    sock.send("fiforeset BIN\n")
    sleep(1)

def Login(host = '169.254.128.1'):
    import socket
    print "Logging in to " + host
    s = socket.socket(socket.AF_INET, socket.SOCK_STREAM)
    s.connect((host,23))
    return s

def Logout(s):
    print "Logging Out"
    s.shutdown(2)

def Startup(host = '169.254.128.1', lvl = [100,100,100,100]):
    #import socket
    from time import sleep
```

```
    print "Preparing iBOB"
    # open the board
    s = Login(host)

    # set the default parameters
    ResetAll(s)
    sleep(1)
    SetLVLs(s,lvl)
    sleep(1)

    return s

def Cleanup(sock):
    ResetAll(sock)
    sock.shutdown(2)

def Capture(bd = ['169.254.128.1'],lvl=
[[100,100,100,100]],captime=10,fname = ''):
    import time
    import os

    print "Starting Capture"

    nb = len(bd)

    # Activate the Boards
    s = []
    for i in range(nb):
        #print bd[i][0]
        s.append(Startup(bd[i],lvl[i][0:4]))
    print s
    # Start UDP
    for i in range(nb):
        StartUDP(s[i])

    # Enable the data output
    for i in range(nb):
        Enable(s[i])
        time.sleep(1)

    # Start the capture
    if fname == '':
        fname = time.strftime("%b%dRun-%H%M%S.pcap",
        time.localtime())
    #print fname
    os.system("sudo tcpdump -Z trj -s 2048 -i eth1 -w " +
    fname + " -C 50 &")
```

```
    # Close the telnet session (to log in during the run)
    for i in range(nb):
        Logout(s[i])

    # Wait
    time.sleep(captime)

    # End the transmission
    print "Cleaning up"
    for i in range(nb):
        s = Login(bd[i])
        Cleanup(s)

    # Stop the Capture
    os.system("sudo killall -2 tcpdump")
    #os.system("sudo killall -2 tcpdump")
    time.sleep(2)

    print "Capture Complete!"

def Snapshot(bd = ["169.254.128.1"]):
    import time
    fname = time.strftime("%b%dSnap-%H%M%S.pcap",
    time.localtime())
    #print bd
    nb = len(bd)
    lvl = []
    for i in range(nb):
        lvl.append([30,30,30,30])
    Capture(bd,lvl,10,fname)
    return fname

def Stats(fname):
    #from pylab import *
    #import numpy

    #print fname

    data = ReadPCAP(fname)

    # sort the data
    ch1a = []
    ch2a = []
    ch3a = []
    ch4a = []
    ch1b = []
    ch2b = []
```

```
ch3b = []
ch4b = []
ch1c = []
ch2c = []
ch3c = []
ch4c = []
ch1d = []
ch2d = []
ch3d = []
ch4d = []

for i in range(len(data[0])):
    if data[1][i] == 1:
        ch1a.append(data[3][i])
        ch2a.append(data[4][i])
        ch3a.append(data[5][i])
        ch4a.append(data[6][i])
    if data[1][i] == 2:
        ch1b.append(data[3][i])
        ch2b.append(data[4][i])
        ch3b.append(data[5][i])
        ch4b.append(data[6][i])
    if data[1][i] == 3:
        ch1c.append(data[3][i])
        ch2c.append(data[4][i])
        ch3c.append(data[5][i])
        ch4c.append(data[6][i])
    if data[1][i] == 4:
        ch1d.append(data[3][i])
        ch2d.append(data[4][i])
        ch3d.append(data[5][i])
        ch4d.append(data[6][i])

print len(ch1a),len(ch1b),len(ch1c),len(ch1d)

# calculate the sigma values
s1a = FindSigma(ch1a)
s2a = FindSigma(ch2a)
s3a = FindSigma(ch3a)
s4a = FindSigma(ch4a)
s1b = FindSigma(ch1b)
s2b = FindSigma(ch2b)
s3b = FindSigma(ch3b)
s4b = FindSigma(ch4b)
s1c = FindSigma(ch1c)
s2c = FindSigma(ch2c)
s3c = FindSigma(ch3c)
s4c = FindSigma(ch4c)
```

```
#s1d = FindSigma(ch1d)
#s2d = FindSigma(ch2d)
#s3d = FindSigma(ch3d)
#s4d = FindSigma(ch4d)

return [[s1a,s2a,s3a,s4a],[s1b,s2b,s3b,s4b],
[s1c,s2c,s3c,s4c]]
```

A.4 Data Tests

Figure A.5 displays a series of RDAQ data plots captured during the first (February 2008) instrument delay tests. In this test, a pulse-modulated monochromatic sine wave (1465 MHz, down-converted by the receiver to 25 MHz) was transmitted from the VLA operation center (cf. Fig. A.6, Bld. 14) toward the array center. The modulation width was set to 100 ns with a repeat rate of 13 μs and the receiver response was recorded with the RESUN data acquisition system. The right panel of Figure A.5 shows a one second RDAQ output data sample from a single antenna located at "DW7" (e), a histogram of the recorded voltage samples (f), a histogram of the measured time between threshold events before the test signal was enabled (g), and a histogram of the time between events after the signal was enabled (h). Corresponding plots to the left (panels a - d) are made using numerical models for the trigger logic and pulse-modulated test signal. The observed RDAQ response is in excellent with the numerical model.

This striated structure observed in figure panels a,e is due to trigger algorithm which is designed to save pulses if any antenna registers a threshold event. A single antenna output data then consists of events which were triggered by that antenna, plus residual data stored when events are observed on other antennas. Panels b,f illustrate two effects. First, the abundance of residual data allows post-facto measurements of the instantaneous threshold level by comparing the digital trigger value ($\pm$ 40 in this case) to the standard deviation of the residual samples. Second, there is a slight asymmetry in the occurrence of threshold events. However,

the slight observed decrease in negative-voltage threshold effect is offset by a slight excess of positive-voltage threshold events, so that a histogram of the signal absolute no longer differs from model. While the asymmetry is not completely understood, the source is suspected to be either a small DC offset in the antenna receiver voltage or a EVLA digitization effect.

Panels d and h illustrate that the test signal characteristics can be reproduced in the output data. Each histogram shows an excess of short duration events up until a cutoff of 100 ns, equaling the pulse modulation width. Subsequent pulses at 13 μs, 26 μs and 39 μs are at harmonics of the pulse repeat rate. A spectrum of delays, rather than two discrete 10 ns and 13 μs signals, are observed because of a phase mismatch between the sine wave period (25 MHz), pulse width, and pulse repeat period 13 μs. The mismatch coupled with noise causes irregularities in each pulse.

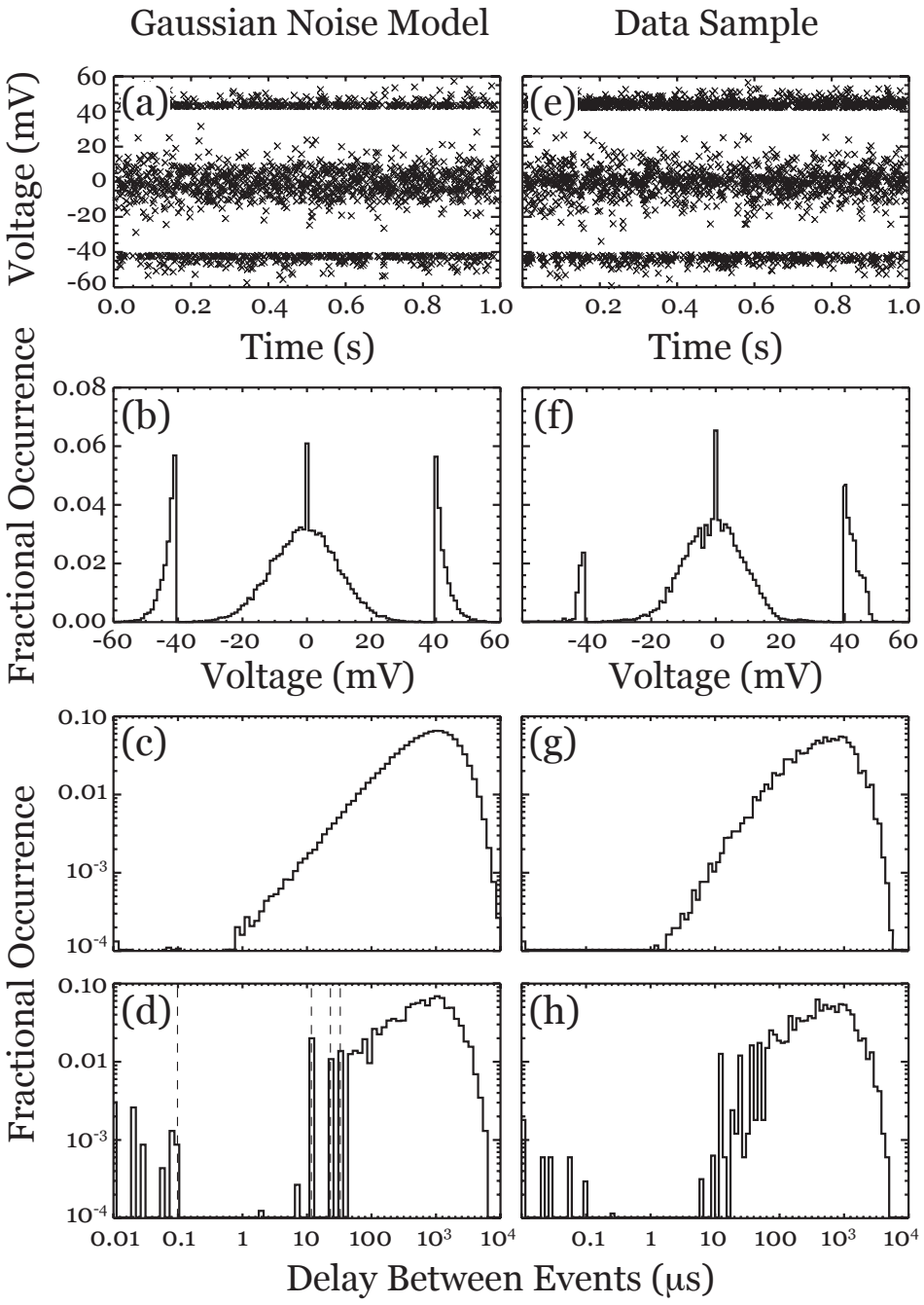

Figure A.5: RESUN data acquisition system recording made during the EVLA receiver pulse width response tests (Sec. 5.1.2.

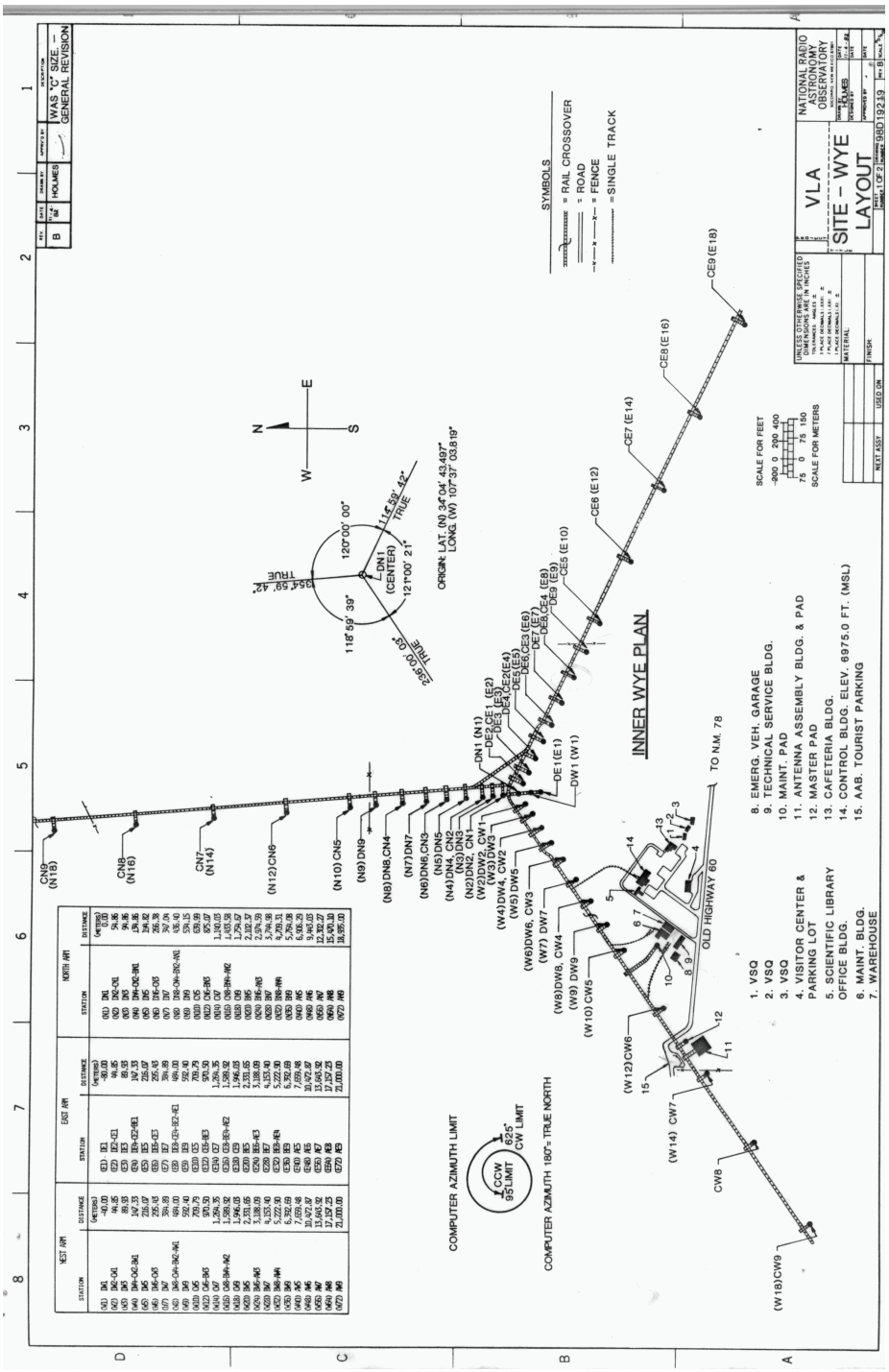

Figure A.6: Illustration of VLA/EVLA antenna locations from the VLA Greenbook (http://www.vla.nrao.edu/astro/guides/greenbook/) showing the array center (position N1) and the EVLA control building (14).

APPENDIX B

AIRBORNE PULSE GENERATOR

The pulse generation circuit and supporting components are less than 1 kg in total weight, making a helium balloon of around 2 meters in diameter an adequate source of lift. Manufactured pulses mimic the anticipated properties of the Ĉerenkov burst emission. Pulses have an adjustable width of approximately 20 ns to 400 ns and a rise/fall response time of < 10 ns, along with an adjustable duty cycle ranging from 1-10 μs. The frequency spectrum of the pulse is generated by an amplified noise source, and is designed to -10 dBm produce RF signals ranging from 500 MHz - 2 GHz. The balloon is a 7-ft diameter polyurethane helium-filled with 4 tether points and a payload of 2.5 kg. The lift capacity and helium retention of the balloon are both sufficient for arial pulse calibration tests.

B.1 Device Components

The following is a list of basic components that comprise the pulse generator circuit (see Fig. B.1. Each item listed is explained further below.

- Battery with remote switch
- Amplified Noise Source
- Adjustable trigger generator and RF switch
- "Fat" dipole antenna

B.1.1 Battery

Components are powered by a Li-Polymer 3300 mAh/18.5V 5 cell battery. The weight of the batter is 0.65 kg and costs $<$ \$200. This battery was purchased from a hobby store, as similar light-weight/high-mAH batteries are used to power remote control cars and planes.

The total current budget for the completed system is $\sim$ 390 mA, with each device contributing

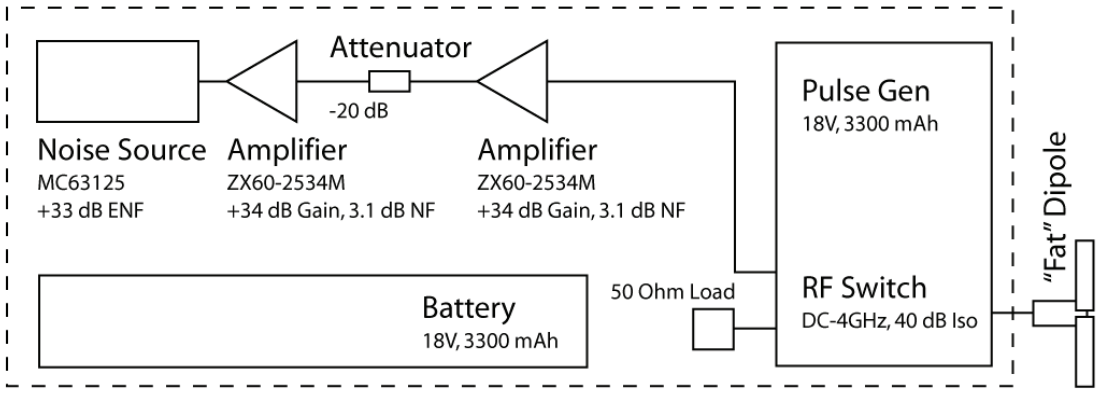

Figure B.1: Block diagram of the RESUN airborne pulse generator.

- 160 mA per 5V amplifier = 320 mA
- 15V Noise Source = 50 mA
- Pulse Generator/RF Switch circuit = 20 mA

For a 50% battery drain (recommended), the resulting signal generation life-span is 4 1/4 hours for an full initial charge. Li-Po batteries require special chargers, which are typically $50-$60 for a 5-cell battery.

B.1.2 Amplified Noise Source

The broadband noise signal is generated by using a 1-2 GHz noise source which is amplified by two low noise amplifiers. The noise source was a model MC63125 source with an excess noise factor (ENF) of +33 dB and required +15 DC. Both amplifiers were Minicircuits model ZX60-2534M amps operating from 500 MHz to 2500 MHz, with +34 dB of gain and a noise figure of 3.1 dB. A -20 dB attenuator was added to provide flexibility in adjusting the output signal strength.

Tests of this amplifier/noise source setup showed a mean RMS Voltage of

77 mV and a mean peak-peak voltage of 754 mV or approximately 10 VRMS. The pulse width for this measurement was 100 ns with a pulse duty cycle of 5 us.

B.1.3 Trigger Generator and RF Switch

The broadband noise generated by the amplified noise source was modulated into pulses by toggling the inputs to a high speed RF switch. The main components of this modulation circuit are listed below and circuit diagrams are given in Figures B.2, and B.3

- 555 timer (LMC555CN - for setting pulse period)
- Monostable Multivibrator with Schmitt-trigger inputs IC chip or "one-shot" (SN74121N - for controlling pulse width).
- High Speed Voltage Comparator (LMV7219 - sharpen the pulse rise/fall times)
- Fast RF Switch (Motorola ADG918BRMZ-ND - modulates the broadband RF noise)

The 555 timer produces a continuously oscillating wave train with a duty cycle that is determined by the values of R3, R4 and C4. Typically, 555 feed-back loops connect the discharge terminal (DIS) directly to the junction of R3 and R4. Instead, this design adds the constant resistor R2 and variable resistor R1 which allows the produced duty cycle to be adjusted without also changing the the output pulse width. For the implementation listed (R1 = 50k Var, R2 = 25k, R3 = 150k, R4 = 100k, C4 = 3pF), the resulting wave train consists of 1 us wide pulses with a variable duty cycle of 1-10 us. Longer duty cycles can be obtained by increasing C4 with respect to the values of R3 and R4. For example, increasing C4 by a factor of 10 (to 30 pF) while leaving R1-R4 fixed increases the variable pulse period to 10-35 us.

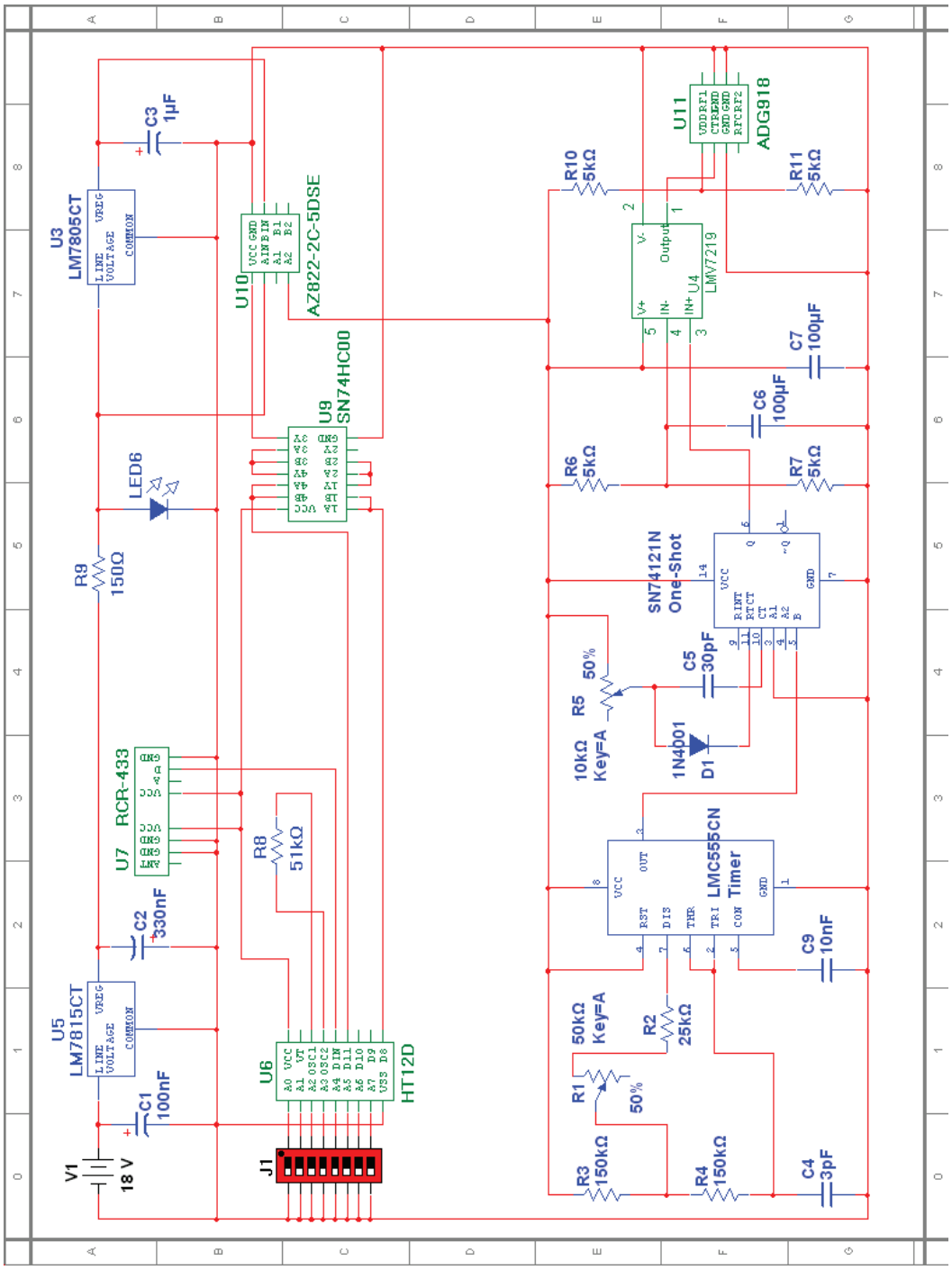

Figure B.2: Circuit diagram of the RESUN airborne pulse generator with remote control power switch.

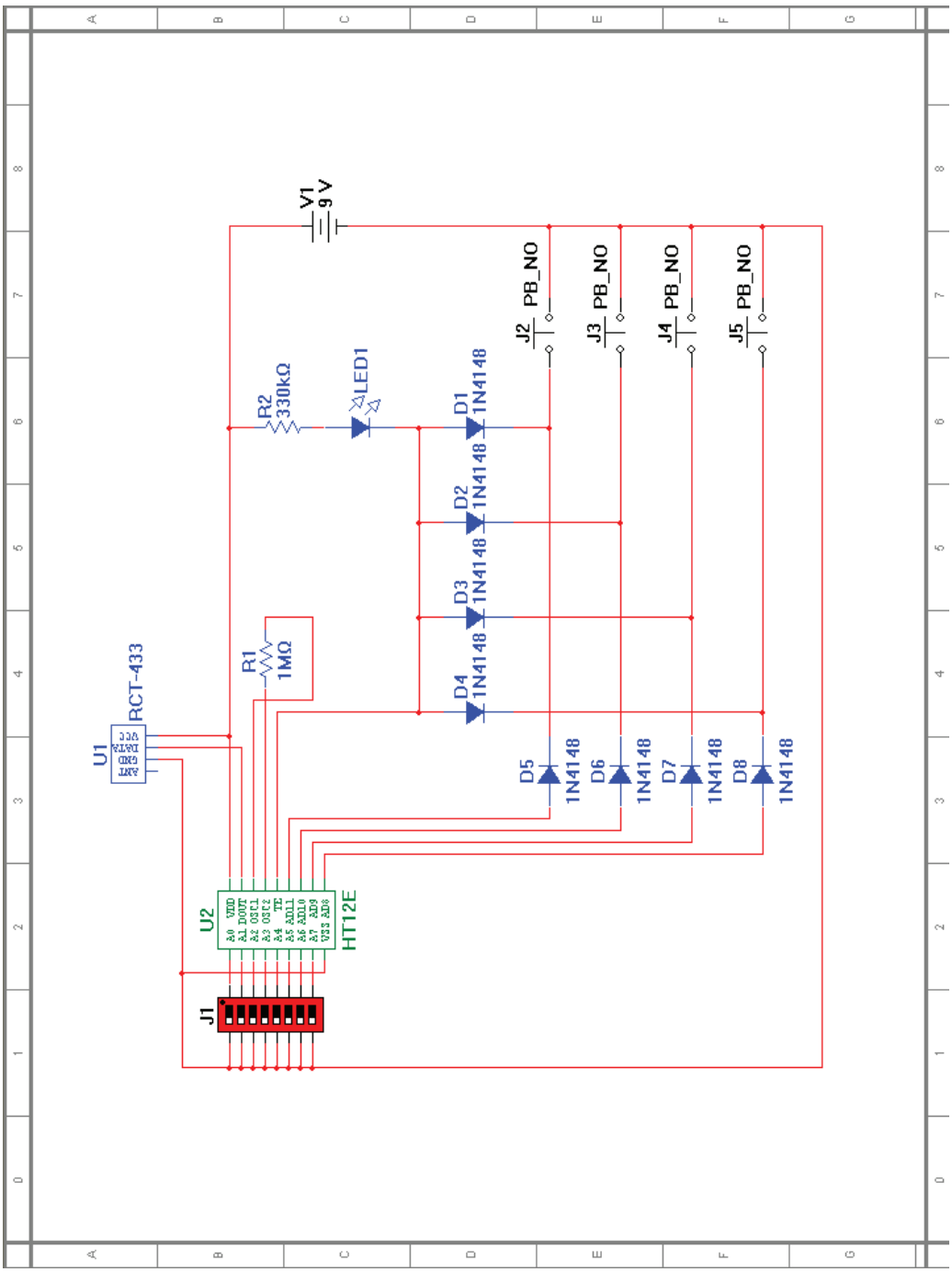

Figure B.3: Circuit diagram of the remote control transmitter.

The wave train from the 555 is fed into a monostable multivibrator ("one-shot") to control the individual pulse width without changing the pulse period.

This is done by setting (or changing) the RC time constant defined by R5 and C5. A diode (D1) is inserted to avoid feedback. The SN74121N TTL output sharpens the pulses from the 555, resulting in a typical rise/fall time < 10 ns. This was sufficient for the RESUN calibration, however the design further employed a high-speed voltage comparator (LMV7219) to obtain < 2 ns pulse rise/fall times. The resulting signal was used to control the RF switch.

The Motorola ADG918BRMZ-ND is a 2-channel, DC-4 GHz RF switch with 40 dB channel isolation and < 10 ns switching time. RF1 is attached to the constant, broadband RF noise source, while RF2 is terminated with a 50 ohm load. In this configuration, the input pulse train acts as a signal modulator, effectively generating broadband noise packets with width and period defined by the trigger source.

B.1.4 Dipole Antenna

A "Fat" 1/4 wavelength dipole antenna was constructed out of copper tubing is used as the element. The antenna has a peak return loss of 15 dB at 1500 MHz and is better that 10 dB from 1350 MHz to 1650 MHz.

B.1.5 Remote Transmitter and Receiver

The addition of a RF Transmitter/Receiver allowed remote access to the device from a range as distant as 150 meters. The remote contains a (RCT-433) 433 MHz, 0 dBm transmitter which sends a 4-bit encoded signal created by a common HT-12E encoder (see Fig. B.3). The receiver (RCR-433) decoded the transmitted signal via a HT-12D decoder and operated a solid-state 5V relay. The relay was then used to enable/disable power to the RF switch and corresponding amplifiers.

B.1.6 Balloon

The flight balloon was a 7-foot diameter polyurethane plastic balloon. Early tests were done with chloroprene weather balloons which are cheaper and provide similar lift, but have a few disadvantages when compared to the polyurethane models. Weather balloons are thin and porous with high helium loss rates, making each balloon essentially single use. Weather balloons are also void of tether points, making the task of controlling the balloon position more difficult.

APPENDIX C

CANDIDATE POST-PROCESSING CODE

Post processing of candidate events was done through a series of IDL scripts. The primary procedures are listed below. Secondary procedures are available upon request.

C.1 Analysis Code

C.1.1 Script: readpcap.pro

The IDL function READPCAP was used to unpack events from the binary packets transmitted and stored by the RDAQ.

```
;-------------------------------------------------------------
; READPCAP
; IDL Function to unpack iBOB PCAP packets
;
; Created: 01/18/08
; Revision 1: Name shortend 02/04/08
; Revision 2: Renamed and edited 09/24/08
; Revision 3: Renamed (from ibob_parse_udp), added
; Phase-B data support
;
; Data files have a series of three parts
; 1. PCAP header (24 bytes, only one per file)
; 2. PPC header (16 bytes, includes arrival timestamp
; and packet size)
; 3. UDP header (42 bytes, includes board info and data
; payload)
;
; INPUTS:
; infile (prompt if not supplied)
; imin (optional, first UDP packet to be read)
; imax (optional, last UDP packet to read)
; phasea (flag to read older Phase-A data)
;
; OUTPUTS:
; data structure containing the 4 board data
;
;-------------------------------------------------------------
function readpcap, infile, imin=imin, imax=imax, $
                   phasea = phasea, verbose=verbose

;keyword setup
if n_params() eq 0 then infile = dialog_pickfile()
if not keyword_set(imin) then imin=0LL
if not keyword_set(imax) then imax=200000LL
```

```
;force imin, imax to be double long
imin=1LL*long(imin)
imax=1LL*long(imax)
if imin ge imax then begin
   print, "Invalid Request.  Please check the values
   of imin, imax."
   return, 0
endif
if keyword_set(phasea) then begin
  DATAORDER = [0,1]
  NSAMPLES = 20LL
  HEADERBYTES = 7
endif else begin
  DATAORDER = [1,0]
  NSAMPLES = 128LL
  HEADERBYTES = 21
endelse

;Global variables
JD1970 = 2440587.5D0
MAXELEMENTS = NSAMPLES*(imax-imin)

;Arrays
pcap_header=bytarr(24)
packet_header=bytarr(16)
udp_header=bytarr(42)
data_header=bytarr(HEADERBYTES)
data=bytarr(8*NSAMPLES)
pkarv_jd=dblarr(MAXELEMENTS)
;ppc_count=ulonarr(MAXELEMENTS)
;reg_full=bytarr(MAXELEMENTS)
;reg_lvl1=bytarr(MAXELEMENTS)
;reg_lvl2=bytarr(MAXELEMENTS)
adc_0i=intarr(MAXELEMENTS)
adc_0q=intarr(MAXELEMENTS)
adc_1i=intarr(MAXELEMENTS)
adc_1q=intarr(MAXELEMENTS)
bin=ulon64arr(MAXELEMENTS)
src=strarr(MAXELEMENTS)
;des=strarr(MAXELEMENTS)

;grab the data file
if keyword_set(verbose) then begin
   print,"Extracting Data from File: "
   print,infile
endif

;open the file as a binary table
```

```
openr,lun,infile,/get_lun

;read the pcap header (24 bytes, only one per gulp file)
readu,lun,pcap_header

;Parse the pcap_header (TODO)
; The file header consists of, in order:
; a 32-bit "magic number";
; a 16-bit major version number;
; a 16-bit minor version number;
; a 32-bit "time zone offset" field that's actually
; not used
; a 32-bit "time stamp accuracy" field that's not
; actually used
; a 32-bit "snapshot length" field;
; a 32-bit "link layer type" field.

;Now read the data
record_count=0LL
udp_count=0LL
while not eof(lun) do begin
   ;read the packet header (16 bytes each)
   readu,lun,packet_header

   ;Parse the packet header
   ;int32 ts_sec   - timestamp seconds
   ;int32 ts_usec  - timestamp microseconds
   ;int32 incl_len - number of octets of packet saved
   ; in file
   ;int32 orig_len - actual length of packet

   ts_sec=ulong(0)
   ts_usec=ulong(0)
   pk_len=ulong(0)
   for i=0,3 do begin
      ts_sec=ts_sec+$
             ishft(ulong(packet_header(0+i)),8*i)
      ts_usec=ts_usec+$
              ishft(ulong(packet_header(4+i)),8*i)
      pk_len=pk_len+$
             ishft(ulong(packet_header(12+i)),8*i)
   endfor
   t_sec=double(ts_sec)+double(ts_usec)/1D6
   ;stop

   ;Check the length to determine if the packet is UDP,
   ;else skip
   if pk_len eq (42 + HEADERBYTES + 8*NSAMPLES) $
```

```
then begin
   ;Valid UDP Packet
   ;stop

   ;Read in the packet info
   readu,lun,udp_header
   readu,lun,data_header
   readu,lun,data

   ;only process the UDP packets between imin and
   ;imax
   if udp_count ge imin and udp_count lt imax $
   then begin
      ;Set the index
      isub=udp_count-imin
      ;data is in bunches of NSAMPLES, so define
      ;the start/stop points
      u=NSAMPLES*isub
      v=NSAMPLES*(isub+1LL)-1LL

      ;Print info if requested
      ;if (udp_count mod long((imax-imin)/10.0))
      ;eq 0 then $
      ; if keyword_set(verbose) then print,
      ;'Reading UDP Packet ',udp_count

      ;parse the UDP header (partial)
      ;1. Ethernet info (14 bytes)
      ;2. IP junk (12 bytes)
      ;3. Source and Destination IP addresses
      src_ip=strtrim(fix(udp_header(26)),2)+"."+$
             strtrim(fix(udp_header(27)),2)+"."+$
             strtrim(fix(udp_header(28)),2)+"."+$
             strtrim(fix(udp_header(29)),2)
      des_ip=strtrim(fix(udp_header(30)),2)+"."+$
             strtrim(fix(udp_header(31)),2)+"."+$
             strtrim(fix(udp_header(32)),2)+"."+$
             strtrim(fix(udp_header(33)),2)
      ;4. Source and Destination ports (2 bytes each)
      ;5. length (8*NSAMPLES + 8)
      ;6. checksum (2 bytes)

      ;parse the data header
      ;1. PPC count (unused in Phase-B)
      ppcc=data_header(3)+$
           ishft(long(data_header(2)),8)+$
           ishft(long(data_header(1)),16)+$
           ishft(long(data_header(0)),24)
```

```
      ;2. FIFO levels (unused in Phase-B)
      reg0=data_header(4)
      reg1=data_header(5)
      reg2=data_header(6)
      ;print,ppcc,reg0,reg1,reg2

      ;parse the data
      data=reform(data,4,2,NSAMPLES)
      ;1. DATA FIFO
      data_fifo=reform(data(*,DATAORDER(0),*))
      ;convert the two's complement data values to
      ;signed int
      data_fifo=(2^8-1)*(data_fifo ge 2^7)-data_fifo
      ;2. INFO/BIN FIFO
      bin_fifo=reform(data(*,DATAORDER(1),*))
      bc0=ishft(reform(long(bin_fifo(0,*))),24)
      bc1=ishft(reform(long(bin_fifo(1,*))),16)
      bc2=ishft(reform(long(bin_fifo(2,*))),8)
      bc3=reform(long(bin_fifo(3,*)))
      bincount=bc0+bc1+bc2+bc3

      ;assign the values to the arrays
      pkarv_jd(u:v)=make_array(NSAMPLES,$
                   value=JD1970+t_sec/86400D0)
      ;ppc_count(u:v)=make_array(NSAMPLES,value=ppcc)
      ;reg_full(u:v)=make_array(NSAMPLES,value=reg0)
      ;reg_lvl1(u:v)=make_array(NSAMPLES,value=reg1)
      ;reg_lvl2(u:v)=make_array(NSAMPLES,value=reg2)
      adc_0i(u:v)=data_fifo(0,*)
      adc_0q(u:v)=data_fifo(1,*)
      adc_1i(u:v)=data_fifo(2,*)
      adc_1q(u:v)=data_fifo(3,*)
      bin(u:v)=bincount
      src(u:v)=make_array(NSAMPLES,value=src_ip)
      ;des(u:v)=make_array(NSAMPLES,value=des_ip)
      ;print,adc0_full,adc0_lvl,adc1_lvl
      ;stop
   endif

;increment the udp count
udp_count=udp_count+1

endif else begin
    ;read the packet and toss
    buf=bytarr(pk_len)
    readu,lun,buf
endelse
```

```
;increment the record count
record_count=record_count+1

endwhile

;free the file
free_lun,lun
;stop

;count the number of UDP packets returned
udp_ret=isub

if udp_ret eq 0 then begin
   print, 'No UDP packets returned.'
   return, 0
endif

if keyword_set(verbose) then begin
   print, 'Processed UDP packets '+strtrim(imin,2)+$
          ' through '+ $
          strtrim(imin+isub,2)
   print, 'Total UDP packets in file = '+$
          strtrim(udp_count,2)
   print, 'Total Records, UDP or otherwise = '+$
          strtrim(record_count,2)
endif

;sort
if keyword_set(verbose) then print, 'Sorting Data'
ib1=where(src eq '169.254.128.1')
ib2=where(src eq '169.254.128.2')
ib3=where(src eq '169.254.128.3')
ib4=where(src eq '169.254.128.4')
;stop

if ib1(0) ne -1 then $
    b1={board:1, fname:infile, adc_0i:adc_0i(ib1), $
    adc_0q:adc_0q(ib1), adc_1i:adc_1i(ib1), $
        adc_1q:adc_1q(ib1), bin:bin(ib1), $
    pkarv_jd:pkarv_jd(ib1), valid:1} else b1={valid:0}

if ib2(0) ne -1 then $
    b2={board:2, fname:infile, adc_0i:adc_0i(ib2), $
    adc_0q:adc_0q(ib2), adc_1i:adc_1i(ib2), $
        adc_1q:adc_1q(ib2), bin:bin(ib2), $
    pkarv_jd:pkarv_jd(ib2), valid:1} else b2={valid:0}

if ib3(0) ne -1 then $
```

```
    b3={board:3, fname:infile, adc_0i:adc_0i(ib3), $
    adc_0q:adc_0q(ib3), adc_1i:adc_1i(ib3), $
        adc_1q:adc_1q(ib3), bin:bin(ib3), $
    pkarv_jd:pkarv_jd(ib3), valid:1} else b3={valid:0}

if ib4(0) ne -1 then $
    b4={board:4, fname:infile, adc_0i:adc_0i(ib4), $
    adc_0q:adc_0q(ib4), adc_1i:adc_1i(ib4), $
        adc_1q:adc_1q(ib4), bin:bin(ib4), $
    pkarv_jd:pkarv_jd(ib4), valid:1} else b4={valid:0}

if keyword_set(verbose) then print, 'Returning Samples'
return, {b1:b1, b2:b2, b3:b3, b4:b4, $
  boards:[b1.valid,b2.valid,b3.valid,b4.valid]}

end
```

C.1.2 Script: get_lunar_pos.pro

This function calculated the GEO coordinate for a position on the moon. Note this function requires the MOONPOS function provided by the NASA astronomical library.

```
;-------------------------------------------------------
;Returns the [x,y,z] coordinates in GEO coordinates
;
;x-axis = in the equitorial plane, fixed with rotation
;and passes
;through the Greenwich meridian (0d Lon)
;z-axis = parallel to rotation axis of earth
;y-axis = z-axis x x-axis
;
;Calls the NASA IDL Astrolib
;
;EDIT 10/26/08 - Changed function to accept vectors of
;jd values
;EDIT 01/22/09 - Added RASHIFT and DECSHIFT commands
;for calculating
;xyz of lunar edge
;-------------------------------------------------------

function get_lunar_pos,jd,rashift=rashift,$
decshift=decshift,verbose=verbose

;Get the ra, dec and dis (NASA IDL AstroLib)
;Ra  - Apparent right ascension of the moon in DEGREES,
```

```
;referred to the
;      true equator of the specified date(s)
;Dec - The declination of the moon in DEGREES
;Dis - The Earth-moon distance in kilometers (between
;the center of the
;      Earth and the center of the Moon).
;MOONPOS, jd, ra, dec, dis, lon, lat
MOONPOS, jd, ra, dec, dis

if keyword_set(rashift) then ra=ra+rashift*$
cos(dec/!radeg)
if keyword_set(decshift) then dec=dec+decshift


;Calculate the XYZ GEI coordinates using ra, dec and dis
zGEI = dis*sin(1D0*dec/!radeg)
yGEI = dis*cos(1D0*dec/!radeg)*sin(1D0*ra/!radeg)
xGEI = dis*cos(1D0*dec/!radeg)*cos(1D0*ra/!radeg)
GEI = reform([xGEI,yGEI,zGEI],n_elements(jd),3)
;stop

;Convert GEI to GEO
;First find the Mean Sidereal Time at Greenwich in deg
;Then, use the GST angle to apply the x-y plane rotation

;eqn 12.1 in "Astronomical Algorithms"
t = (jd-2451545.0D0)/36525D0
GST_mean = (280.46061837D0 + 360.98564736629D0*$
(jd-2451545.0D0) + $
            0.000387933D0*t^2D0 - t^3D0/38710000D0) $
mod 360D0
neg=where(gst_mean lt 0)
if neg(0) ne -1 then gst_mean(neg)=gst_mean(neg)*360D0
;calculate the euation of the equinoxes to convert the
;mean GST to the
;true GST (from AA, chap. 22, chap. 12
;deg
omega=(125.04452D0-1934.136261D0*t) mod 360D0
lsun=(280.4665D0+36000.7698D0*t) mod 360D0
lmoon=(218.3165D0+481267.8813D0*t) mod 360D0
;arcsec
dphi=-17.20D0*sin(omega/!radeg)-1.32D0*$
sin(2*lsun/!radeg)-$
     0.23D0*sin(2*lmoon/!radeg)+0.21D0*$
sin(2*omega/!radeg)
deps=9.20D0*cos(omega/!radeg)+0.57D0*$
cos(2*lsun/!radeg)+$
     0.10D0*cos(2*lmoon/!radeg)-0.09D0*$
```

```
cos(2*omega/!radeg)
eps_zero=84381.44760D0-46.8150D0*t-0.00059D0*t^2+$
0.001813*t^3
;deg
eps=(eps_zero+deps)/3600D0
;correction
dGST=dphi*cos(eps/!radeg)
GST_apparent=(GST_mean+dGST/3600D0) mod 360D0
;stop

GST=GST_apparent
;apply the rotation
;zGEO = total(GEI*[0,0,1],/DOUBLE)
;yGEO = total(GEI*[-sin(1D0*GST/!radeg),
;cos(1D0*GST/!radeg),0],/DOUBLE)
;xGEO = total(GEI*[cos(1D0*GST/!radeg),
;sin(1D0*GST/!radeg),0],/DOUBLE)
;GEO = [xGEO, yGEO, zGEO]
zGEO = zGEI
yGEO = xGEI*(-sin(1D0*GST/!radeg))+yGEI*$
cos(1D0*GST/!radeg)
xGEO = xGEI*cos(1D0*GST/!radeg)+yGEI*sin(1D0*GST/!radeg)
GEO = reform([xGEO,yGEO,zGEO],n_elements(jd),3)
;stop

;PRINT
;print Verbose statements
if keyword_set(verbose) then begin
  print,make_array(80,value='-'),format='(80A)'
  for i=0,n_elements(jd)-1 do begin
    print, jd(i),date_conv(jd(i),'s'), $
format='("JD = ",F17.8," ",A)'
    ra_str=adstring(ra(i)/15.0)
    dec_str=adstring(dec(i))
    print, ra(i), ra_str, dec(i), dec_str, dis(i), $
      format='("RA = ",F7.3, " [",A,"] ", " $
Dec = ",F7.3, " [",A,"] ", " D (km) = ",F10.3)'
    print, "The (app) GEI [x,y,z] coordinates (km) $
are : ["+$
      strtrim(GEI(i,0),2)+","+strtrim(GEI(i,1),2)+","+$
strtrim(GEI(i,2),2)+"]"
    print, "GST (mean) = " + strtrim(GST_mean(i),2)+$
" deg ["+$
      adstring(gst_mean(i)/15)+"]"
    print, "GST (app) = "+strtrim(GST_apparent(i),2)+$
" deg ["+$
      adstring(gst_apparent(i)/15)+"]"
    print, "The GEO [x,y,z] coordinates (km) are : ["+$
```

```
      strtrim(GEO(i,0),2)+","+strtrim(GEO(i,1),2)+","+$
strtrim(GEO(i,2),2)+"]"
  endfor
  print,make_array(80,value='-'),format='(80A)'
endif

return, reform(GEO)
end
```

C.1.3 Script: channel_compare.pro

This is the main coincident pulse detection script. Analysis was performed by (1) loading the data using the READPCAP script, (2) computing the data RMS levels, (3) marking the threshold events, (4) calculating the total signal delays for every baseline for each event, (5) checking for coincident event using a series of matrix shifts.

```
;-------------------------------------------------------
; CHANNEL_COMPARE
; IDL Procedure to compare the iBOB channel data
; "the work-horse function"
; USAGE
; 1. Read the data using READPCAP
;    data = READPCAP("infile",/verbose)
; 2. Send single board data to CHANNEL_COMPARE
;    if data.b1.valid eq 1 then channel_compare,data.b1,
;    /verbose
;-------------------------------------------------------
function match_pulse,b,d,t,bin_err,bin_rng
  ;calculate txb (time for each trigger) and
;expand by bin_rng for shift search
  txb=[lon64arr(bin_rng,4), long64(t)*b, $
lon64arr(bin_rng,4)]

  ;shift and search
  n=n_elements(b(*,0))
  match=bytarr(n,4)
  for i=0,2*bin_rng do begin
     match+=abs((b-d)-txb(i:n-1+i,*)) le bin_err
  endfor

  ;ignore multiple matches
  match=match gt 0
  return, match
```

```
end

pro channel_compare,data,fake_delays=fake_delays,$
phasea=phasea,verbose=verbose

;Search Globals
bin_rng = 8LL
min_err = 15LL
max_err = 1000LL
min_sig = 3.5D0
max_sig = 4.75D0

;STEP A - SET SHORT NAMES    ------------------------
n = n_elements(data.bin)
board = data.board - 1
ch1 = data.adc_0i
ch2 = data.adc_0q
ch3 = data.adc_1i
ch4 = data.adc_1q
bin = data.bin
jd = data.pkarv_jd
;stop

;STEP B - REMOVE PPS RESETS    ----------------------
flip = where((1D0*bin(1:n-1)-1D0*bin(0:n-2)) lt 0)
if flip(0) ne -1 then for i=0,n_elements(flip)-1 do $
   bin(flip(i)+1:n-1) = bin(flip(i)+1:n-1)+10LL^8
dt = (max(bin)-min(bin))*10D-9
if keyword_set(verbose) then print,dt,$
format='("Data Length = ",F6.2," sec")'
;stop

;STEP C - COMPUTE STATS    -------------------------
s = datastats(data)
;s = datastats(data,/mkplot)

if keyword_set(verbose) then begin
   print,"Estimate Channel Levels"
   print,"      CHAN        LVL     NTRIG       "+$
   "MEDIAN       SIGMA        NSAMP"
   for i=0,3 do print,i+1,s.datalvl[i],s.ntrig[i],$
                      s.m[i],s.siglvl[i],s.nsamp[i]
endif

;set the min_sigma level for the data
min_sig = max([min_sig,s.datalvl/s.siglvl])
;stop
```

```
;STEP D - BUILD THE TRIGGER MATRIX    --------------
if keyword_set(verbose) then print,$
   "Building Trigger Matrix"

sm = fltarr(n,4)
sm(*,0) = abs(ch1)/s.siglvl[0]
sm(*,1) = abs(ch2)/s.siglvl[1]
sm(*,2) = abs(ch3)/s.siglvl[2]
sm(*,3) = abs(ch4)/s.siglvl[3]

t1 = where(abs(ch1) ge s.datalvl[0])
t2 = where(abs(ch2) ge s.datalvl[1])
t3 = where(abs(ch3) ge s.datalvl[2])
t4 = where(abs(ch4) ge s.datalvl[3])

t = bytarr(n,4)
t(t1,0) = 1
t(t2,1) = 1
t(t3,2) = 1
t(t4,3) = 1
;stop

;STEP E - LOAD ANTENNA VALUES    -------------------
if keyword_set(verbose) then print,$
"Loading Sub-Array Parameters"
a = get_setup(jd(0))
;stop

;select the board
a = reform(a,4,4)
a = reform(a(*,board))

if keyword_set(verbose) then begin
   print,"Selected Antennas :"
   print,"PAD       X(km)           Y(km)           "+$
         "Z(km)           DELAY(ns)"
   for i=0,3 do print,a(i).pad,a(i).r[0],a(i).r[1],$
                      a(i).r[2],a(i).delay
endif
;stop

;STEP F - CALCULATE LUNAR POSITION    --------------
if keyword_set(verbose) then print,$
   "Finding the Lunar Position"

;change for Phase A processing
n_beams = 3
if keyword_set(phasea) then n_beams = 2
```

```
beam_angle = 2D0*!pi*board/n_beams
;lunar center for approx dec
moonpos,jd(n/2),ra,dec
rashift = 0.25d * cos(beam_angle) * cos(dec/!radeg)
decshift = 0.25d * sin(beam_angle)
m = get_lunar_pos(jd(n/2),rashift=rashift,$
                  decshift=decshift,verbose=verbose)
;stop

;STEP G - CALCULATE DELAYS     ---------------------
;if keyword_set(verbose) then print,
;"Calculating the Delays"

d=intarr(n,4)
;d is an array that contains the 4-antenna
;delay set (in samples) for EVERY
;trigger event
d(t1,*)=round(make_array(n_elements(t1),value=0.1d) # $
 [0d,$
  calc_delay(a[0].r,a[1].r,m)-(a[0].delay-a[1].delay),$
  calc_delay(a[0].r,a[2].r,m)-(a[0].delay-a[2].delay),$
  calc_delay(a[0].r,a[3].r,m)-(a[0].delay-a[3].delay)])
d(t2,*)=round(make_array(n_elements(t2),value=0.1d) # $
 [calc_delay(a[1].r,a[0].r,m)-(a[1].delay-a(0).delay),$
  0d,$
  calc_delay(a[1].r,a[2].r,m)-(a[1].delay-a(2).delay),$
  calc_delay(a[1].r,a[3].r,m)-(a[1].delay-a(3).delay)])
d(t3,*)=round(make_array(n_elements(t3),value=0.1d) # $
 [calc_delay(a[2].r,a[0].r,m)-(a[2].delay-a(0).delay),$
  calc_delay(a[2].r,a[1].r,m)-(a[2].delay-a(1).delay),$
  0d,$
  calc_delay(a[2].r,a[3].r,m)-(a[2].delay-a(3).delay)])
d(t4,*)=round(make_array(n_elements(t4),value=0.1d) # $
 [calc_delay(a[3].r,a[0].r,m)-(a[3].delay-a(0).delay),$
  calc_delay(a[3].r,a[1].r,m)-(a[3].delay-a(1).delay),$
  calc_delay(a[3].r,a[2].r,m)-(a[3].delay-a(2).delay),$
  0d])
;stop

;STEP H - FIND THE COINCIDENT PULSES     -----------
if keyword_set(verbose) then begin
   print,"Finding the Coincident Pulses"
   ;print,min_err,format='("Bin Uncertainty = ",I3)'
endif

;create a bin value array
b=long64(bin)#make_array(4,value=1LL)
```

```
;stop

;mark the triggers to search
i_min = where(total(sm ge min_sig, 2) ge 1)
i_max = where(total(sm ge max_sig, 2) ge 1)

;search
m_min = match_pulse(b(i_min,*),d(i_min,*),t(i_min,*),$
min_err,bin_rng)
m_max = match_pulse(b(i_max,*),d(i_max,*),t(i_max,*),$
max_err,bin_rng)
;stop

;STEP I - COUNT THE HITS    ------------------------
cnt_min=total(m_min,2)
cnt_max=total(m_max,2)

h2_min=where(cnt_min eq 2)
h3_min=where(cnt_min eq 3)
h4_min=where(cnt_min eq 4)
;h2_max=where(cnt_max eq 2)
;h3_max=where(cnt_max eq 3)
h4_max=where(cnt_max eq 4)

n1_min = n_elements(cnt_min)
n2_min = n_elements(h2_min)
if h3_min(0) eq -1 then n3_min = 0 else n3_min = $
   n_elements(h3_min)
if h4_min(0) eq -1 then n4_min = 0 else n4_min = $
   n_elements(h4_min)
;n1_max = n_elements(cnt_max)
;n2_max = n_elements(h2_max)
;if h3_max(0) eq -1 then n3_max = 0 else n3_max =
;n_elements(h3_max)
if h4_max(0) eq -1 then n4_max = 0 else n4_max = $
   n_elements(h4_max)
;stop

;STEP J - PRINT    --------------------------------
;daycnv,jd(0),yr,mn,day,hr
fname = strsplit(data.fname,'/',/extract)
fname = fname(n_elements(fname)-1)

;openw,lun,'results.txt',/get_lun,/append
;printf,lun,fname, board+1,dt, s.datalvl/s.siglvl,
;n1_min, n2_min, n3_min, n4_min, n4_max, $
;       format = '(A,2X,I1,2X,F5.2,2X,4(F4.2,2X),
;5(I0,2X))'
```

```
;free_lun,lun
stop

;if keyword_set(verbose) then begin

;3-station hits
;if h3(0) ne -1 then begin
;   imax=min([10,n_elements(h3)])
;   print,n_elements(h3),format='(I-6,
;   " 3 station coincidences found.")'
;   print,"First " + strtrim(imax,2) + " of "+
;   strtrim(n_elements(h3),2) + $
;      " hits displayed."
;   for i=0,imax-1 do begin
;      j=h3(i)
;      k=[j,jd(j),reform(match(j,*)),reform(d(j,*))]
;      print,k,format='(I10,5x,F14.6,5x,2("(",3(I0,","),I0,")",5x))'
;   endfor
;endif

;endif

;if h4(0) ne -1 then begin
 ;;  imax=n_elements(h4)
 ;  print,n_elements(h4),format='(I-6," 4 station coincidences
 ;  found!")'
;   print,"Displaying " + strtrim(n_elements(h4),2) + " hit(s)."
;   for i=0,imax-1 do begin
;      j=h4(i)
;      k=[j,jd(j),reform(match(j,*)),reform(d(j,*))]
;      print,k,format='(I10,5x,F14.6,5x,2("(",3(I0,","),I0,")",5x))'
;   endfor
;endif
;stop
end
```

BIBLIOGRAPHY

Abbasi, R. U., T. Abu-Zayyad, M. Allen, J. F. Amann, G. Archbold, K. Belov, J. W. Belz, S. Y. B. Zvi, D. R. Bergman, A. Biesiadecka, S. A. Blake, J. H. Boyer, O. A. Brusova, G. W. Burt, C. Cannon, Z. Cao, W. Deng, Y. Fedorova, J. Findlay, C. B. Finley, R. C. Gray, W. F. Hanlon, C. M. Hoffman, M. H. Holzscheiter, G. Hughes, P. Hüntemeyer, D. Ivanov, B. F. Jones, C. C. H. Jui, K. Kim, M. A. Kirn, B. C. Knapp, E. C. Loh, M. M. Maestas, N. Manago, E. J. Mannel, L. J. Marek, K. Martens, J. A. J. Matthews, J. N. Matthews, S. A. Moore, A. O'Neill, C. A. Painter, L. Perera, K. Reil, R. Riehle, M. D. Roberts, D. Rodriguez, M. Sasaki, S. R. Schnetzer, L. M. Scott, M. Seman, G. Sinnis, J. D. Smith, R. Snow, P. Sokolsky, C. Song, R. W. Springer, B. T. Stokes, S. R. Stratton, J. R. Thomas, S. B. Thomas, G. B. Thomson, D. Tupa, L. R. Wiencke, A. Zech, and X. Zhang (2008, September). An Upper Limit on the Electron-Neutrino Flux from the HiRes Detector. *"Astrophysical Journal" 684*, 790–793.

Alvarez-Muñiz, J., E. Marqués, R. A. Vázquez, and E. Zas (2006, July). Coherent radio pulses from showers in different media: A unified parametrization. *Physical Review D 74*(2), 023007–+.

Alvarez-Muniz, J., C. W. James, R. J. Protheroe, and et al. (2008, 0). Cherenkov radio emission from showers in dense media at eev energies. *International Cosmic Ray Conference 5*, 1507–1510.

Alvarez-Muniz, J., R. A. Vazquez, and E. Zas (2000, 1). Characterization of neutrino signals with radiopulses in dense media through the landau-pomeranchuk-migdal effect. *Physical Review D 61*(2), 023001.

Askaryan, G. A. (1962). Excess Negative Charge of the Electron-Photon Shower and Coherent Radiation Originating from It. Radio Recording of Showers under the Ground and on the Moon. *Journal of the Physical Society of Japan Supplement 17*, C257+.

Barwick, S. W. e. a. (2006, May). Constraints on Cosmic Neutrino Fluxes from the Antarctic Impulsive Transient Antenna Experiment. *Physical Review Letters 96*(17), 171101–+.

Beck, R. (2005, August). The Square Kilometer Array (SKA) - Status and prospects. *Astronomische Nachrichten 326*, 608–609.

Beresnyak, A. R., R. D. Dagkesamanskii, I. M. Zheleznykh, A. V. Kovalenko, and V. V. Oreshko (2005, February). Limits on the Flux of Ultrahigh-Energy Neutrinos from Radio Astronomical Observations. *Astronomy Reports 49*, 127–133.

Bhat, N. D. R., S. J. Tingay, and H. S. Knight (2008, April). Bright Giant Pulses from the Crab Nebula Pulsar: Statistical Properties, Pulse Broadening, and Scattering Due to the Nebula. *"Astrophysical Journal" 676*, 1200–1209.

Butler, B. J., M. M. McKinnon, R. A. Perley, and P. E. Dewdney (2006, 8). The expanded very large array (evla). In *IAU Special Session*, Volume 1.

Cronin, J. W., T. K. Gaisser, and S. P. Swordy (1997, January). Cosmic rays at the energy frontier. *Scientific American 276*, 32–37.

Crotty, P., J. Lesgourgues, and S. Pastor (2004, June). Current cosmological bounds on neutrino masses and relativistic relics. *"Physical Review D" 69*(12), 123007–+.

Dagkesamanskii, R. D. and I. M. Zheleznykh (1989, September). A radio astronomy method of detecting neutrinos and other superhigh-energy elementary particles. *Pis ma Zhurnal Eksperimental noi i Teoreticheskoi Fiziki 50*, 233–235.

Engel, R., D. Seckel, and T. Stanev (2001, November). Neutrinos from propagation of ultrahigh energy protons. *"Physical Review D" 64*(9), 093010–+.

Fodor, Z., S. D. Katz, and A. Ringwald (2002, 4). Determination of absolute neutrino masses from bursts of z bosons in cosmic rays. *Physical Review Letters 88*, 171101.

Fogli, G. L., E. Lisi, A. Marrone, A. Melchiorri, A. Palazzo, P. Serra, and J. Silk (2004, December). Observables sensitive to absolute neutrino masses: Constraints and correlations from world neutrino data. *"Physical Review D" 70*(11), 113003–+.

Gayley, K. G., R. L. Mutel, and T. R. Jaeger (2009, December). Analytic Aperture Calculation and Scaling Laws for Radio Detection of Lunar-target Ultrahigh-energy Neutrinos. *"Astrophysical Journal" 706*, 1556–1570.

Gorham, P. W., P. Allison, S. W. Barwick, J. J. Beatty, D. Z. Besson, W. R. Binns, C. Chen, P. Chen, J. M. Clem, A. Connolly, P. F. Dowkontt, M. A. Duvernois, R. C. Field, D. Goldstein, A. Goodhue, C. Hast, C. L. Hebert, S. Hoover, M. H. Israel, J. Kowalski, J. G. Learned, K. M. Liewer, J. T. Link, E. Lusczek, S. Matsuno, B. C. Mercurio, C. Miki, P. Miočinović, J. Nam, C. J. Naudet, J. Ng, R. J. Nichol, K. Palladino, K. Reil, A. Romero-Wolf, M. Rosen, L. Ruckman, D. Saltzberg, D. Seckel, G. S. Varner, D. Walz, Y. Wang, and F. Wu (2009, 7). New limits on the ultrahigh energy cosmic neutrino flux from the anita experiment. *Physical Review Letters 103*, 051103.

Gorham, P. W., S. W. Barwick, and J. J. e. a. Beatty (2007, 10). Observations of the askaryan effect in ice. *Physical Review Letters 99*(17), 171101.

Gorham, P. W., C. L. Hebert, K. M. Liewer, C. J. Naudet, D. Saltzberg, and D. Williams (2004, July). Experimental Limit on the Cosmic Diffuse Ultrahigh Energy Neutrino Flux. *Physical Review Letters 93*(4), 041101–+.

Gorham, P. W., D. P. Saltzberg, P. Schoessow, W. Gai, J. G. Power, R. Konecny, and M. E. Conde (2000, December). Radio-frequency measurements of coherent transition and Cherenkov radiation: Implications for high-energy neutrino detection. *Physical Review E 62*, 8590–8605.

Greisen, K. (1966, April). End to the Cosmic-Ray Spectrum? *Physical Review Letters 16*, 748–750.

Gusev, G. A., B. N. Lomonosov, K. M. Pichkhadze, N. G. Polukhina, V. A. Ryabov, T. Saito, V. K. Sysoev, E. L. Feinberg, V. A. Tsarev, and V. A. Chechin (2006, 1). Detection of ultrahigh-energy cosmic rays and neutrinos by radio method using artificial lunar satellites. *Cosmic Research 44*, 19–38.

Hankins, T. H., R. D. Ekers, and J. D. O'Sullivan (1996, December). A search for lunar radio Ĉerenkov emission from high-energy neutrinos. *Monthly Notices of the Royal Astronomical Society 283*, 1027–1030.

Hine, B. P. (2009, November). Lunar atmosphere and dust environment explorer (ladee).

James, C. W., R. M. Crocker, R. D. Ekers, T. H. Hankins, J. D. O'Sullivan, and R. J. Protheroe (2007, August). Limit on ultrahigh energy neutrino flux from the Parkes Lunar Radio Cherenkov experiment. *Monthly Notices of the Royal Astronomical Society 379*, 1037–1041.

James, C. W., R. D. Ekers, J. Alvarez-Muiz, R. J. Protheroe, R. A. McFadden, C. J. Phillips, and P. Roberts (2009, 6). Status report and future prospects on lunaska lunar observations with atca. *Nuclear Instruments and Methods in Physics Research A 604*, S112–S115.

James, C. W. and R. J. Protheroe (2009, 6). The directional dependence of apertures, limits and sensitivity of the lunar cherenkov technique to a uhe neutrino flux. *Astroparticle Physics 31*, 392–398.

James, C. W. and R. J. Protheroe (2009, January). The sensitivity of the next generation of lunar Cherenkov observations to UHE neutrinos and cosmic rays. *Astroparticle Physics 30*, 318–332.

Kalashev, O. E., V. A. Kuzmin, D. V. Semikoz, and G. Sigl (2002, September). Ultrahigh-energy neutrino fluxes and their constraints. *"Physical Review D" 66*(6), 063004–+.

Kravchenko, I. e. a. (2006, April). RICE limits on the diffuse ultrahigh energy neutrino flux. *Physical Review D 73*(8), 082002–+.

Lawson, K. D., C. J. Mayer, J. L. Osborne, and M. L. Parkinson (1987, March). Variations in the Spectral Index of the Galactic Radio Continuum Emission in the Northern Hemisphere. *Monthly Notices of the Royal Astronomical Society 225*, 307.

Lehtinen, N. G., P. W. Gorham, A. R. Jacobson, and R. A. Roussel-Dupré (2004, January). FORTE satellite constraints on ultrahigh energy cosmic particle fluxes. *Physical Review D 69*(1), 013008–+.

Meeus, J. (1998). *Astronomical algorithms*. Richmond, VA: Willmann-Bell.

Miocinovic, P., R. C. Field, P. W. Gorham, E. Guillian, R. Milincic, D. Saltzberg, D. Walz, and D. Williams (2006, 8). Time-domain measurement of broadband coherent cherenkov radiation. *Physical Review D 74*(4), 043002.

Olhoeft, G. R. and D. W. Strangway (1975, January). Dielectric properties of the first 100 meters of the moon. *Earth and Planetary Science Letters 24*, 394–404.

Ott, J., e. a. (2010, May). Pushing the limits of the evla: An enhancement program for the next decade.

Panda, S., S. Mohanty, J. Padmanabhan, and O. Stål (2007, November). Prospects for the Giant Metrewave Radio Telescope to observe radio waves from ultra high energy particles interacting with the Moon. *Journal of Cosmology and Astro-Particle Physics 11*, 22–+.

Parsons, A., D. Backer, A. Siemion, H. Chen, D. Werthimer, P. Droz, T. Filiba, J. Manley, P. McMahon, A. Parsa, D. MacMahon, and M. Wright (2008, 11). A scalable correlator architecture based on modular fpga hardware, reuseable gateware, and data packetization. *Publications of the Astronomical Society of the Pacific 120*, 1207–1221.

Reno, M. H. (2005, June). High Energy Neutrino Cross Sections. *Nuclear Physics B Proceedings Supplements 143*, 407–413.

Saltzberg, D., P. Gorham, D. Walz, C. Field, R. Iverson, A. Odian, G. Resch, P. Schoessow, and D. Williams (2001, March). Observation of the Askaryan Effect: Coherent Microwave Cherenkov Emission from Charge Asymmetry in High-Energy Particle Cascades. *Physical Review Letters 86*, 2802–2805.

Scholten, O., J. Bacelar, R. Braun, A. G. de Bruyn, H. Falcke, B. Stappers, and R. G. Strom (2006, October). Optimal radio window for the detection of Ultra-High Energy cosmic rays and neutrinos off the moon. *Astroparticle Physics 26*, 219–229.

Scholten, O., S. Buitink, J. Bacelar, R. Braun, A. G. de Bruyn, H. Falcke, K. Singh, B. Stappers, R. G. Strom, and R. Al Yahyaoui (2009, June). First results of the NuMoon experiment. *Nuclear Instruments and Methods in Physics Research A 604*, 102–+.

Scholten, O., S. Buitink, J. Bacelar, R. Braun, A. G. de Bruyn, H. Falcke, K. Singh, B. Stappers, R. G. Strom, and R. a. Yahyaoui (2009, 10). Improved flux limits for neutrinos with energies above 10$ˆ{22}$ ev from observations with the westerbork synthesis radio telescope. *ArXiv e-prints 0910.4745S*(19), 191301.

Shepard, M. K., R. A. Brackett, and R. E. Arvidson (1995). Self-affine (fractal) topography: Surface parameterization and radar scattering. *Journal of Geophysical Research 100*, 11709–11718.

Sigl, G., S. Lee, P. Bhattacharjee, and S. Yoshida (1999, February). Probing grand unified theories with cosmic-ray, gamma-ray, and neutrino astrophysics. *"Physical Review D" 59*(4), 043504–+.

Stanev, T. (2004, August). Neutrino production by UHECR proton interactions in the infrared background. *Physics Letters B 595*, 50–54.

Veron-Cetty, M. P. and P. Veron (2006, 8). A catalogue of quasars and active nuclei: 12th edition. *Astronomy and Astrophysics 455*, 773–777.

Waxman, E. (2009, August). The case for high energy neutrino astronomy. *Nuclear Physics A 827*, 15–25.

Waxman, E. and J. Bahcall (1999, 1). High energy neutrinos from astrophysical sources: An upper bound. *Physical Review D 59*, 023002.

Williams, D. R. (2004, December). *The Askar'yan effect and detection of extremely high energy neutrinos in the lunar regolith and salt*. Ph. D. thesis, University of California, Los Angeles.

Wynn-Williams, G. (1992, June). *The Fullness of Space*. Cambridge University Press.

Yamamoto, T. (2008, 0). The uhecr spectrum measured at the pierre auger observatory and its astrophysical implications. *International Cosmic Ray Conference 4*, 335–338.

Yoshida, S., H. Dai, C. C. H. Jui, and P. Sommers (1997, April). Extremely High Energy Neutrinos and Their Detection. *The Astrophysical Journal 479*, 547–+.

Zatsepin, G. T. and V. A. Kuz'min (1966, August). Upper Limit of the Spectrum of Cosmic Rays. *Soviet Journal of Experimental and Theoretical Physics Letters 4*, 78–+.

Zuber, M. T., D. E. Smith, L. Alkalai, D. H. Lehman, M. M. Watkins, and Grail Team (2008, March). Outstanding Questions on the Internal Structure and Thermal Evolution of the Moon and Future Prospects from the GRAIL Mission. In *Lunar and Planetary Institute Science Conference Abstracts*, Volume 39 of *Lunar and Planetary Inst. Technical Report*, pp. 1074–+.